

COMPRESSOR BLADE FLOW CONTROL IN AN AXIAL
COMPRESSOR WITH PLASMA ACTUATORS

By

CRAIG A. WILLIAMSON

Bachelor of Science in Mechanical Engineering
Oklahoma Christian University
Edmond, OK, USA
2000

Submitted to the Faculty of the
Graduate College of
Oklahoma State University
in partial fulfillment of
the requirements for
the Degree of
MASTER OF SCIENCE
December, 2008

COMPRESSOR BLADE FLOW CONTROL IN AN AXIAL
COMPRESSOR WITH PLASMA ACTUATORS

Thesis Approved:

Dr. Jamey Jacob

Thesis Advisor

Dr. Andrew Arena

Dr. Frank Chambers

Dr. A. Gordon Emslie

Dean of the Graduate College

ACKNOWLEDGMENTS

First I must thank my wife Laura for her incredible support and understanding during this busy time in our lives. Her loving nature not only towards me but to our children, Camdyn, Carter and Collin, has allowed me to keep focus on the completion of this thesis. My family continues to be my motivation for self improvement.

I have encountered few individuals in life whom had a good answer for any question that was posed to them. Dr. Jamey Jacob is one of these individuals. He often provided guidance and the road ahead when I had thought I had reached a dead end.

I would also like to thank Dr. Frank Chambers and Dr. Andrew Arena for their guidance as my defense committee members.

I must give special thanks to the United States Air Force for not only funding my books and tuition but for also having the faith in me to be able to complete this degree program in 18 months.

TABLE OF CONTENTS

Chapter	Page
1 INTRODUCTION	1
1.1 Importance of Work	1
1.2 Background	2
1.2.1 Compressor Flow Regime	2
1.2.2 Controlling Compressor Flow	4
1.3 Previous work	8
1.3.1 Compressor Flow Characterization	9
1.3.2 Plasma Actuators as a Flow Control Device	10
1.3.3 Turbomachinery Applications of Plasma Actuators	12
2 EXPERIMENTAL SETUP	15
2.1 OSCAR facility	15
2.2 Measurement Instrumentation	16
2.2.1 Uncertainty of Hotwire Velocity Calculations	18
2.3 Data Retrieval and Signal conditioning	23
2.3.1 Drag Calculation Uncertainty	25
2.4 Plasma actuator	26
2.4.1 Construction	26
2.4.2 Power and Control	26
2.4.3 Calculating Forcing Frequency	27
2.4.4 Application to Compressor Blades	30
2.5 Particle Image Velocimetry Setup	30

2.6	Determining Re and Actuator Placement for Experimentation	33
2.6.1	XFOIL Results	33
3	EXPERIMENTAL RESULTS	37
3.1	Exploratory Results	37
3.1.1	Quiescent Plasma Actuator Characterization	37
3.1.2	Baseline Data	40
3.1.3	Mechanical trip	43
3.1.4	Plasma actuator as a steady trip	44
3.2	Parametric Results	51
3.2.1	Counter and Co-Flow Results for 600 RPM at Various Forcing Frequencies	54
3.2.2	Counter and Co-Flow Results for 350 RPM at Various Forcing Frequencies	81
3.2.3	Comparison Between Reynolds Numbers	109
4	CONCLUSIONS	111
4.0.4	Discussion	111
4.0.5	Future work	112
A	Labview Front Panel and Block Diagram	115
B	Visual Basic Code: Window Averaging Algorithm	118
C	XFOIL Supplementary Data	126
	BIBLIOGRAPHY	136

LIST OF TABLES

Table		Page
2.1	Hotwire calibration sample data	21
2.2	Sources of error for velocity uncertainty calculations	22
2.3	Reduced Forcing Frequencies at Various RPM and Forcing Frequencies	29
2.4	XFOIL Caculations for Delta Star at 350 and 600 RPM	36
3.1	Power usage by plasma actuators using Kapton and Teflon as dielectric	38
3.2	Momentum characterization of various configurations	43

LIST OF FIGURES

Figure	Page
1.1 Typical Jet Engine [1]	4
1.2 Compressor Test Rig [1]	5
1.3 Compressor Map [1]	6
1.4 Flow Separation [2]	7
1.5 Typical Plasma Actuator Construction [3]	8
2.1 Photo of OSCAR facility	16
2.2 Schematic of Compressor rig instrumentation	17
2.3 Schematic of Hotwire Calibration Setup	19
2.4 Hotwire calibration graph and curve fit equation	20
2.5 Uncertainty of Velocity measurements using hotwire	22
2.6 Velocity measurements of the rotor wake at 600RPM	24
2.7 Window averaged velocity measurements of the rotor wake at 600RPM	25
2.8 Photograph of the pulsed power system	28
2.9 Schematic of the pulsed power system	29
2.10 Plasma actuator on a compressor blade: approx. 1/4 chord	30
2.11 Plasma actuator on a compressor blade with visible plasma	31
2.12 Plasma actuator on a compressor blade with visible plasma in low ambient lighting	31
2.13 Schematic of the PIV setup	32
2.14 NACA 65-010 at various angles of attack for 350 RPM case [4]	35
2.15 NACA 65-010 at various angles of attack for 600 RPM case [4]	35

3.1	Voltage and amperage on a plasma actuator with Teflon as dielectric	39
3.2	Voltage and amperage on a plasma actuator with Kapton as dielectric	40
3.3	Quiescent PIV Laser setup	40
3.4	Quiescent PIV mounting orientation	41
3.5	Quiescent Velocity profiles for steady plasma actuation with a Kapton dielectric	41
3.6	Quiescent Velocity profiles for steady plasma actuation with a Teflon dielectric	42
3.7	Quiescent Velocity profiles for pulsed plasma actuation with a Kapton dielectric at $F = 50$ Hz	42
3.8	Quiescent Velocity profiles for pulsed plasma actuation with a Teflon dielectric at $F = 50$ Hz	43
3.9	Velocity measurement at 250 RPM, displaying poor wake structure .	44
3.10	Velocity measurement at 700 RPM, displaying poor wake structure .	45
3.11	Mechanical trip installed at 1/4 chord	46
3.12	Plasma actuator in a counter flow orientation	47
3.13	Plasma actuator in a co-flow orientation	48
3.14	600 RPM steady plasma actuation at 1/4 chord	49
3.15	Wake velocity per blade for the mechanical trip blade, and average blade, and a non-actuated plasma blade at 600RPM	53
3.16	Drag variations at various forcing frequencies for 600 RPM with Plasma at 1/4 Chord	55
3.17	Wake Velocity at 600 RPM, 1/4 chord, Counter Flow Plasma: Off . .	56
3.18	Wake Velocity at 600 RPM, 1/4 chord, Counter Flow Plasma: Steady	59
3.19	Wake Velocity at 600 RPM, 1/4 chord, Counter Flow Plasma: $F = 10$ Hz	60

3.20	Wake Velocity at 600 RPM, 1/4 chord, Counter Flow Plasma: $F = 30$ Hz	61
3.21	Wake Velocity at 600 RPM, 1/4 chord, Counter Flow Plasma: $F = 50$ Hz	62
3.22	Wake Velocity at 600 RPM, 1/4 chord, Co-Flow Plasma: Off	63
3.23	Wake Velocity at 600 RPM, 1/4 chord, Co-Flow Plasma: Steady	64
3.24	Wake Velocity at 600 RPM, 1/4 chord, Co-Flow Plasma: $F = 10$ Hz	65
3.25	Wake Velocity at 600 RPM, 1/4 chord, Co-Flow Plasma: $F = 30$ Hz	66
3.26	Wake Velocity at 600 RPM, 1/4 chord, Co-Flow Plasma: $F = 50$ Hz	67
3.27	Drag variations at various forcing frequencies for 600 RPM with Plasma at leading edge	68
3.28	Wake Velocity at 600 RPM, Leading edge, Counter Flow Plasma: Off	70
3.29	Wake Velocity at 600 RPM, Leading edge, Counter Flow Plasma: Steady	71
3.30	Wake Velocity at 600 RPM, Leading edge, Counter Flow Plasma: $F =$ 10 Hz	72
3.31	Wake Velocity at 600 RPM, Leading edge, Counter Flow Plasma: $F =$ 30 Hz	73
3.32	Wake Velocity at 600 RPM, Leading edge, Counter Flow Plasma: $F =$ 50 Hz	74
3.33	Wake Velocity at 600 RPM, Leading edge, Co-Flow Plasma: Off	76
3.34	Wake Velocity at 600 RPM, Leading edge, Co-Flow Plasma: Steady	77
3.35	Wake Velocity at 600 RPM, Leading edge, Co-Flow Plasma: $F = 10$ Hz	78
3.36	Wake Velocity at 600 RPM, Leading edge, Co-Flow Plasma: $F = 30$ Hz	79
3.37	Wake Velocity at 600 RPM, Leading edge, Co-Flow Plasma: $F = 50$ Hz	80
3.38	Drag variations at various forcing frequencies for 350 RPM with Plasma at 1/4 Chord	82
3.39	Wake Velocity at 350 RPM, 1/4 chord, Counter Flow Plasma: Off	83

3.40	Wake Velocity at 350 RPM, 1/4 chord, Counter Flow Plasma: Steady	84
3.41	Wake Velocity at 350 RPM, 1/4 chord, Counter Flow Plasma: F = 10 Hz	85
3.42	Wake Velocity at 350 RPM, 1/4 chord, Counter Flow Plasma: F = 30 Hz	86
3.43	Wake Velocity at 350 RPM, 1/4 chord, Counter Flow Plasma: F = 50 Hz	87
3.44	Wake Velocity at 350 RPM, 1/4 chord, Co-Flow Plasma: Off	89
3.45	Wake Velocity at 350 RPM, 1/4 chord, Co-Flow Plasma: Steady . . .	90
3.46	Wake Velocity at 350 RPM, 1/4 chord, Co-Flow Plasma: F = 10 Hz .	91
3.47	Wake Velocity at 350 RPM, 1/4 chord, Co-Flow Plasma: F = 30 Hz .	92
3.48	Wake Velocity at 350 RPM, 1/4 chord, Co-Flow Plasma: F = 50 Hz .	93
3.49	Drag variations at various forcing frequencies for 350 RPM with Plasma at leading edge	95
3.50	Wake Velocity at 350 RPM, Leading edge, Counter Flow Plasma: Off	97
3.51	Wake Velocity at 350 RPM, Leading edge, Counter Flow Plasma: Steady	98
3.52	Wake Velocity at 350 RPM, Leading edge, Counter Flow Plasma: F = 10 Hz	99
3.53	Wake Velocity at 350 RPM, Leading edge, Counter Flow Plasma: F = 30 Hz	100
3.54	Wake Velocity at 350 RPM, Leading edge, Counter Flow Plasma: F = 50 Hz	101
3.55	Wake Velocity at 350 RPM, Leading edge, Co-Flow Plasma: Off . . .	104
3.56	Wake Velocity at 350 RPM, Leading edge, Co-Flow Plasma: Steady .	105
3.57	Wake Velocity at 350 RPM, Leading edge, Co-Flow Plasma: F = 10 Hz	106
3.58	Wake Velocity at 350 RPM, Leading edge, Co-Flow Plasma: F = 30 Hz	107
3.59	Wake Velocity at 350 RPM, Leading edge, Co-Flow Plasma: F = 50 Hz	108

3.60	Change in drag on a co-flow actuator at 1/4 chord at various Reynolds numbers	110
3.61	Change in drag for a counter flow actuator at 1/4 chord at various Reynolds numbers	110
A.1	Screen shot of Labview front panel	116
A.2	Screen shot of Labview block diagram	117

CHAPTER 1

INTRODUCTION

Over the years optimization of the gas turbine engine has take many forms. There are typically three major components to a gas turbine engine: the compressor, combustor, and turbine. This present work will focus on the potential for improvements in an axial flow compressor. The primary goal of any air breathing compressor is to increase the pressure of the incoming airflow. This is done most efficiently when the increase in pressure is very high and the amount of input work is very low. The focus of this present work is to improve compressor efficiency by experimentally changing the momentum in the boundary layer of a compressor rotor using plasma actuation.

1.1 Importance of Work

Compressor efficiency has always been a point of interest for turbo-machinery designers. According to Mattingly [1] compressor pressure ratios were on the order of 3:1 to about 5:1 in the 1930's-40's. Nearing the end of the 21st century pressure ratios of 40:1 were being achieved. As compressor efficiency increases the pressure ratio also increases. These improvements in efficiency were largely due to the knowledge field advances of variable compressor geometry, rotating stalls, blade tip clearance effects and three dimensional and unsteady flow phenomena characterization. The improvements in these fields allowed the increase in pressure ratios. Compressor hardware design has nearly reached an efficiency plateau. This plateau ushers in areas of study where small improvements to compressor airflow could provide relatively large improvements to modern day compressor efficiency advancements. As compressor

efficiency increases overall engine efficiency is increased. To large scale operators of turbo-machinery, i.e. the airline industry, even a 0.1% increase in efficiency could correlate to millions of dollars in fuel savings in a one year time frame (based on \$9.5 billion per year fuel cost for United Airlines [5]). Increased compressor efficiency could also lead to lower operating temperatures which could extend the life of costly engine hardware. The ability to prevent a stall condition while operating at the edge of the performance envelope is also of interest for turbo-machinery designers. In high performance fighter aircraft, as well as cargo aircraft, the issue of compressor rotating stall prevention is of utmost importance. For military operations a compressor stall in a single engine aircraft could result in the loss of a weapon system, or even more catastrophic the loss of life. This present work has the potential to increase compressor efficiency and to actively prevent a compressor stall.

1.2 Background

1.2.1 Compressor Flow Regime

The gas turbine engine is designed to convert the energy of the incoming fuel into mechanical power and/or the high speed thrust of a jet. There are three major components to a turbine engine: the compressor, combustor, and turbine [Figure 1.1]. The compressor section of a gas turbine engine adds work to the free stream air which enters. The work, which is provided from the downstream turbine section, compresses the incoming air. This is usually done in multiple stages of rotating blades. Stator vanes are usually situated between the stages of rotating blades to redirect airflow to an optimum angle such that more efficient compression can occur. Blade shape and angle are of critical importance to achieve the desired operating point conditions. Each blade and stator vane is typically modeled after some known airfoil shape over which the flow has already been characterized. The compressed air is then fed into the combustion section where it is diffused and combined with atomized fuel.

The fuel and air mixture is then ignited after which a massive expansion of the gases occur. The expanded gases are then forced from the combustion area into the turbine section of the engine where work is performed on the turbine. This work translates into rotational motion of the turbine which in turn causes the compressor to rotate. The compressor and turbine sections are connected with a rigid shaft. The remainder of the hot gases will then either be used for further work extraction in subsequent stages of turbine or will exit the engine core.

Once a compressor is designed and built they are usually instrumented on a test rig where the pumping characteristics are determined [Figure 1.2]. These pumping characteristics are typically represented by a plot called a compressor map. The compressor stall line, as seen in the compressor map [Figure 1.3] is a major limiting factor in the operating envelope of aircraft turbine engines, and is of major concern for new compressor design. For ideal operation the compressor would operate directly on the stall line. Since steady operation above the stall line is impossible, and entering the region even momentarily is dangerous to the compressor the operating line of the compressor is usually located with a buffer zone between it and the stall line.

Compressors typically stall due to the flow separating from the compressor blades. Flow separation is primarily caused by an adverse pressure gradient. For a profile with a curved surface, such as an airfoil, the streamlines of the flow field converge on the uphill causing an increase in flow velocity and a decrease in pressure. [Figure 1.4] This consequent fall in pressure is termed a favorable pressure gradient. Once the flow reaches the high point the streamlines begin to diverge. This divergence causes a decrease in the flow velocity with a consequent rise in pressure. This pressure rise is termed an adverse pressure gradient. The decelerating stream causes the boundary layer thickness to increase such that the stream just parallel to the boundary surface ceases to flow. The adverse pressure gradient then causes the stream in this confined area to reverse its flow. The point at which the reversed flow meets the forward flow

is termed the separation point. The flow reversal causes the fluid near the surface to advect into the mainstream. It is known that separation will cause a decrease in the lift force, a sharp increase in drag, decreased heat transfer, and pressure pulsations. These are all conditions which should be eliminated during compressor operation. Thus compressor blade airfoil design has largely had a goal of preventing separation from occurring.

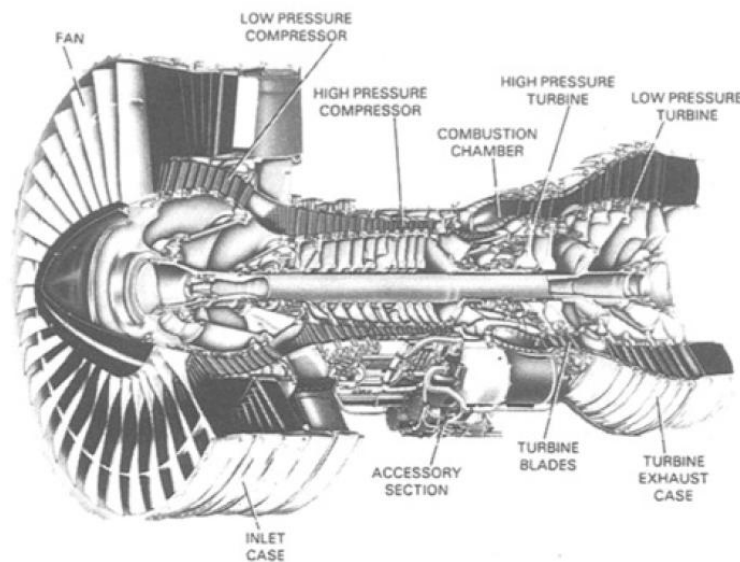


Figure 1.1: Typical Jet Engine [1]

1.2.2 Controlling Compressor Flow

There are multiple ways to control flow conditions over an airfoil. Some of these include turbulators, chevrons, trips, roughness strips, vortex generators, synthetic jets, and plasma actuators. All of these methods change the energy in the boundary layer by adding, removing, or re-characterizing the momentum of the flow. These flow control mechanisms can be further broken down into active, passive or reactive

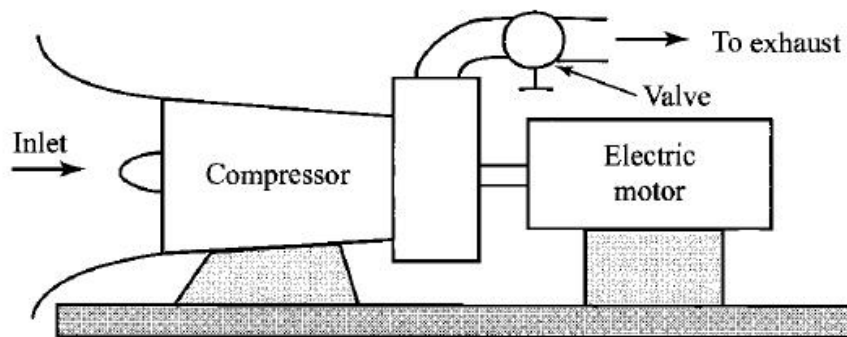


Figure 1.2: Compressor Test Rig [1]

devices. For the purpose of this present work these will be defined as follows. Passive flow control devices are those which are always considered turned-on. An example would be a roughness strip, or a trip in the flow. They are a physical part of the assembly and can be beneficial to the flow control design, while operating in certain flow regimes. An example of an active flow control device would be a synthetic jet, or a plasma actuator. These are devices which can be turned on and off as needed. A reactive flow control device is an active device which is located in a control loop. Typically a reactive flow device will be enabled or disabled when the system meets some predetermined flow condition. These flow conditions are typically determined using a sensing device. Thus when the sensor detects a predetermined condition the

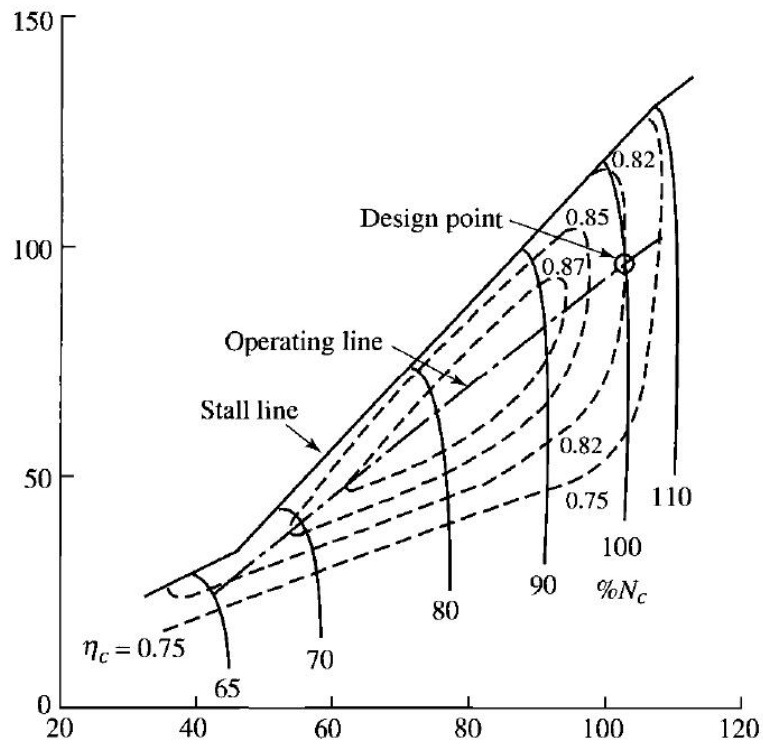


Figure 1.3: Compressor Map [1]

information is used by the system to activate the flow control mechanism.

This present work will focus on plasma actuators, which can be an active or reactive flow control mechanism, with the greatest area of usefulness being as a reactive device. The typical plasma actuator consists of two offset electrodes, one of which is exposed to air while the other is covered by a thin dielectric material.[Figure 1.5] When a high voltage AC signal is applied to the electrodes the air at the edge of the exposed electrode is ionized in the region of the high voltage gradient. The plasma in this area produces a body force on the surrounding air. This body force was characterized by Enloe et al. [6, 7]. In the paper covering plasma morphology, they found that the thrust provided by the actuator is directly proportional to the input power, which is proportional to $V^{7/2}$. They also clearly determined that the aerodynamic plasma actuator produces a dielectric barrier discharge, and discounted bulk heating as a mechanism for affecting the flow. Their final conclusion in the paper over plasma

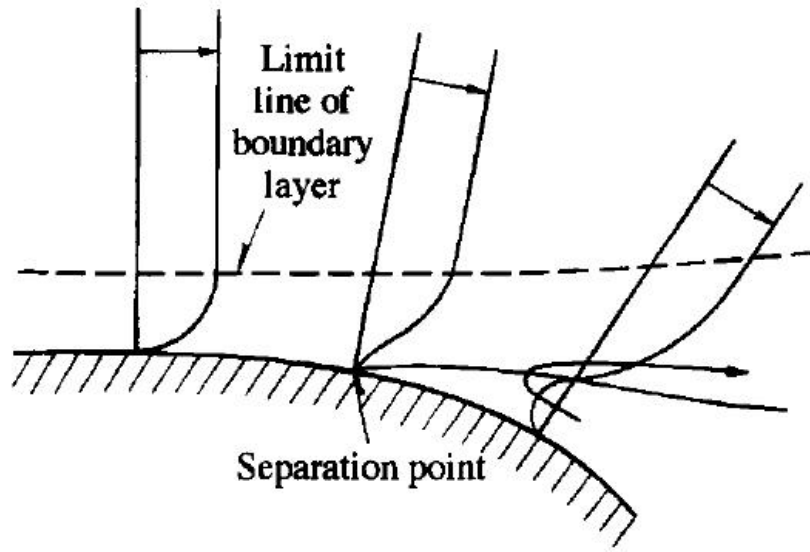


Figure 1.4: Flow Separation [2]

morphology was that an electrostatic body force is created by the plasma actuator which is proportional to the net charge density and the strength of the electric field; the body force is given by $f = \rho E = -\frac{\epsilon_0}{\lambda_D^2} \phi E$ where ϵ_0 is the permittivity of free space and λ_D is the Debye length.

Thus plasma actuators are attractive because they have no moving parts, involve no mass fluctuation to the system, are light and simple, can easily be installed anywhere, require little power, and can be turned on and off as part of an active or reactive system. The drawback to plasma actuators is their relatively low momentum imparting capability. As the knowledge in this technological field increases the momentum capability is sure to increase. Even though the momentum input at this

point is relatively small adding it in the right place at the right time can have large effects. It has been shown experimentally many times [8, 9, 10, 11, 12] that plasma actuators have the capability to delay or prevent separation.

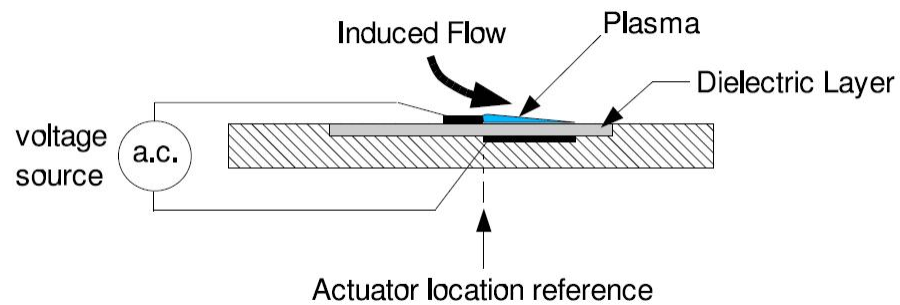


Figure 1.5: Typical Plasma Actuator Construction [3]

1.3 Previous work

Innovative methods for flow control have been investigated over the years, and a slough of research can be found on a myriad of flow control devices. A broad range of these devices will now be reviewed concluding with research performed on plasma actuators, the focus of this present work.

1.3.1 Compressor Flow Characterization

Of particular interest to this present work was research performed by Prato et al. [13] which was performed on the same experimental setup as this present research. In their work Prato et al. characterized the 3-D wake of the trailing edge of the compressor rotor blades using a five hole probe arrangement. They observed higher total velocity defects in the hub-wall region and increased wake growth rate in the tip region.

Braunscheidel et al. [14] experimentally demonstrated the effects of synthetic jets acting on the suction surface of a compressor stator vane. This was done by a row of spanwise injection slots along the length of the blade actuated by an external acoustic driver. The effects on a separated flow field at different velocities and excitation frequencies were explored. The system was evaluated using Total pressure loss reductions across the blade passage. The results showed a weak dependence on the beneficial effect due to the excitation frequency and a strong dependence on the amplitude at all frequencies. Loss reductions up to 22% were demonstrated at given span locations, and a loss reduction of 5.5% was seen for the entire passage.

Kefalakis et al. [15] performed studies on an axial compressor where 1% of the mass flow rate was used as a tip injection medium. Steady and pulsating jets were studied as a means to inject momentum at the compressor blade tips. Injection air angle, quantity, velocity, pulsating frequency, and pressure were all varied in this study. A 10% increase in stall surge margin was achieved.

Gbadebo et al. [16] studied the effects of suction on a compressor cascade both computationally and experimentally. Their goal was to model and prevent the 3-D separation over the suction surface and at the end wall corner of the blade passage. The numerical analysis displayed that by using 0.7% of the mass flow rate of the compressor as bleed air that the increases in stagnation pressure and static pressure rise were, respectively, worth about 1.5 and 4 times the loss in work for the bled air.

Nguyen et al. [17] studied separation flow control on a stator cascade located

within a low speed axial compressor using air injection. The focus was to create an adaptive active flow control loop. A 1-D unsteady flow model was used which incorporated Euler's equations. The numerical simulation modeled the proposed flow configuration on the stator cascade, with further work recommended to validate with experimentation.

1.3.2 Plasma Actuators as a Flow Control Device

Gregory et al. [18] showed the effects of using plasma actuators to effectively switch a high momentum jet between Coanda attachment walls by inducing a flow asymmetry across the nozzle of the fluidic oscillator. This use of plasma actuation allows the device to effectively serve as a fluid amplifier. This plasma actuated fluidic oscillator has possible uses in flow control applications such as cavity resonance tone suppression, jet thrust vectoring, and enhancement of jet mixing.

Enloe et al. [19] performed force production measurements on plasma actuators configured with a single encapsulated electrode and an asymmetric electrode alignment. They experimented with the intent of being better able to describe the physics behind the momentum coupling during plasma actuation. The Dielectric Barrier Discharge (DBD) is known to operate as a two phase process; one on the positive-going portion of the high voltage AC waveform, and the other on the negative-going portion. Using high speed photography it was determined that approximately 97% of momentum coupling occurs during the negative-going discharge cycle of the actuation.

Patel et al. [20] showed the effects of using dielectric barrier discharge plasma actuators for flow control over an unmanned combat air vehicle wing. Control was implemented on the wing leading edge allowing longitudinal control without the use of a hinged control surface. This showed great feasibility for hingeless flight control for highly swept wings at high angle of attack flight conditions, where conventional flaps and ailerons are ineffective.

General studies of plasma between two parallel electrodes performed by Shyy et al. [21] modeled the effects of the dielectric characteristics, applied voltage, frequency, and the asymmetric configuration of the electrodes. This computational model considered the effects of these variables on the downstream flow velocities, by measuring pressure, and the heat transfer due to the plasma field. The model showed a clear dependence of the induced jet velocity of the applied voltage and frequency. The heat flux exhibited a similar dependence on the strength of the plasma.

Further modeling of a plasma actuator was performed by Jayaraman et al. [22] using a 2-D asymmetric actuator operating in Helium gas. The simulations revealed that the momentum coupling was primarily affected by the combination of factors such as the geometric arrangement, the waveform of the applied voltage, and dielectric material. The relationship of the sensitivity of the generated force of the plasma to the magnitude of the applied voltage showed a near cubic dependence for both the model in Helium gas and the observed experiments in air.

Gregory et al. [23] showed experimentally that the time-averaged force production of a dielectric-barrier discharge plasma actuator is independent of the density of the neutral particles. It is dependent upon the ion density, volume of the plasma, and the applied electric field. The results showed a linear relationship between force production and air pressure, with the force going to zero at vacuum conditions.

Leading edge separation control was modeled by Orlov et al. [12] using a space-time lumped-element circuit. This model of the plasma discharge physics compared well to some of the characteristic features of the discharge. An application of their model was studied both numerically and experimentally for a NACA 0021 airfoil. The airfoil angle of attack and the forcing frequency of the plasma actuator were varied in this study. Improvements to the airfoil flow characteristics at a post-stall angle of attack were noted in the numerical simulations with the plasma actuators. With steady plasma actuation stall was delayed by approximately two degrees of

angle of attack. During pulsed plasma actuation the stall angle was increased by as much as five degrees. Their computational results corresponded very well with experimentation.

Experiments were performed by Greenblatt et al. [24] on a flat plate and an Eppler E338 airfoil. Both were oriented with plasma actuators on the leading edges with the intent of controlling flow parameters at low flight Reynolds numbers ($3000 < \text{Re} < 50,000$). Steady actuation of the plasma was investigated as well as pulsed actuation where the parameters of duty cycle and forcing frequency varied systematically. Optimum reduced frequencies for increasing lift in post-stall conditions were approximately between 0.4 and 1. Profound differences were seen in response to the reduced frequency and the duty cycle between the flat plate and the E338 airfoil, clearly demonstrating the effects of the leading edge detail in low Re applications.

1.3.3 Turbomachinery Applications of Plasma Actuators

Van Ness et al. [25] proposed using the active flow control capability of a plasma actuator to reduce blade tip losses in a low pressure turbine. A 29.5% reduction in maximum pressure loss at an axial chord Reynolds number of 10^5 was achieved during actuation.

Wall et al. [11] performed experiments using a pulsed DC dielectric barrier discharge plasma actuator to reattach a separated flow of a highly loaded turbine blade suction surface. Using phase locked particle image velocimetry (PIV) he showed that at a pulse rate of 100 pulses per second the 70% velocity contour in the boundary layer was moved closer to the wall by 39%.

Doc Vo [26] modeled a circumferential plasma actuator on a compressor case near the compressor rotor to induce axial flow acceleration within the tip clearance gap region, with the intention of suppressing tip clearance flow responsible for spike formation and short length-scale rotating stall inception. His computational study

was carried out to optimize actuator location and required actuation strength required to achieve the desired effects. He showed that plasma actuation near the rotor leading edge and concentrated in the tip gap region most efficiently suppressed the criteria for spike stall inception. The simulations indicated that actuation effectiveness decreases with increasing compressor speed and that stronger actuation strength than that of conventional plasma actuators may be needed.

Wu et al. [27] outfitted a Teflon compressor case with plasma actuators in order to measure the efficiency increase of a subsonic axial compressor during actuation. They calculated the pressure rise coefficient and flow coefficient for the compressor test rig with and without plasma actuation to represent compressor performance. The experiment showed that, with plasma actuation, the mass flow coefficients near stall decreased by as much as 5.2% at a constant rotor speed.

Mabe et al. [10] tested airfoils of various sizes varying free stream velocity, angle of attack, and flap deflection angle. Two sets of data were presented: one where the plasma actuator was located at 5% chord and the other where the actuator was located just upstream of the flap, about 75% chord. It was determined that the input momentum was very weak and not sufficient to prevent separation at Reynolds numbers greater than 100,000. The plasma actuators used in the study only provided sufficient momentum to be effective at very low Reynolds numbers, such as those appropriate to micro-air-vehicles.

Van Ness II et al. [28] performed five-hole probe measurements and stereo PIV measurements on the tip gap of a turbine blade. A Pak-B Pratt and Whitney blade was cantilevered in a cascade of blades such that a gap existed between the measurement blade and the end wall of the test rig. The plasma actuator was located on the tip of the blade in the gap region and a variety of Reynolds numbers and plasma forcing frequencies were investigated. The results documented that the unsteady disturbances produced by the plasma actuator affected the circulation and positions of

the tip-gap and passage vortices.

Huang et al. [9] used a linear cascade of turbine blades to examine the effects of using plasma actuators for controlling separation. They characterized the flow using surface pressure, laser-Doppler velocimetry, and hot wire measurements. It was determined that unsteady actuation was more effective than the steady actuation at reattaching the separated flow, while using less power.

CHAPTER 2

EXPERIMENTAL SETUP

2.1 OSCAR facility

The Oklahoma State Compressor Aerodynamics Research Facility (OSCAR) was finalized in 2004 [29]. It is located in Room 059 of the lower basement of the ATRC. The OSCAR facility features a 1.5 stage low speed axial flow compressor with a casing radius of 18 in. The inlet consists of 43 guide vanes followed by 21 cambered and twisted rotor blades followed by a final stage of 25 stator blades. The principle purpose of this facility is to explore stall, surge, wake interaction and other unsteady aerodynamic and aero elastic phenomena found in axial compressors. A photograph of the compressor test rig can be seen in Figure 2.1.

The compressor rotor is driven by a 50hp US Electric motor (model R135A) and is capable of driving the compressor up to 1600 rpm. An inverter manufactured by ABB (model ACS600) is used to adjust the torque and speed control of the electric motor that drives the compressor rotor. A secondary fan, which controls the mass flow through the compressor, is located at the aft of the compressor assembly. A separate 50hp electric motor manufactured by US Electric (model 38-21-1750) is used to drive the secondary fan. The secondary fan operates at a constant 1750 rpm and pulls a nominal volumetric flow rate of up to 40,000 cfm. This volumetric flow rate equates to a total mass flow rate of 3059 lbm/min, at standard day conditions. A conical shaped plug located in the aft end of the compressor rig is used to control the mass flow rate. This plug is used to increase or decrease the mass flow rate by axially traversing into or out of the flow exit, effectively changing the exit area.



Figure 2.1: Photo of OSCAR facility

A National Instruments PCI-6071E series card provides data collection capability for the OSCAR facility. The data collection card(DCC) is capable of handling a sampling rate of 1.2 MHz. A BNC-2090 breakout box connects instrumentation on the OSCAR facility through a single cable to the computer. The computer program used to manage the data acquisition device was LabView.

2.2 Measurement Instrumentation

A digital tachometer composed of a Keyence laser head and amplifier (models LV-H35, 21A) relays a voltage signal to the DCC. A schematic of the measurement instrumentation system can be seen in figure 2.2. The laser head is mounted aft of the compressor rotor and stator stages. In the compressor casing where the laser mounts there is a hole which allows the laser beam to penetrate. There is a reflective strip mounted on the rotating hub which passes under the focused beam of the laser.

The voltage signal to the DCC changes as the laser passes over the reflective strip, thus allowing one to calculate the RPM and to have the capability of indexing the beginning and end of a rotation cycle.

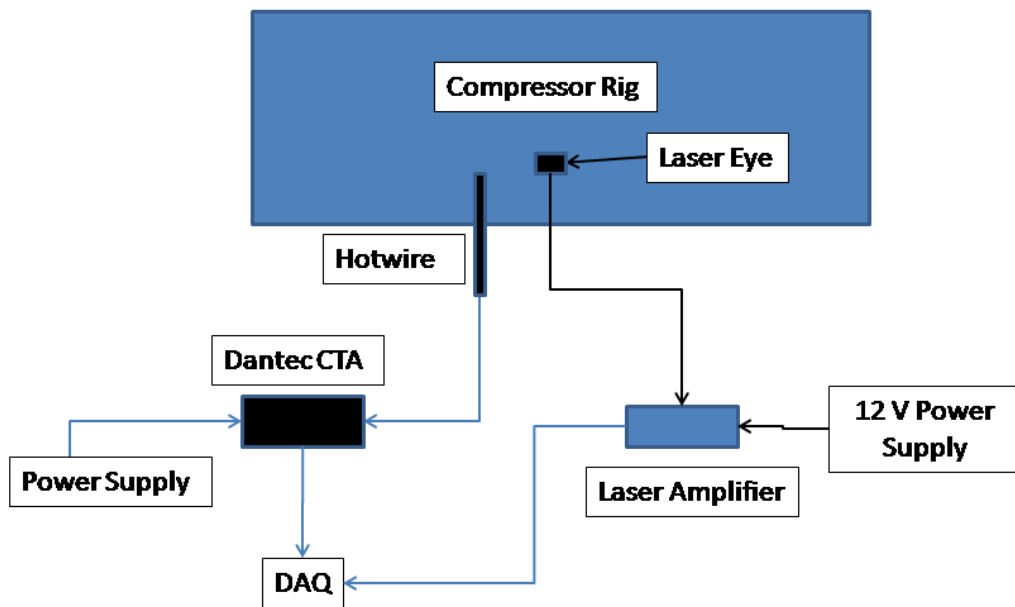


Figure 2.2: Schematic of Compressor rig instrumentation

A hotwire was used extensively during this research. The probe was mounted one chord length downstream of the compressor rotor trailing edge. The probe was mounted such that the immersion depth into the compression path could be varied. A schematic of the hotwire installation can also be seen in figure 2.2. A single normal sensor probe with a five micron welded tungsten sensor length of 1.2 mm and a Dantec

Mini CTA (Model 54T30) were used to transfer a voltage signal from the hotwire to the DCC. This voltage signal was then converted into a velocity value using the standard hot wire calibration process [30]. A schematic of the hotwire calibration process can be seen in figure 2.3. The controllable air jet assembly, manufactured by Dantec, was outfitted with a compressed air inlet and a pressure port. Compressed shop air was connected to the air inlet and a digital manometer, manufactured by Infiltec, was connected to the pressure port. To calibrate the hotwire the probe was mounted within a half inch from the calibration air jet, perpendicular to the flow. A lever on the air jet assembly allowed the user to adjust the strength of the jet, while the pressure port allowed measurement of the jet pressure. The jet pressure was set at a series of values between zero and three inches of H₂O as measured from the manometer, and the voltage output of the hotwire was recorded. The LabVIEW interface allowed the 10 kHz signal from the hotwire to be averaged once per second, and that was the hotwire voltage recorded. A sample of the calibration data can be seen in table 2.1. The velocity value was calculated using Bernoulli's equation, with a conversion factor from inches to meters. The resulting data in graphical form and the curve fit equation can be seen in figure 2.4. This equation and similar ones were used to convert the hotwire voltage data into velocity measurements for this study. Classical hotwire calibration is usually done using King's power law however according to Jorgenson [31] power law curve fits are less accurate than polynomial fits, especially over wide velocity ranges. Jorgenson recommends using a fourth order polynomial. The cubic polynomial curve fit equation displayed in figure 2.4 provided a correlation coefficient of 0.999 thus the cubic spline was deemed satisfactory.

2.2.1 Uncertainty of Hotwire Velocity Calculations

Uncertainty calculations were made on the hotwire data. The standard hotwire error calculations were followed using Dantec's practical guide by Jorgenson [31]. To

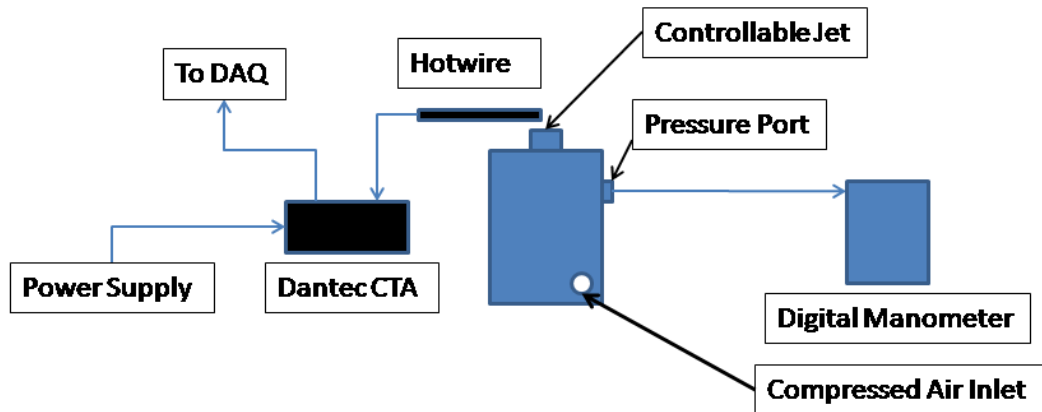


Figure 2.3: Schematic of Hotwire Calibration Setup

develop the total uncertainty of the hotwire velocity samples the vectoral sum of the relative uncertainties of the individual sources of error needed to be calculated. This was done using the below equation.

$$U(tot) = 2 * \sqrt{\sum u(y_i)^2}$$

where $u(y_i)$ is the relative uncertainty of the various error sources, and $U(tot)$ is the total uncertainty.

According to Jorgenson when a dedicated calibrator is used to calibrate a hotwire, similar to the one used in this study, the relative standard uncertainty is +/- 1.0%.

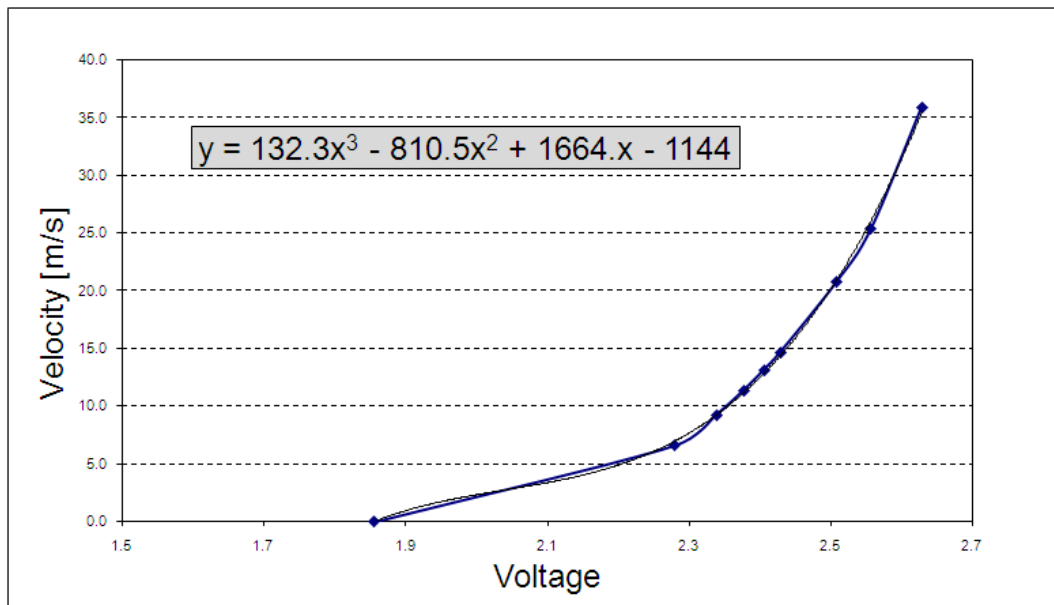


Figure 2.4: Hotwire calibration graph and curve fit equation

This uncertainty value only applies when measuring flows greater than 5 m/s, which is the case in this study. Jorgenson also provides a standard relative uncertainty for the linearisation conversion for the curve fit equation of $\pm 0.5\%$. The precision error of the hotwire data was calculated using the typical standard deviation method. An average standard deviation of a baseline run at 600 RPM was calculated to be $\pm 0.5\%$. The remaining sources of error of humidity, temperature variation, ambient pressure, probe positioning, and analog to digital conversion were neglected either due to their ability to be controlled during experimentation or due to their typically

Table 2.1: Hotwire calibration sample data

Voltage [V]	Velocity [m/s]	Pressure [in. H2O]
1.856	0.0	0.0
2.28	6.6	0.1
2.339	9.3	0.2
2.377	11.3	0.3
2.406	13.1	0.4
2.429	14.7	0.5
2.508	20.7	1
2.557	25.4	1.5
2.629	35.9	3

insignificant values.

Thus to calculate total uncertainty the above equation was used with the $u(y_i)$ represented in table 2.2. The total uncertainty calculated was +/- 2.5%, which provided a 95% confidence interval. This uncertainty is of a typical magnitude for hotwire measurements.

A graphical representation of this confidence interval is displayed in figure 2.5. This graph depicts the velocity values for average baseline blade velocity at 600 RPM, showing the error bars for a 95% confidence interval.

Table 2.2: Sources of error for velocity uncertainty calculations

Source of Uncertainty	$u(y_i)$ [+/-%]
Precision	0.5
Calibration	1.0
Linearisation	0.5
Total Uncertainty	2.5

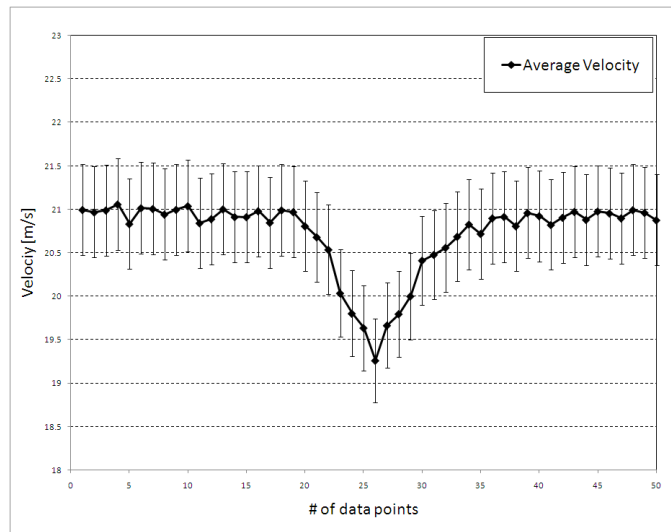


Figure 2.5: Uncertainty of Velocity measurements using hotwire

2.3 Data Retrieval and Signal conditioning

A software package called LabView was used to monitor, collect, and analyze data. The data received from the Laser and the hotwire was controlled through LabView using the front panel and block diagram found in Appendix A. This code was created in order to receive the data from the instrumentation, control the sampling rate, and write measurement files which were later used to analyze the data. Formulas were also incorporated into the code to provide real time data for flow velocities and RPM. The DCC sampling rate was adjusted using Labview. Sampling rates of 5 kHz to 50 kHz were used during the course of this research.

To analyze data in this quantity a Visual Basic for Applications (VBA) computer program was written [Appendix B]. This program performs a window averaging algorithm which takes data from several compressor revolutions and averages them. This allowed the velocity data downstream of the blades to go from the form of highly noisy in appearance to a well developed wake structure as seen in figures 2.6 and 2.7 respectively. It is of note that the velocity axis scale of the two graphs are the same. This window averaging technique allows the wake velocity to be visually and quantitatively compared. The pattern of the wake has a frequency of 21 cycles per window which coincides with the 21 blades of the compressor rotor per one revolution. Further programming was also done in VBA to perform an average of the wake velocity following each blade. The program allows the user to average the velocity in the wake of each rotor blade, allowing one to compare the differences of the wake between an average blade and a blade of interest. Take for example a sampling rate of 10,000 Hz and a rotor speed of 600 RPM, with 21 blades in the rotor this equates to 1050 blade passings in a 5 second sampling period. This also results in about 48 samples of data per blade passing. The VBA computer code takes all passings of an individual blade, one out the total of 21, and averages all 50 passings of that single blade in those 5 seconds. It accomplishes this for all 21 blades in the rotor.

The VBA program also performs momentum calculations. This was done using the equation below.

$$D' = \rho \int_{-y/2}^{y/2} U_2(U_1 - U_2)dy$$

where D' is the drag per unit length, U_1 is the free stream velocity, U_2 is the downstream velocity and ρ is the density of air. The integral was solved on a per blade basis using a numerical trapezoidal method.

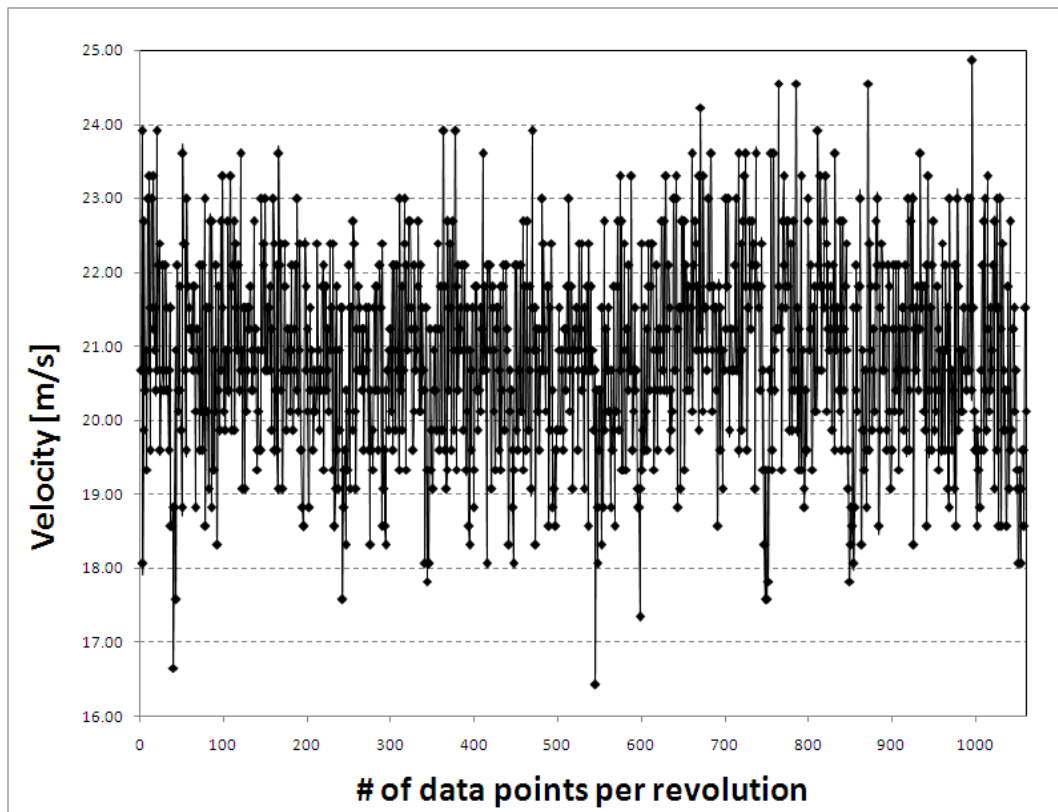


Figure 2.6: Velocity measurements of the rotor wake at 600RPM

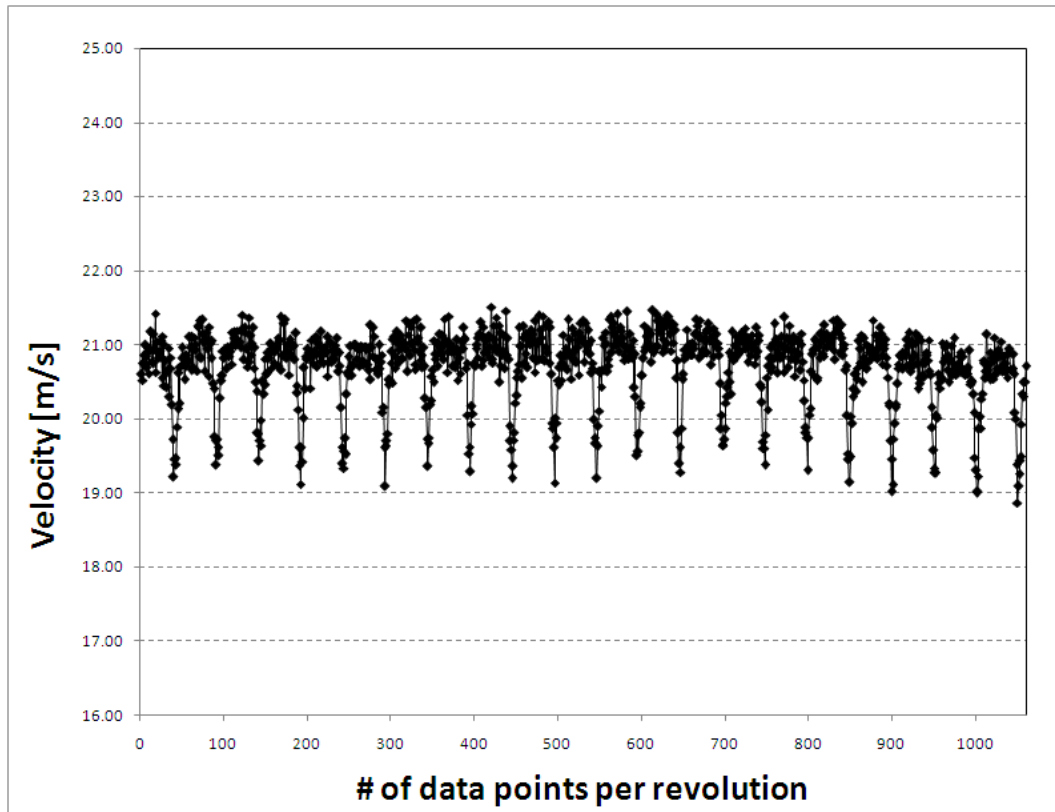


Figure 2.7: Window averaged velocity measurements of the rotor wake at 600RPM

2.3.1 Drag Calculation Uncertainty

The uncertainty for the drag calculations was determined using the VBA program. The drag for an average blade was calculated using average wake velocity data. The hotwire velocity calculation uncertainty of + 2.5% was then imposed on that average wake velocity data. The -2.5% wake velocity was processed through the VBA program and the drag was recorded. The +2.5% wake velocity was then processed as well and that drag value recorded. The resulting drag values displayed a range of 10% of the average blade drag. Thus it was determined that the drag calculation uncertainty

was +/- 5%.

2.4 Plasma actuator

2.4.1 Construction

Typical plasma actuators used in this research were constructed using a 0.5 inch wide copper strip as the exposed electrode and a 0.25 inch wide copper strip as the buried electrode. The actuators were constructed of varied lengths throughout the research. This research focused on the effect of linear actuators as flow control mechanisms in an axial flow compressor, thus all actuators used were linear. The dielectric material, which separated the two electrodes, was also varied throughout this research. Kapton of 0.002 inch thickness and .010 inch thick Teflon were used as dielectric materials.

2.4.2 Power and Control

To power the plasma actuator a high AC voltage must be used. This was accomplished using a transformer (Model MINIMAX7) which was powered using an MPJA DC power supply (Model 14601PS). This was the transformer and power source combination that was used throughout this research. The input to the transformer was varied throughout the experimentation and typically had values ranging from 12 to 15 volts with about one amp of current.

A rotating coupling connector manufactured by Mercotac (Model 230) mounted to the front of the rotor shaft was used to transfer power from the power supply to the transformer. The transformer was located in the inner hub of the compressor and was temporarily attached to the inner diameter of the hub using hook and pile. A 22 AWG multi-stranded wire was used to connect all components. To transfer power to the plasma actuator, located on a rotor blade, leads of varying conductive material were run from the inner hub through a port to the actuator. It was determined during

the exploratory analysis that leads with the lowest profile possible needed to be used, in order to reduce flow field interference.

It is common to use pulsed actuation when using a plasma actuator. Each new pulse creates a new vortex that advects downstream. Although the maximum velocity drops compared to the steady case the benefit is seen in the increase of turbulent kinetic energy created by the advected vortices, and by the decrease in power consumption. In this present study the plasma actuator was pulsed using a 5 V DC relay (SPDT Micromini) and a Tektronix function generator (Model CFG253). A photograph of the pulsed power setup can be seen in figure 2.8 and a schematic of the system can be seen in figure 2.9. The function generator delivered a square wave at various frequencies to the relay. The square wave was set at an amplitude of five volts and to a 50% duty cycle.

2.4.3 Calculating Forcing Frequency

For the inflow conditions at various regimes of laminar and turbulent cases, the scaling of dimensionless frequency of oscillation is important. Geometric parameters are often used to characterize the frequency of oscillation. Comparison between various methods can be achieved by using the forcing frequency as a dimensionless parameter. The physical significance of a reduced forcing frequency is related the amount of time it takes a vortex to travel the characteristic length, which in this case is the chord length at midspan. Thus at a reduced forcing frequency of one a new vortex is created when the previous vortex reaches the trailing edge.

$$F^+ = \frac{f L_{ssl}}{U_1}$$

where, F^+ is the reduced forcing frequency, f is the forcing frequency, L_{ssl} is the distance along the suction surface length from the leading edge of the blade to the location of actuation, and U_1 is the relative free stream velocity. The relative



Figure 2.8: Photograph of the pulsed power system

free stream velocity was calculated using the velocity triangle method as described in Mattingly [1]. Values of f ranging from 10 Hz - 50 Hz are used in this study, resulting in F^+ values seen in table 2.3. The forcing frequency to achieve the optimum reduced forcing frequency of one is also displayed in table 2.3.

In this study the reduced frequency was limited by the responsiveness of the transformer. Exploratory results showed that the output signal of the transformer ceased displaying a pulsed signal at input pulsing frequencies greater than 50 Hz.

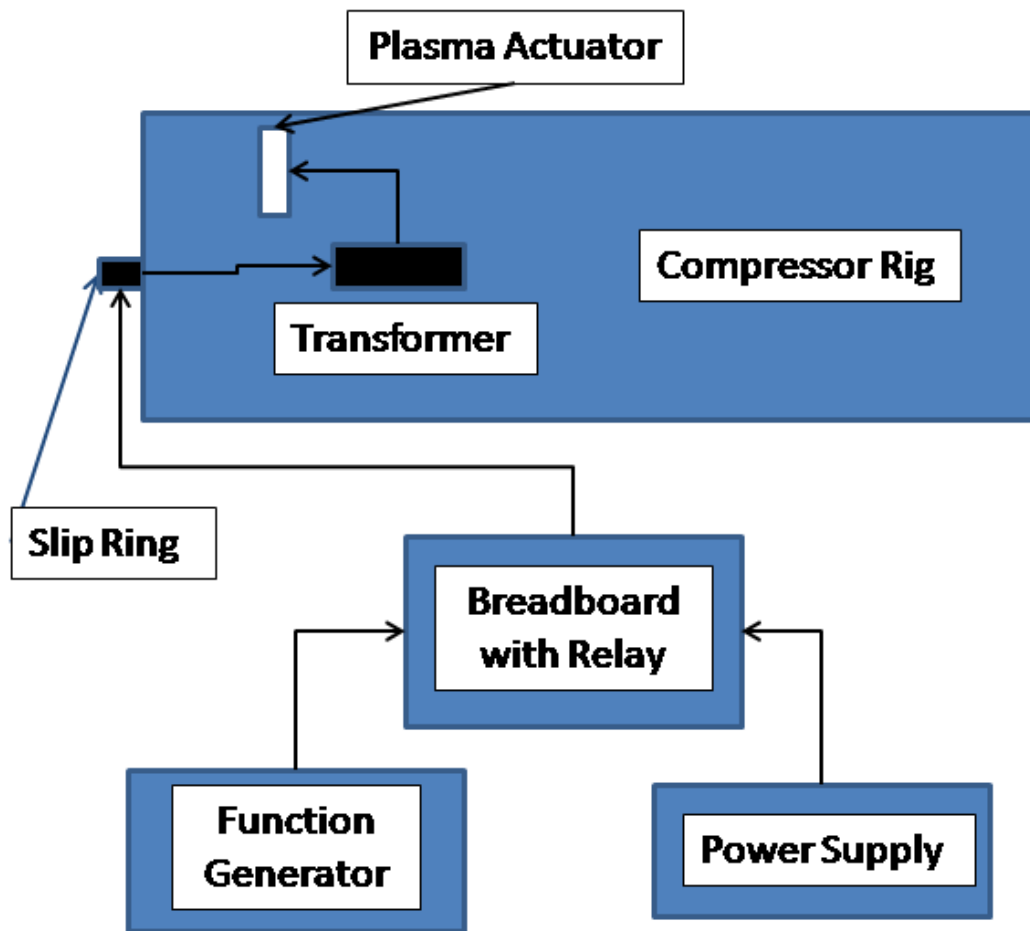


Figure 2.9: Schematic of the pulsed power system

Table 2.3: Reduced Forcing Frequencies at Various RPM and Forcing Frequencies

Forcing Frequency	350 RPM	600 RPM
$F = 10\text{Hz}$	0.071	0.050
$F = 30\text{Hz}$	0.214	0.150
$F = 50\text{Hz}$	0.356	0.250
$F^+ = 1$	140 Hz	200 Hz

2.4.4 Application to Compressor Blades

Once the actuators were constructed they were adhered to a compressor rotor blade using an adhesive tape, with the plasma region located at various chord locations throughout the research [Figure 2.10]. An actuator can be seen during actuation in Figure 2.11, and the same actuator can be seen with low ambient lighting conditions in Figure 2.12.



Figure 2.10: Plasma actuator on a compressor blade: approx. $1/4$ chord

2.5 Particle Image Velocimetry Setup

Particle Image Velocimetry (PIV) is a whole-flow-field technique providing instantaneous velocity vector measurements in a 2-D cross-section of the flow. In PIV, the velocity vectors are derived from sub-sections of the target area of the particle-seeded flow by measuring the movement of particles between two light pulses. The flow field is infiltrated with small tracer particles which are carried by the flow, and are tracked from one image to the other. A laser light sheet is used to illuminate the target area. The time between the images captured is known, and PIV algorithms are used to

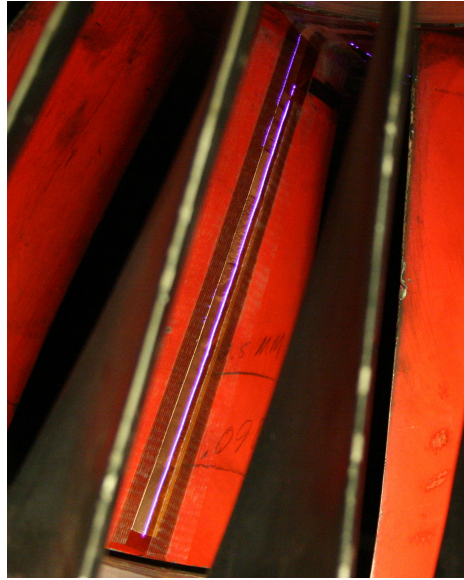


Figure 2.11: Plasma actuator on a compressor blade with visible plasma

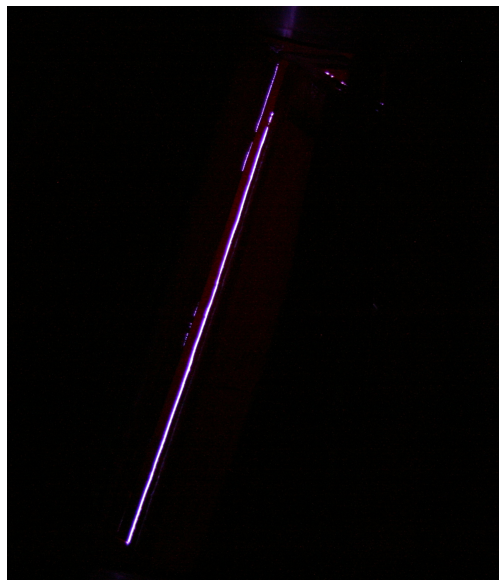


Figure 2.12: Plasma actuator on a compressor blade with visible plasma in low ambient lighting

compute the particle velocities. A schematic of the PIV arrangement can be seen in figure 2.13.

The flow field is seeded with smoke particles of the order 1 micron in diameter, generated from a SAFEX 2010 fog generator. A 2-D light sheet is projected in the

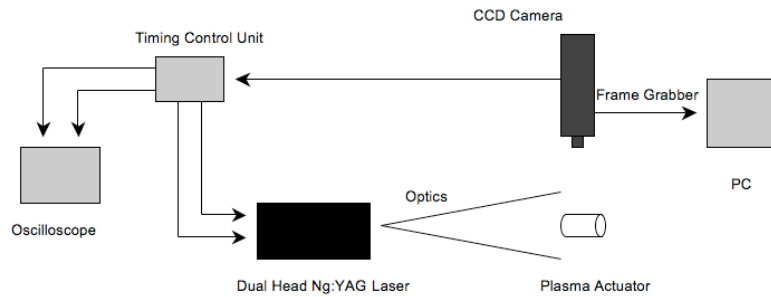


Figure 2.13: Schematic of the PIV setup

plane of the tunnel at the mid-actuator using a dual-head 50 mJ Nd-YAG laser from New Wave Research (Solo PIV III). The light sheet is aligned and adjusted using a series of 3 lenses. First, the beam emitted from the laser is focused using a converging lens. The second in the series is a diverging lens, placed at the focal length of the first (converging) lens, and serves to create a more concentrated, thinner beam. The third lens in the series is cylindrical, and spreads the beam into a 2-D sheet with a thickness of approximately 2 mm. The laser is pulsed in sync with a Kodak Megaplug ES 1.0 CCD camera which has 1008 x 1018 pixels. A timing control unit from Taitech allows time between a pair of pulses from 1 μ s to 1 ms. The camera is placed in multiple locations above the cascade.

The CCD camera is able to capture each light pulse in separate image frames. Epix frame grabbing hardware and software is used to acquire binary image pairs for processing. For each run, 124 images are captured at a rate of 10 Hz. Fluid parcels

registered by CCD pixels are advected with individually estimated velocities and total accelerations. A Wall Adaptive Lagrangian Parcel-Tracking algorithm (WaLPT) developed by Sholl and Savas [32], is adopted to track the fluid parcels. A standard DPIV algorithm is employed to determine the initial velocity field, and the routines in WaLPT allow for more accurate measurement of the velocities near the wall by essentially mirroring the flow about the interface using an image parity exchange (IPX) routine.[33] IPX reverses the flow on the other side, providing a group of particles under the surface. With IPX turned on, the interrogation windows can be extended across the surface, allowing the calculation of near-wall velocity. Velocity and reverse flow probability fields obtained in post-processing are averaged over the entire run. The surface is masked using XCAP resulting in a higher accuracy of the wall derivatives providing better boundary layer calculations. The PIV computer code can be found in the thesis by Ramakumar [34].

2.6 Determining Re and Actuator Placement for Experimentation

Preliminary studies were completed to theoretically determine the optimum area of interest for this study. The main area of study was to do determine the chord wise location and corresponding Reynolds number at which separation occurs on the subject compressor blade configuration.

2.6.1 XFOIL Results

According to Hanson [29] the compressor blades used in the OSCAR facility are based on a modified NACA 65-010 airfoil. A program named XFOIL was used to analyze flow conditions over the NACA 65-010 airfoil. XFOIL is an interactive program for the design and analysis of subsonic isolated airfoils [4]. The coordinates for the NACA 65-010 airfoil needed to be loaded into XFOIL, thus the x and y coordinates were generated using a source code found on the University of Illinois website [35].

Once the airfoil coordinates were loaded into XFOIL the Reynolds number and angle of attack seen by the airfoil were systematically varied with results seen in figure . To determine the relative Reynolds number for the compressor rotor at various angles of attack the velocity triangle method was used [1]. These velocities were then used to calculate the Reynolds numbers which coincided with the proper span wise location. It will later be seen in this study that the operating RPMs of 350 and 600 became points of interest, which correlate to Reynolds numbers of 170,000 and 260,000 respectively. Once the relative velocities were determined the effective angles of attack could also be calculated using the method in Mattingly. Angles of attack of six and 20 degrees were calculated for the 350 and 600 RPM cases respectively at the midspan location with the mass flow fan in operation and with the conical plug set as described in the experimental results. It was determined for the NACA 65-010 airfoil at the specified Reynolds numbers that separation was mostly a leading edge phenomenon. The XFOIL results can be seen in figures 2.14 and 2.15 for the 350 and 600 RPM cases respectively. XFOIL was also used to determine the size of trip which was necessary to effect the flow at the subject operating conditions. This was done by examining the dump files to extract the boundary layer displacement thickness δ^* . These dump files can be found in Appendix C. The resulting δ^* values can be seen in table 2.4. They were calculated by re-dimensionalizing the XFOIL δ^* values using the midspan chord length as a multiplier. It was determined that a 1/16 inch (0.00159 meter) thick trip was sufficient to cause a trip to the boundary layer in both the 350 and 600 RPM flow regimes. A trip of 0.00159 meter thickness was determined to be about nine times the greatest boundary layer displacement thickness.

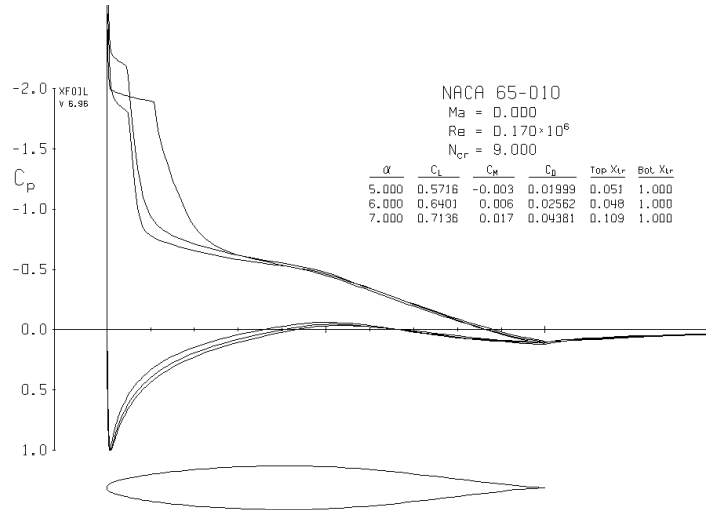


Figure 2.14: NACA 65-010 at various angles of attack for 350 RPM case [4]

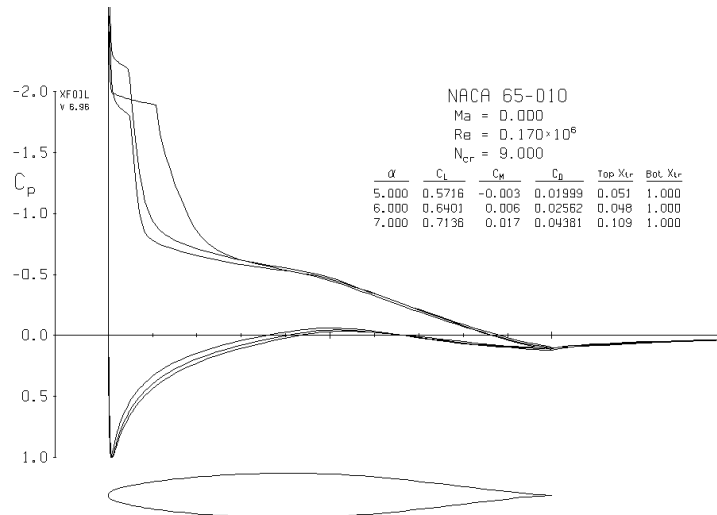


Figure 2.15: NACA 65-010 at various angles of attack for 600 RPM case [4]

Table 2.4: XFOIL Calculations for Delta Star at 350 and 600 RPM

Delta Star [m]	350 RPM	600 RPM
1/4 Chord	7.35 E -6	175 E -6
Leading Edge	9.8 E -6	58.87 E -6

CHAPTER 3

EXPERIMENTAL RESULTS

3.1 Exploratory Results

3.1.1 Quiescent Plasma Actuator Characterization

The plasma actuators tested in the quiescent state were done so such that their construction would mirror that which was used in the compressor rotor application. This required that the plasma have an eight inch operating length. The actuator was constructed using a 0.5 inch wide eight inch long copper strip as the exposed electrode and a 0.25 inch wide eight inch long copper strip as the buried electrode. Kapton of 0.002 inch thickness and .010 inch thick Teflon were used as dielectric materials.

During quiescent experiments the voltage and amperage from the transformer was measured. The voltage was measured using a Northstar voltage probe (Model PVM-1) with a 1000:1 scaling factor. Amperage was measured using NK Technologies AC current transducer (Model AT2-010) which was set at a range of 0 to 200 amps for a range of 0 to 10 volts output. Both measuring devices were connected with a BNC cable to a Tektronix digital oscilloscope.

The actuators were powered using a transformer. The input and output of that transformer varied, dependent upon the dielectric material. The power required by both configurations of actuator, the Kapton and Teflon dielectric, showed some differences. As can be seen in Table 3.1 the Teflon actuator configuration required less power at the 15 volt setting, drawing only .85 amps. The Kapton actuator drew one amp at the 15 volt setting. The Teflon configuration also had a higher peak to peak

voltage signal when measured after the transformer. The higher peak to peak voltage can be attributed to the lower dielectric constant that Teflon has over Kapton. Its voltage was nearly twice that of the Kapton configuration as can be seen in comparing figures 3.1 and 3.2.

Table 3.1: Power usage by plasma actuators using Kapton and Teflon as dielectric

Parameter	Teflon	Kapton
Voltage(V)	15	15
Current(A)	0.85	1.0
Power(W)	12.75	15

The plasma actuator configurations were characterized in the quiescent state using particle image velocimetry (PIV). The actuator was mounted in a semi-enclosed state to prevent random airflow from affecting the PIV results. The mounting orientation, enclosure, and laser setup can be seen in figures 3.3 and 3.4.

It can be seen in the velocity profile diagrams figure 3.5 for Kapton and figure 3.6 for Teflon, that the actuators produced a wall jet in the boundary layer region. This resultant momentum was input in the region within one centimeter from the surface. Figures 3.5 and 3.6 display velocity profiles for the Kapton and Teflon dielectrics with steady plasma actuation. In these figures it can be seen that the Kapton configuration only produce a maximum velocity of about 5 cm/s while the Teflon configuration produced a maximum velocity of about 40 cm/s. Figures 3.7 and 3.8 display velocity profiles for the same arrangement but for a forcing frequency of 50 Hz. These figures display that a maximum velocities of about 3 cm/s and 9 cm/s were seen on the Kapton and Teflon configurations respectively. The Teflon dielectric configured actuator displayed the better performance at a lower power consumption level. This was explained by the amount of peak to peak voltage that was inherent to the Teflon configuration due to its lower dielectric constant. Although the Teflon configuration

required less average power the instantaneous power was greater due to the elevated driving voltage over the Kapton configuration. It is also of note that each of the velocity profiles display a time averaged velocity. This averaged velocity typically displays fluctuations up to 30%. Thus the jet is not a constant laminar jet, it fluctuates significantly which actually proves beneficial due to its effect as a turbulator. This increase in turbulence adds momentum to the flow by increasing the turbulent kinetic energy in the boundary layer.

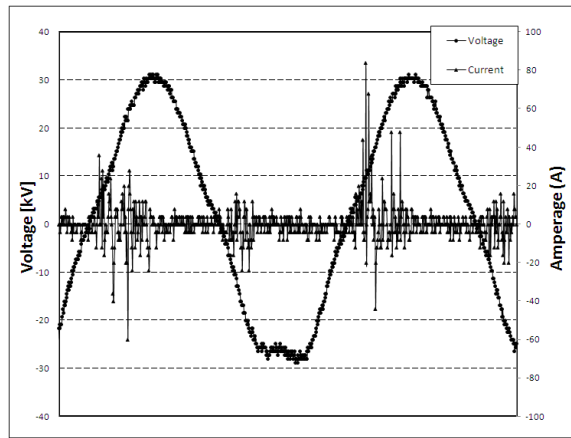


Figure 3.1: Voltage and amperage on a plasma actuator with Teflon as dielectric

Momentum calculations were performed on the PIV measurements to characterize how much momentum was being imparted to the flow. This momentum calculation was carried out in the same manner as the drag calculations referred to in section 2.3. The momentum deficit of an average blade wake was also calculated using this method. The momentum deficit for an average blade at 600 RPM was calculated to be 0.6012 N/m. The momentum addition for both the Teflon and Kapton configurations during steady actuation can be seen in table 3.2. It was calculated that the Teflon configured actuator contributed a magnitude of 0.1075% of the blade wake momentum deficit.

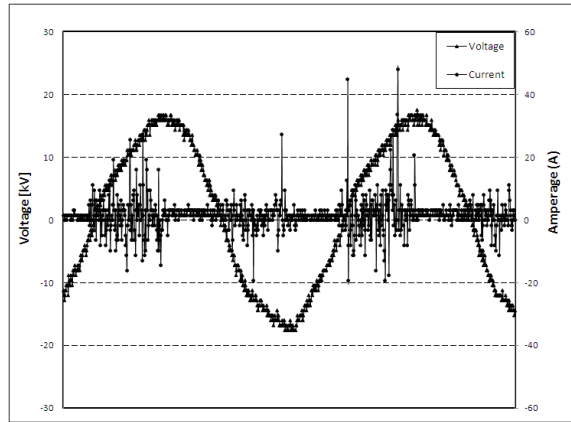


Figure 3.2: Voltage and amperage on a plasma actuator with Kapton as dielectric

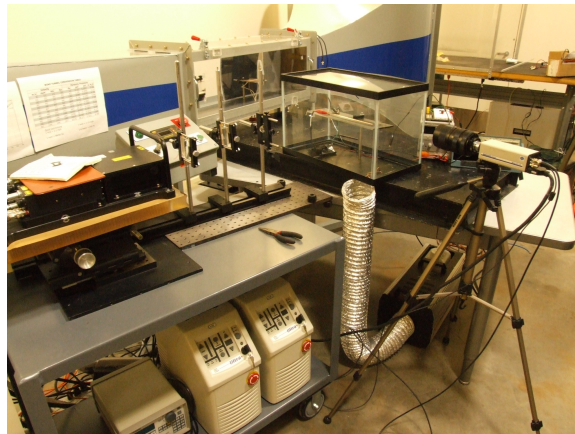


Figure 3.3: Quiescent PIV Laser setup

3.1.2 Baseline Data

All preliminary results that will be described below were achieved by operating the rotor at a variety of RPM with the mass flow fan in operation at a constant RPM. Data collection was initiated using the Labview code, which wrote measurement files for both the laser and hotwire signals. The measurement files were then imported into

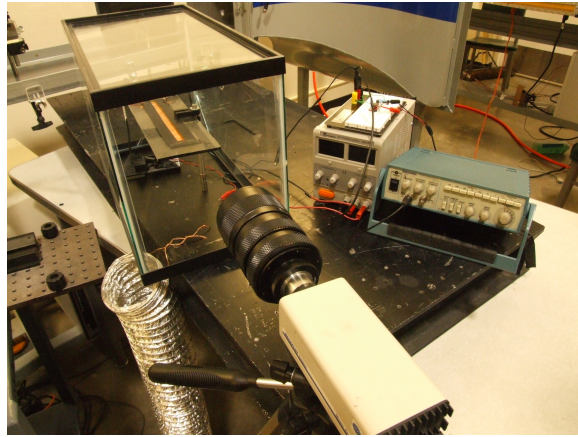


Figure 3.4: Quiescent PIV mounting orientation

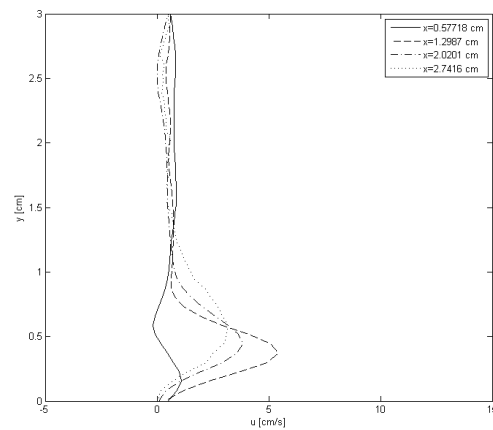


Figure 3.5: Quiescent Velocity profiles for steady plasma actuation with a Kapton dielectric

Excel where the VBA computer program performed the data analysis. The conical plug which controls the mass flow on the OSCAR setup was kept at roughly a one inch opening. This provided the mass flow rate which the preliminary analysis showed as the optimum area of interest. The preliminary hotwire results were taken one chord

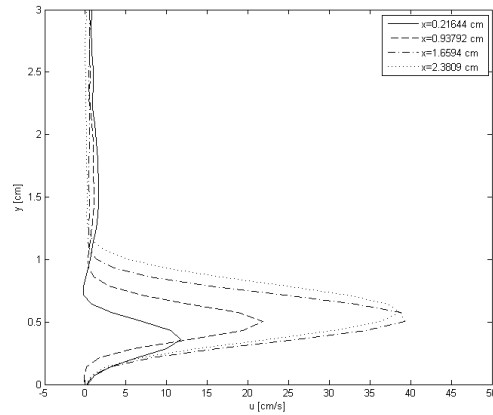


Figure 3.6: Quiescent Velocity profiles for steady plasma actuation with a Teflon dielectric

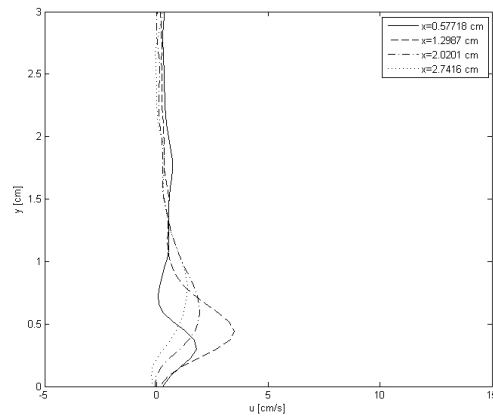


Figure 3.7: Quiescent Velocity profiles for pulsed plasma actuation with a Kapton dielectric at $F = 50$ Hz

length downstream with an immersion location at one half span. The compressor was run at 200, 400, and 600 RPM and baseline data was taken. It can be seen in Fig 2.7 that the wake structure at 600RPM was very organized and well defined. As the

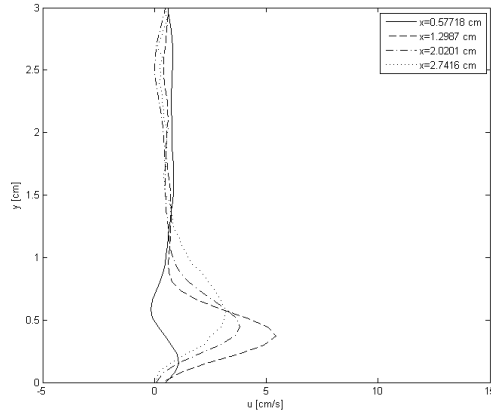


Figure 3.8: Quiescent Velocity profiles for pulsed plasma actuation with a Teflon dielectric at $F = 50$ Hz

Table 3.2: Momentum characterization of various configurations

Parameter	Momentum D' [N/m]	% of Blade wake
Average Blade wake	-0.6012	1.0
Teflon	6.46 E-04	0.1075
Kapton	0.083 E-04	0.0014

RPM went up or down from this point the signal became less organized. It can be seen in figures 3.9 and 3.10 that there is a poorly defined wake pattern at 250 and 700 RPM respectively.

3.1.3 Mechanical trip

To verify that the VBA data processing program was working correctly a mechanical trip was installed on one of the blades. A 3/16 by 1/16 by 5 in. long strip of plastic was adhered to the suction side of one of the compressor blades using aluminum tape. As described earlier this trip height was analytically determined to be sufficient to

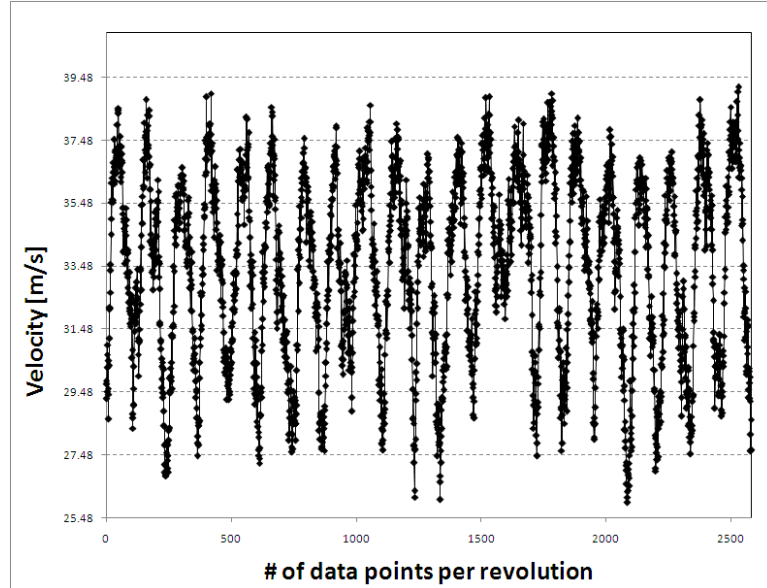


Figure 3.9: Velocity measurement at 250 RPM, displaying poor wake structure effect the boundary layer for both the 350 and 600 RPM cases. It was located at approximately one quarter chord as can be seen in figure 3.11. It was verified in the post processed data that the trip was visible. There was a large momentum deficit in the wake of the trip blade, and the tripped blade was located at the expected point in the data. Preliminary runs with the compressor RPM set at 200, 400, and 600 were performed. The best wake structure and trip response was seen at the 600 RPM level thus this operating region became a point of interest.

3.1.4 Plasma actuator as a steady trip

The initial test to determine the effect of a plasma actuator was performed using a five inch long actuator with the plasma region located approximately at quarter chord on the suction side of one blade. The actuator was configured such that the momentum input was actually counterflow to the compressor flow field as seen in

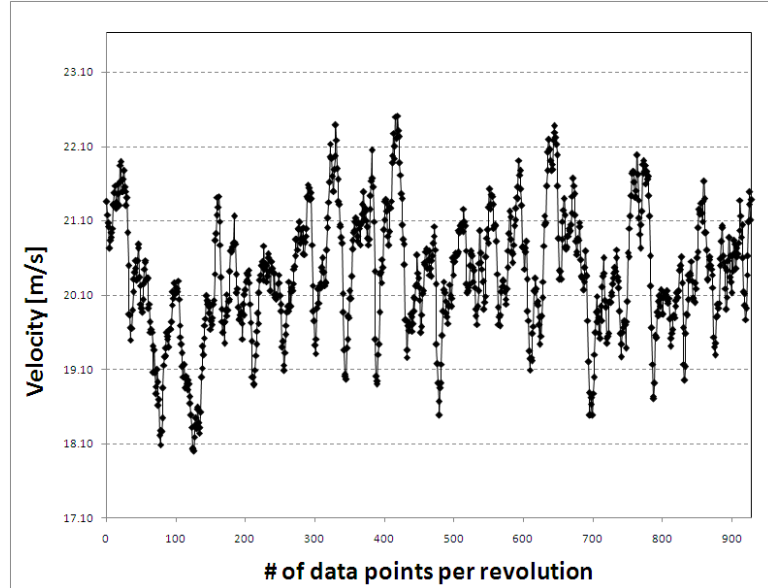


Figure 3.10: Velocity measurement at 700 RPM, displaying poor wake structure figure 3.12. The typical orientation for actuators is in the co-flow direction, as seen in figure 3.13. Thus the counterflow actuator can act as a steady trip when powered. The plasma was powered by the transformer using a 15 volt input. Data was recorded at 600 RPM with the plasma both on and off. The leads connecting the transformer to the plasma actuator were two 22 AWG multi-stranded wires. These ran from the actuator to the hub interior, where the transformer was located. They were adhered near the root of the blade in an attempt to minimize flow field interference.

At 600 RPM it was noted that the counterflow plasma actuator acted as a trip similar to the mechanical trip which also remained installed. As seen in figure 3.14 the actuator was located on the eighth wake position while the mechanical trip was located on the 11th wake position.

It was also of interest that the flow seemed to speed up in the blade passage directly following the actuated blade, as can be seen in figure 3.14. This was later determined



Figure 3.11: Mechanical trip installed at 1/4 chord

to be due to the wires which were used to power the actuator. Although they were adhered near the root of the blade to minimize flow interference their presence was still visible in the measurements. When they were replaced with flat copper strips in subsequent testing the blade passage profile returned to normal. It was reasoned that the wires had a throttling effect on the flow in the subject blade passage by slightly decreasing the blade passage area.

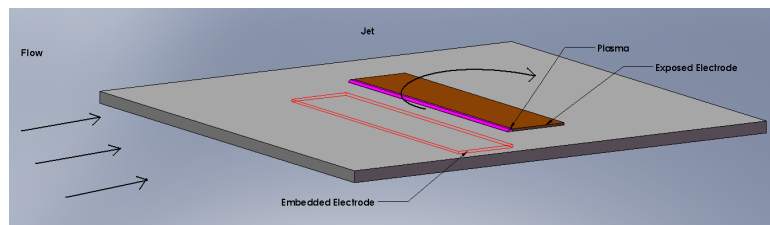


Figure 3.12: Plasma actuator in a counter flow orientation

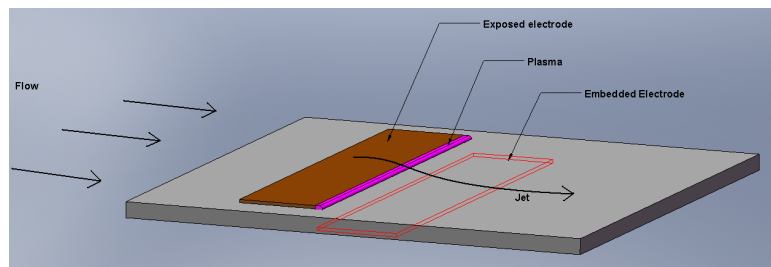


Figure 3.13: Plasma actuator in a co-flow orientation

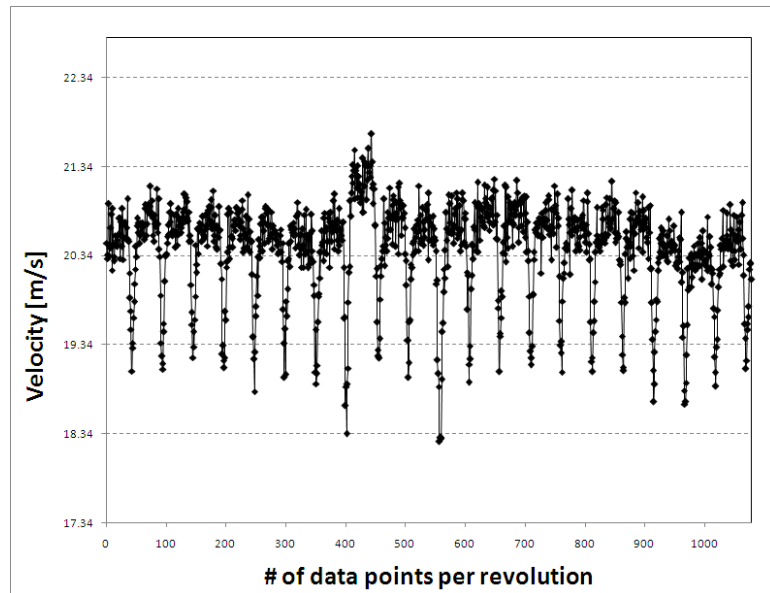


Figure 3.14: 600 RPM steady plasma actuation at 1/4 chord

3.2 Parametric Results

The parametric study focused on two areas of interest. With the conical plug in a fixed position and the mass flow fan at a constant RPM the designed operating range was estimated using the exploratory results. It was reasoned that if the mechanical trip was not visible in the window averaged data that the boundary layer was such that the momentum imparting capabilities of the plasma actuator would have little effect. The mechanical trip was only clearly visible in the data between 350 and 600 RPM, thus the parametric study focused on the upper and lower ends of this operating regime. Based on previous work done by Visbal et al. [36] that showed a counter-flow actuator can provide an effective on-demand boundary-layer tripping device. Visbal surmised that this property could be effective for the control of laminar separation. Thus the counter flow orientation was explored as well. In the preliminary studies it was determined that for Reynolds numbers between 15×10^4 and 30×10^4 that separation was generally a leading edge phenomenon. Thus for the parametric study actuators were placed at 1/4 chord and as close to the leading edge as the actuator configuration would allow, which equated to about the 1/15 chord location.

The actuators were powered at the same magnitude as the exploratory results. All actuators used in the parametric analysis incorporated the Teflon dielectric which resulted in a 15 volt, .85 amperage draw from the power source. This was the power that drove the transformer to its 30 kV performance.

It will be seen in the parametric results that the effect of the plasma actuators on the compressor flow was compared using a percent change in drag. These drag values were calculated using the aforementioned D' equation multiplied by the actual blade span. Thus the drag values compared were no longer per unit length. The percent change in drag was calculated by taking the difference between the subject run at

one of the given forcing frequencies and the actuator blade with the actuator turned off. That difference was then taken as a percentage of the non-actuated plasma blade drag value. This was done in order to remove the physical presence of the actuator on the blade as being a contributor to the drag increase, thus making the non-actuated blade the baseline blade for comparative purposes. A positive value of D denotes a decrease in the total drag of the compressor rotor blade, and a negative value denotes an increase in drag. For comparison purposes the drag was calculated for the mechanical trip at both the 350 and 600 RPM cases and was found to have a negative change in drag of 7% and 28% respectively. Thus at 350 RPM the tripped blade had a 7% increase in drag over the non actuated plasma blade and at 600 RPM the tripped blade had a 28% increase in drag over the non actuated plasma blade.

The majority of the following graphs contain velocity quantities versus the number of data points averaged. An alternate way to present the data would be to graph the velocity quantity versus the tangential distance normalized by the blade spacing $[Y/S]$, which would locate $y = 0.5$ at the wake center. This alternative method is depicted in figure 3.15.

Figure 3.15 compares a non actuated plasma blade with an average blade and the blade with the mechanical trip. It can be seen that the mechanical trip has a much greater velocity deficit in the blade wake than the average and non-actuated plasma blade. In this figure and all that follow that contain an average blade plotted against the plasma blade it must be understood that the average blade contains twenty times the amount of realizations in the average than the subject blade. Take for instance the 600 RPM case shown in figure 3.15. At 600 RPM the subject plasma blade passes the hotwire 50 times in the five second sample. Thus the plasma blade consists of an average with 50 realizations. The average blade on the other hand consists of the remaining 20 blades in the rotor, thus for the same five second sample 1000 blades pass the hotwire. Thus the average blade consists of an average with 1000 realizations.

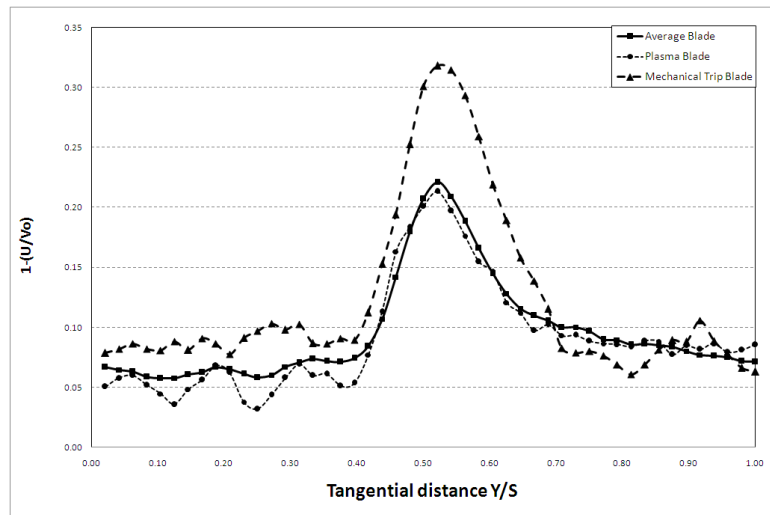


Figure 3.15: Wake velocity per blade for the mechanical trip blade, and average blade, and a non-actuated plasma blade at 600RPM

3.2.1 Counter and Co-Flow Results for 600 RPM at Various Forcing Frequencies

The first set of results were achieved with the rotor RPM set to 600, which equated to a Reynolds number of about 2.6×10^4 . The data was sampled at 10 kHz and analyzed using the window averaging computer program. The forcing frequency was varied using forcing frequencies of 10 Hz, 30 Hz, and 50 Hz. Data was also sampled with the actuator off and in steady actuation. The hotwire was located at the midspan location, one chord length downstream. Results were taken with the actuator at 1/4 chord and at the leading edge locations.

600 RPM 1/4 chord results

A summary of the drag data for both flow orientations can be seen in figure 3.16 for the 1/4 chord actuator configuration at 600 RPM. The graph shows the change in percent delta D for various forcing frequencies. The data reveals that the counter flow orientation increases the drag in the wake of the plasma blade with increasing forcing frequency. It also shows that for the co-flow orientation that as the forcing frequency increases so does the decrease in drag. It is of note that at a forcing frequency of 10 Hz and at zero Hz, which signifies steady plasma operation, the percent change in drag is negative. This signifies that there is a drag increase on the plasma blade at these forcing frequencies.

The individual graphical results for the counter flow orientation can be seen in figures 3.17(a) through 3.21(b) for both the entire rotor revolution and for the plasma blade itself for the 1/4 chord cases run at 600 RPM. In this group of figures the plasma blade wake is located in the eighth blade position and the mechanical trip remained installed on the eleventh blade position. It can be seen in these figures that mechanical

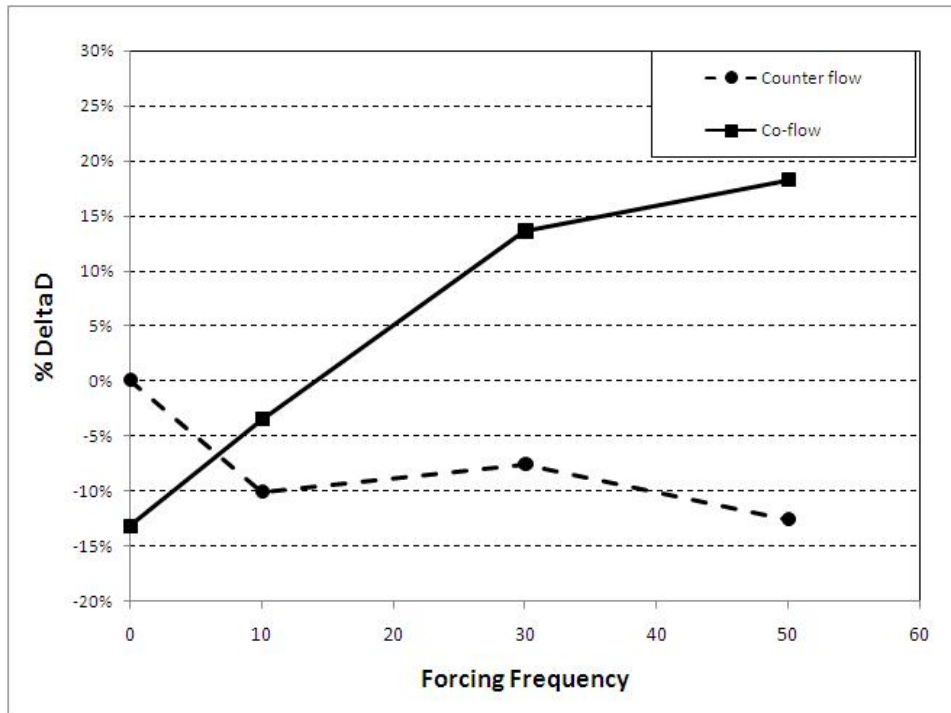
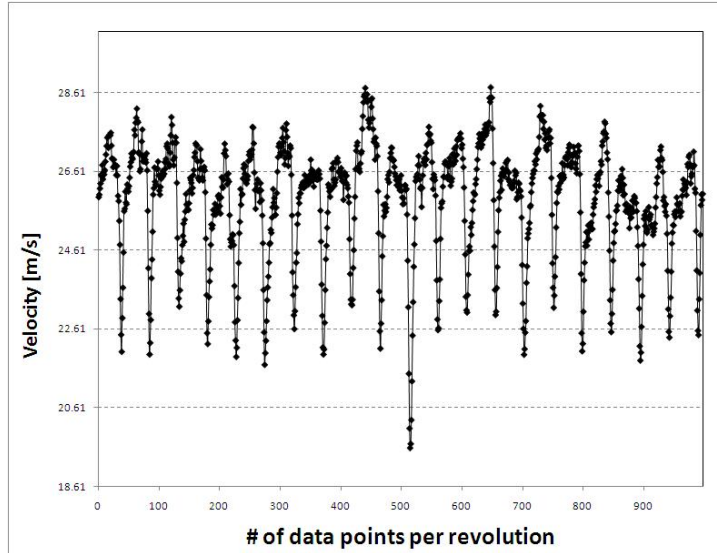
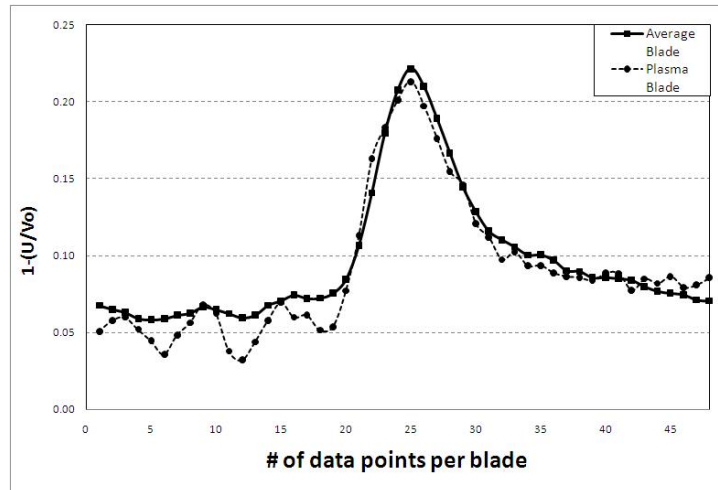


Figure 3.16: Drag variations at various forcing frequencies for 600 RPM with Plasma at 1/4 Chord

trip is visually evident. It can also be seen in the plasma blade wake measurements that there is a velocity decrease evident on the suction side of the blade wake. This would coincide with the actuator being located on the suction surface, and it acting to remove momentum from the flow.



(a) Wake velocity per revolution



(b) Wake velocity for plasma blade

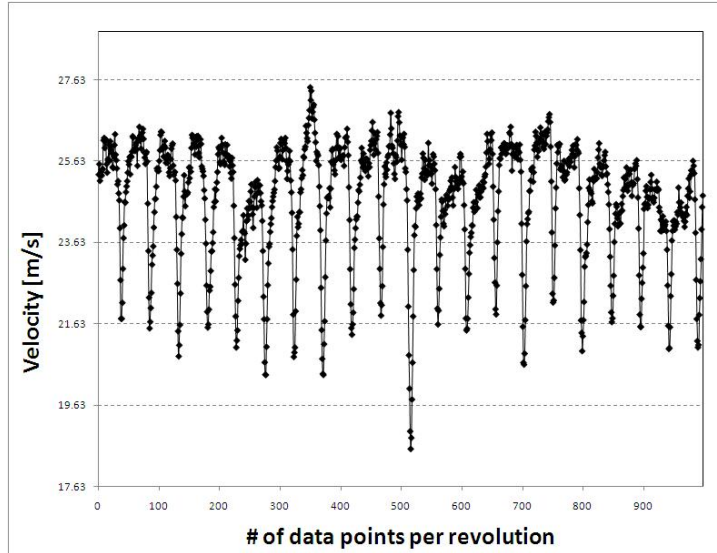
Figure 3.17: Wake velocity for 600 RPM per revolution (a), and per blade (b): 1/4 Chord Counter Flow Plasma Off

The individual graphical results for the co-flow orientation can be seen in figures 3.22(a) through 3.26(b) for both the entire rotor revolution and for the plasma blade itself for the 1/4 chord cases run at 600 RPM. In this group of figures the plasma blade wake is located in the seventh blade position and the mechanical trip remained installed on the eleventh blade position. It can be seen in these figures that mechanical trip is visually evident. It can also be seen in the plasma blade wake measurements that there is a velocity decrease evident on the suction side of the blade wake for both the 30 Hz and 50 Hz case but none is evident in the steady or 10 Hz case. This would coincide with the actuator removing more momentum at the higher forcing frequencies.

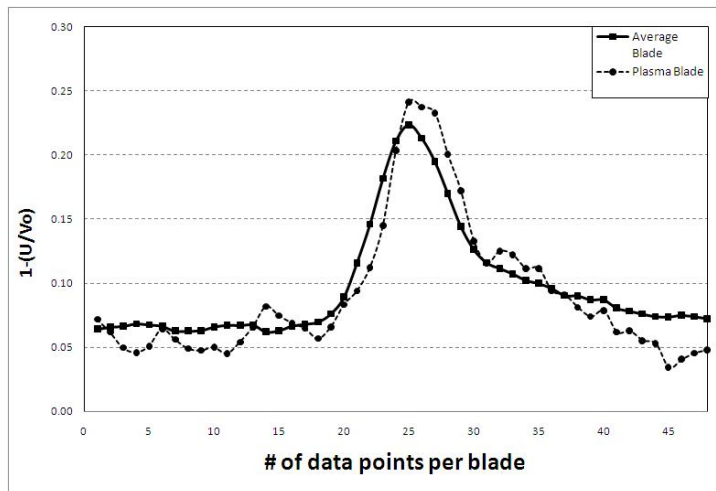
600 RPM Leading edge results

A summary of the drag data for both flow orientations can be seen in figure 3.27 for the leading edge actuator configuration at 600 RPM. The graph shows the change in percent delta D for various forcing frequencies. The data reveals that the counter flow orientation increased the drag in the wake of the plasma blade with increasing forcing frequency. It can be seen that there is a major increase in drag at a forcing frequency of 10 Hz. Results show that for the leading edge counter flow actuator at any forcing frequency had an unpredictable and deleterious effect on the blade wake. The graph also shows that for the co-flow orientation that as the forcing frequency increased the drag began to decrease. It is of note that at a forcing frequency of zero Hz, which signifies steady plasma operation, the percent change in drag was at its optimum for both the counter and co-flow orientations, and better than the baseline blade for the co-flow case. This could indicate that a pulsed leading edge actuator may be too disruptive to the flow at this Reynolds number, and may possibly encourage separation.

The individual graphical results for the counter flow orientation can be seen in figures 3.28(a) through 3.32(b) for both the entire rotor revolution and for the plasma blade itself for the leading edge cases run at 600 RPM. In this group of figures the plasma blade wake is located in the eighth blade position and the mechanical trip remained installed on the eleventh blade position. It can be seen in these figures that mechanical trip is visually evident. It can also be seen in the plasma blade wake measurements for most forcing frequencies that actuation increased the peak of the wake over that of an average blade. It can be seen in the 10 Hz case that the drag was increased significantly. The 50 Hz forcing frequency begins to show a decrease in velocity on the suction side of the blade wake. This would coincide with the actuator being located on the suction surface and acting to remove momentum from the flow.

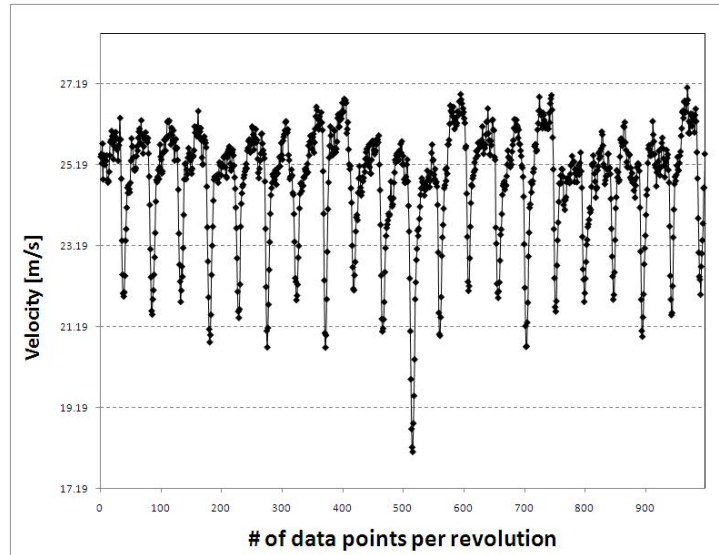


(a) Wake velocity per revolution

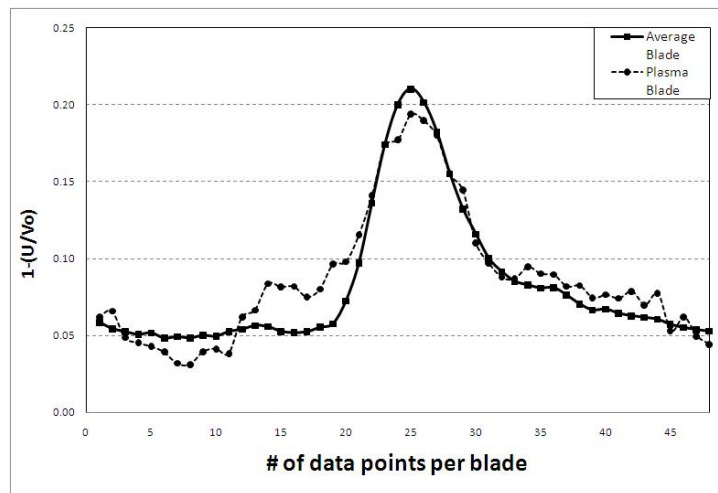


(b) Wake velocity for plasma blade

Figure 3.18: Wake velocity for 600 RPM per revolution (a), and per blade (b): 1/4 Chord Counter Flow Plasma Steady

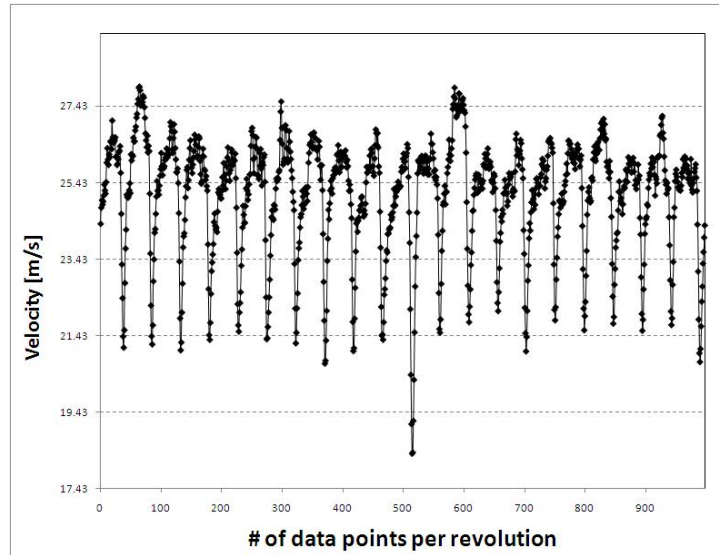


(a) Wake velocity per revolution

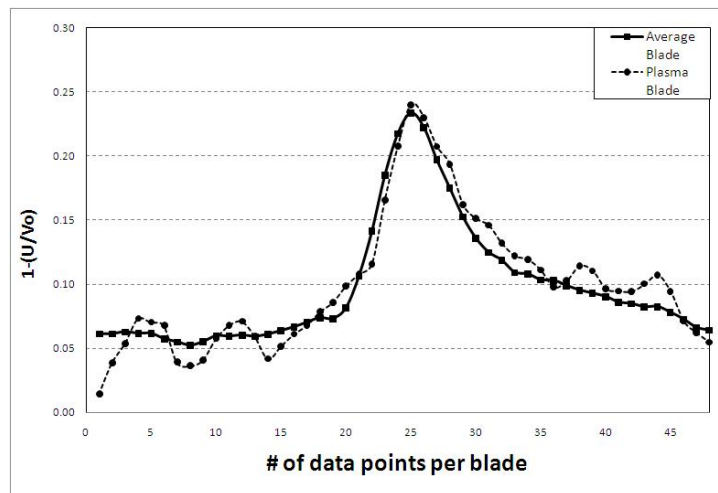


(b) Wake velocity for plasma blade

Figure 3.19: Wake velocity for 600 RPM per revolution (a), and per blade (b): 1/4 Chord Counter Flow Plasma at $F = 10\text{Hz}$

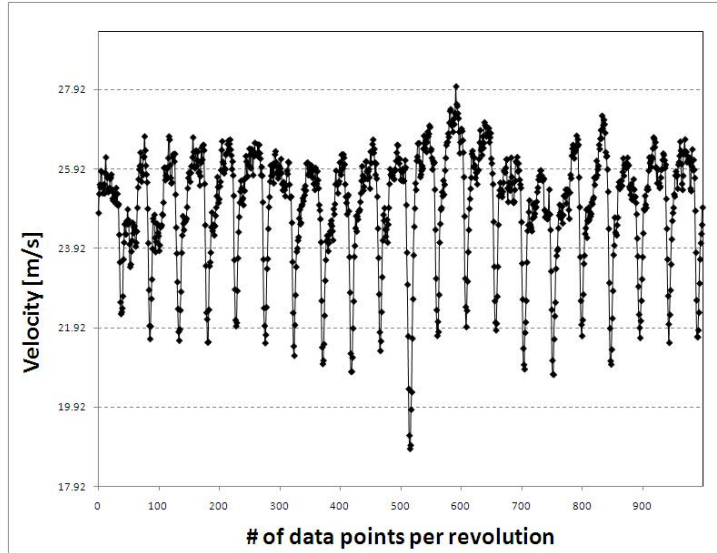


(a) Wake velocity per revolution

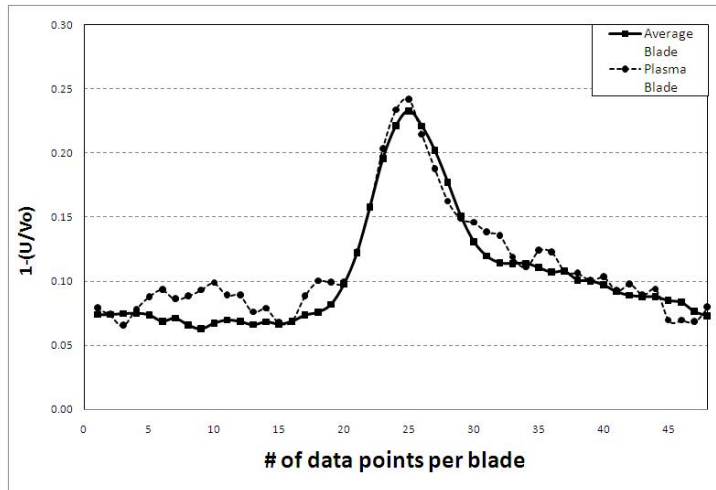


(b) Wake velocity for plasma blade

Figure 3.20: Wake velocity for 600 RPM per revolution (a), and per blade (b): 1/4 Chord Counter Flow Plasma at $F = 30\text{Hz}$

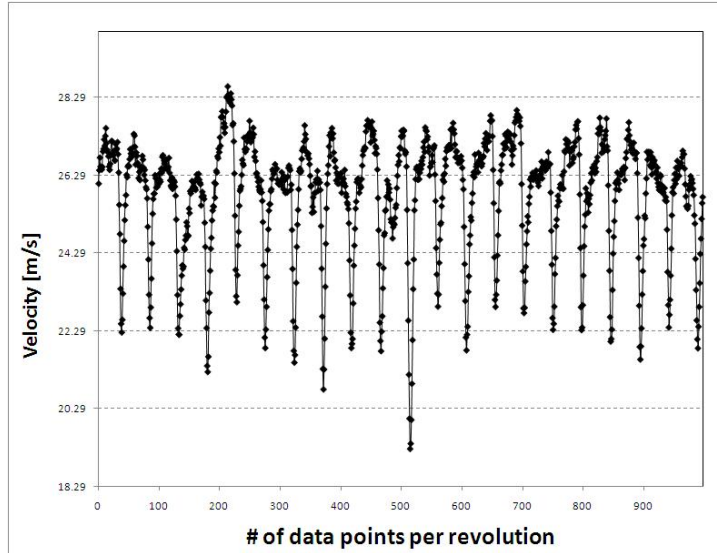


(a) Wake velocity per revolution

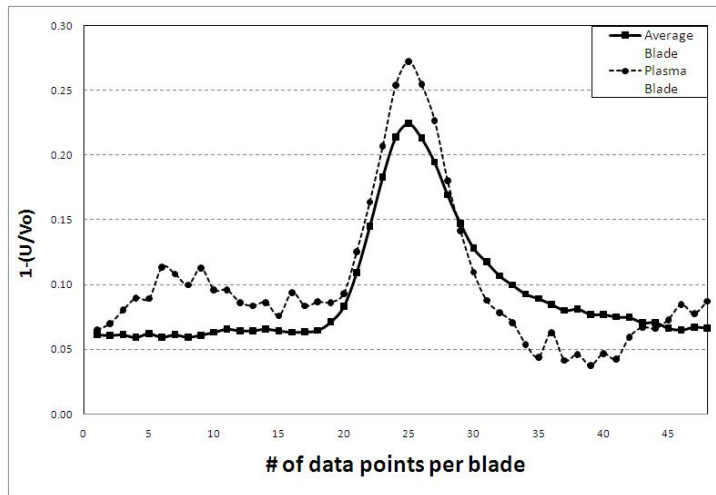


(b) Wake velocity for plasma blade

Figure 3.21: Wake velocity for 600 RPM per revolution (a), and per blade (b): 1/4 Chord Counter Flow Plasma at $F = 50\text{Hz}$

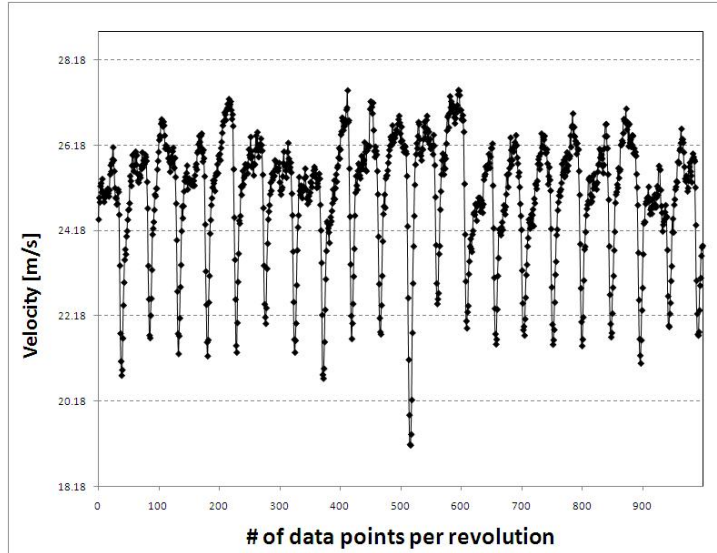


(a) Wake velocity per revolution

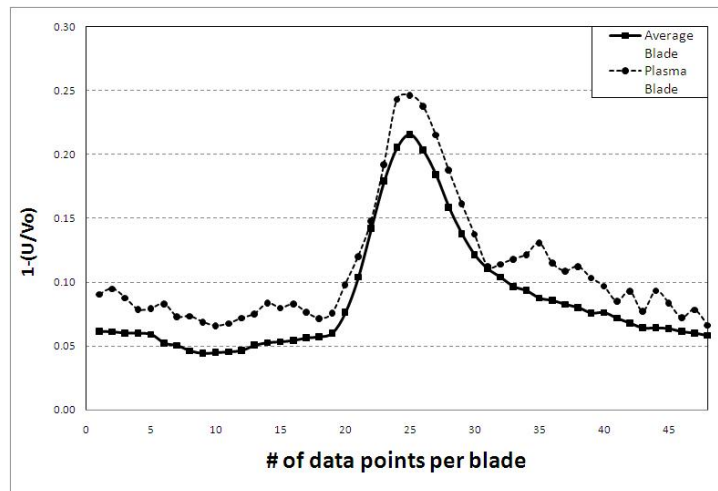


(b) Wake velocity for plasma blade

Figure 3.22: Wake velocity for 600 RPM per revolution (a), and per blade (b): 1/4 Chord Co-Flow Plasma Off

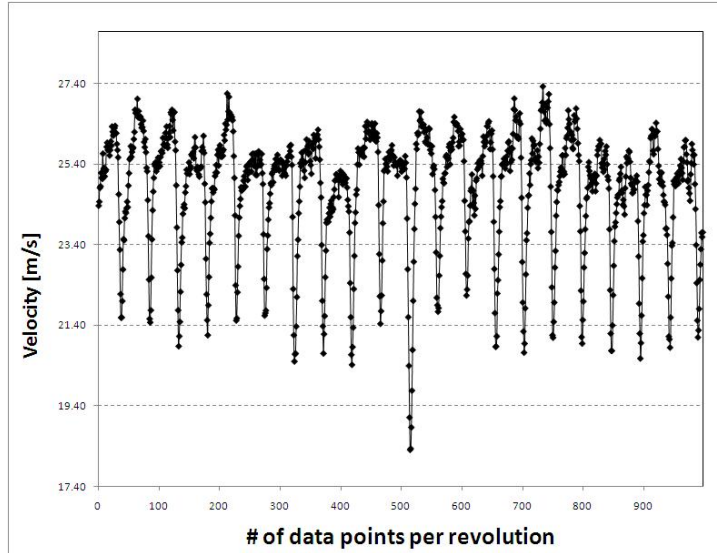


(a) Wake velocity per revolution

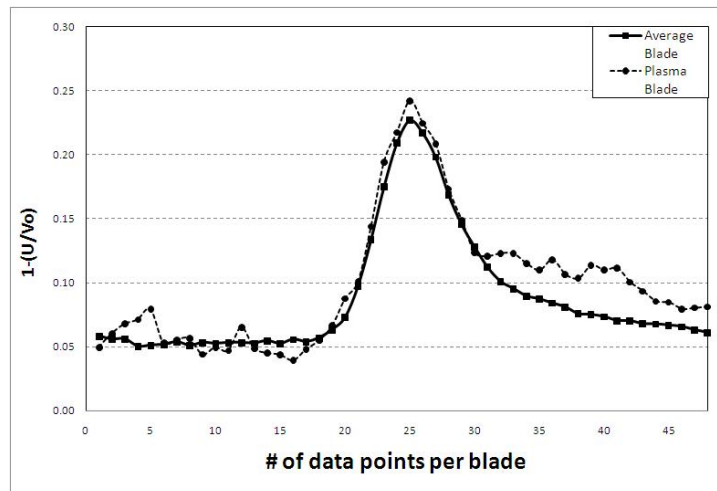


(b) Wake velocity for plasma blade

Figure 3.23: Wake velocity for 600 RPM per revolution (a), and per blade (b): 1/4 Chord Co-Flow Plasma Steady

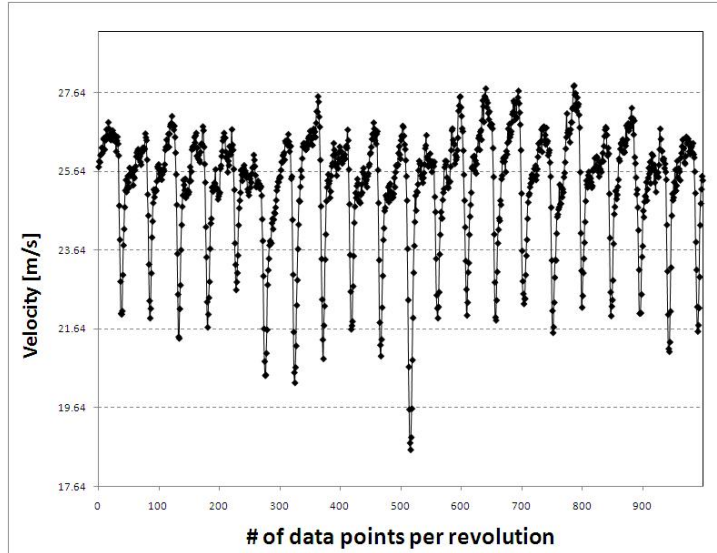


(a) Wake velocity per revolution

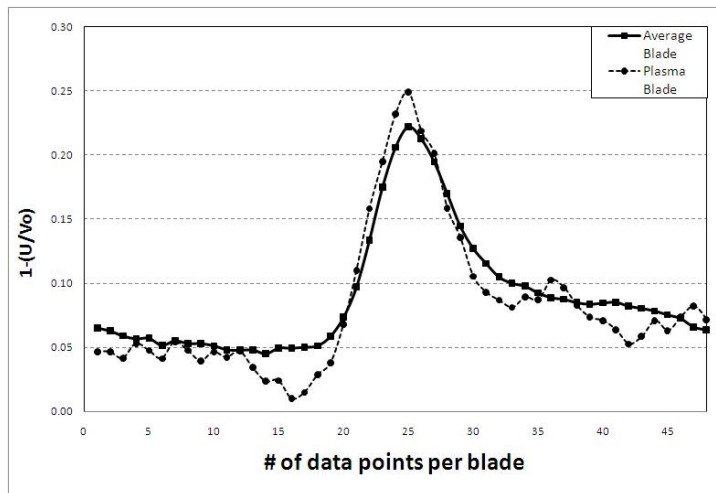


(b) Wake velocity for plasma blade

Figure 3.24: Wake velocity for 600 RPM per revolution (a), and per blade (b): 1/4 Chord Co-Flow Plasma at $F = 10\text{Hz}$

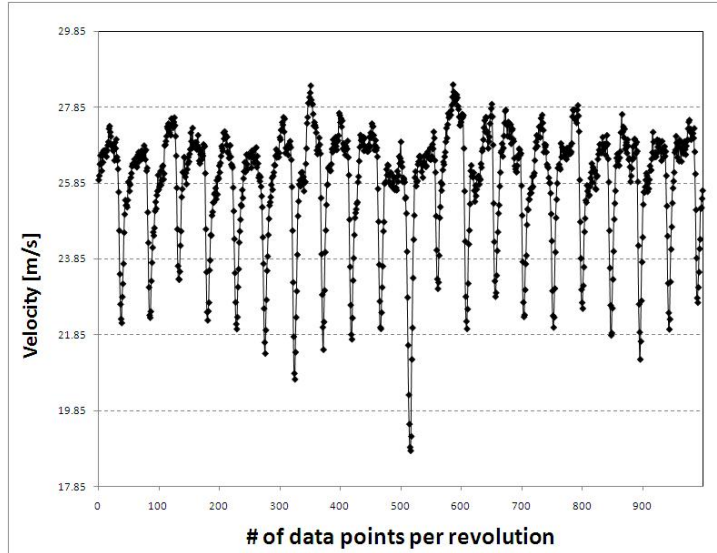


(a) Wake velocity per revolution

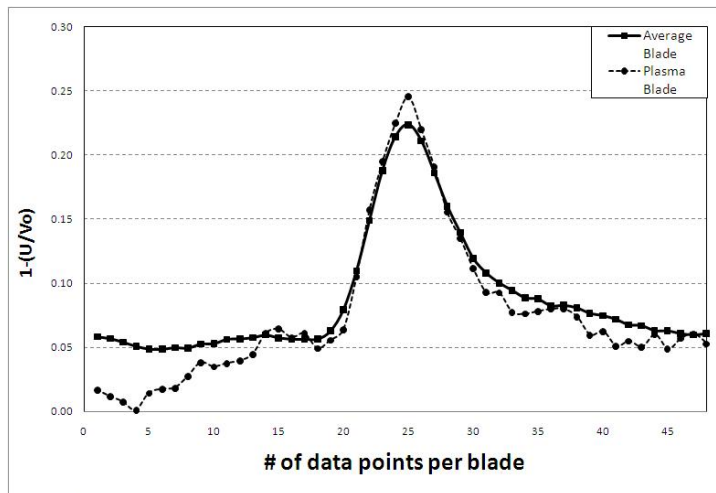


(b) Wake velocity for plasma blade

Figure 3.25: Wake velocity for 600 RPM per revolution (a), and per blade (b): 1/4 Chord Co-Flow Plasma at $F = 30\text{Hz}$



(a) Wake velocity per revolution



(b) Wake velocity for plasma blade

Figure 3.26: Wake velocity for 600 RPM per revolution (a), and per blade (b): 1/4 Chord Co-Flow Plasma at $F = 50\text{Hz}$

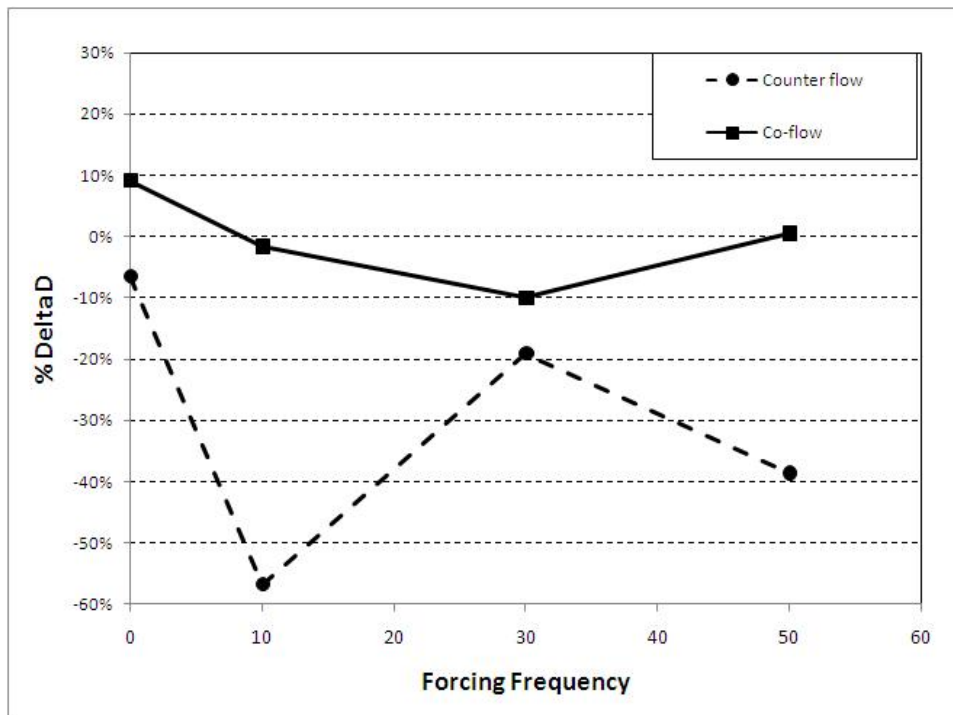
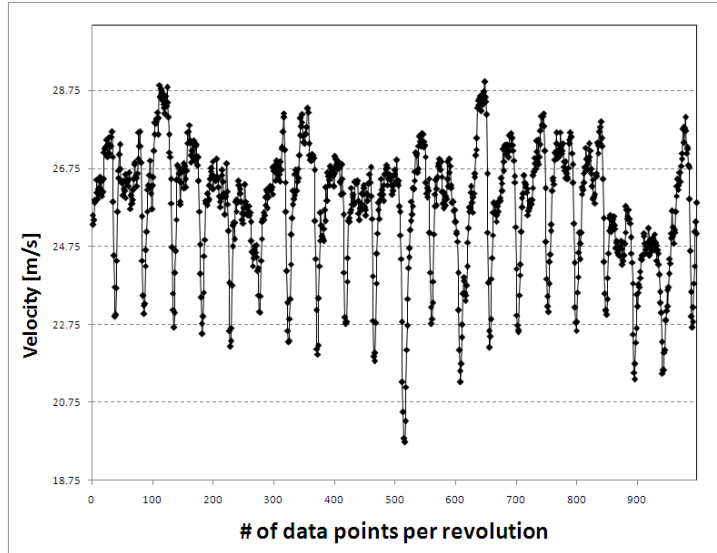
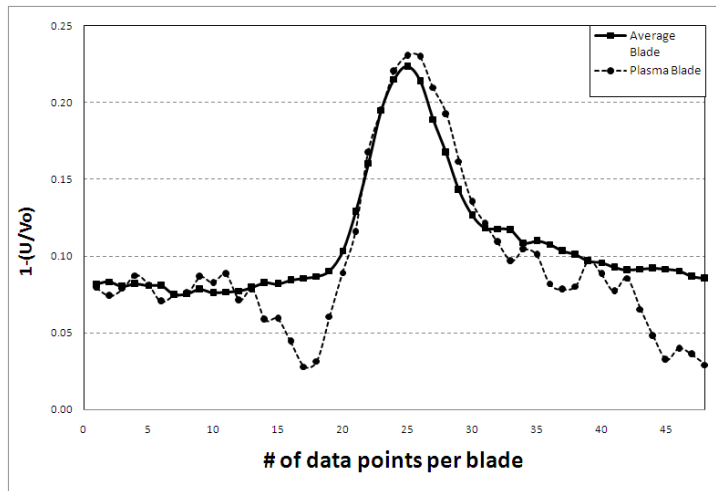


Figure 3.27: Drag variations at various forcing frequencies for 600 RPM with Plasma at leading edge

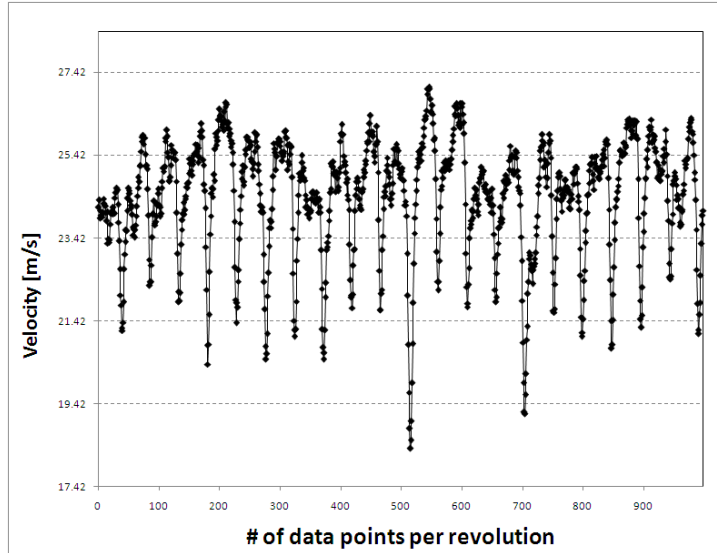


(a) Wake velocity per revolution

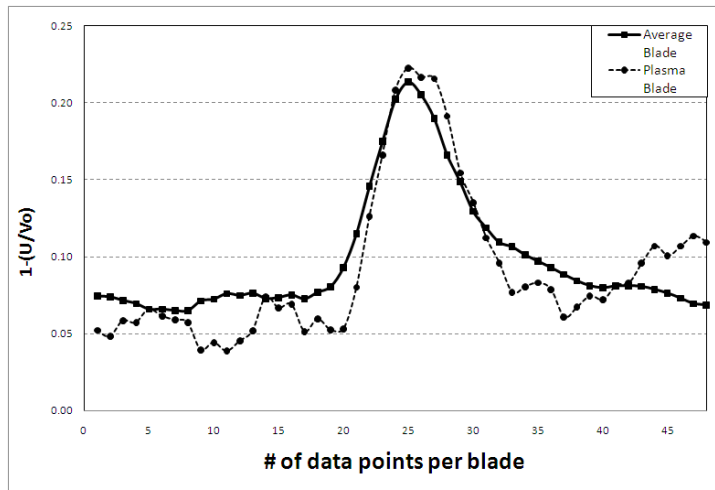


(b) Wake velocity for plasma blade

Figure 3.28: Wake velocity for 600 RPM per revolution (a), and per blade (b): Leading edge Counter Flow Plasma Off

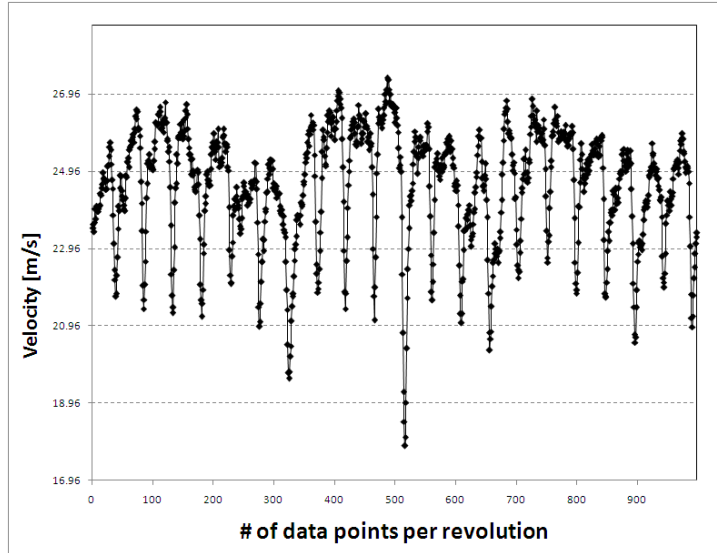


(a) Wake velocity per revolution

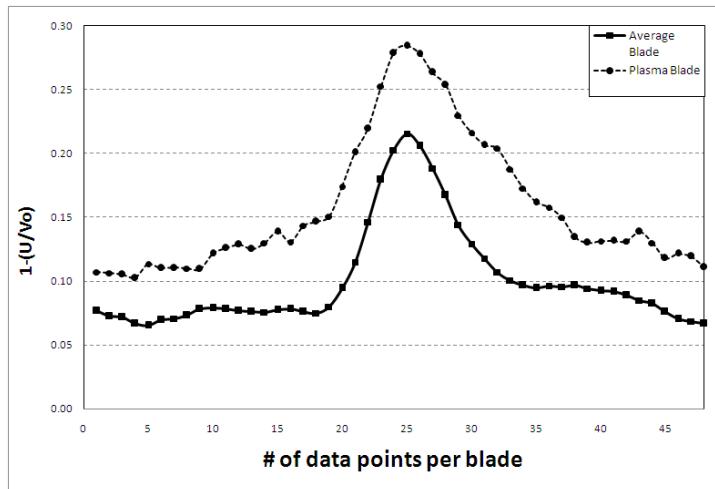


(b) Wake velocity for plasma blade

Figure 3.29: Wake velocity for 600 RPM per revolution (a), and per blade (b): Leading edge Counter Flow Plasma Steady



(a) Wake velocity per revolution

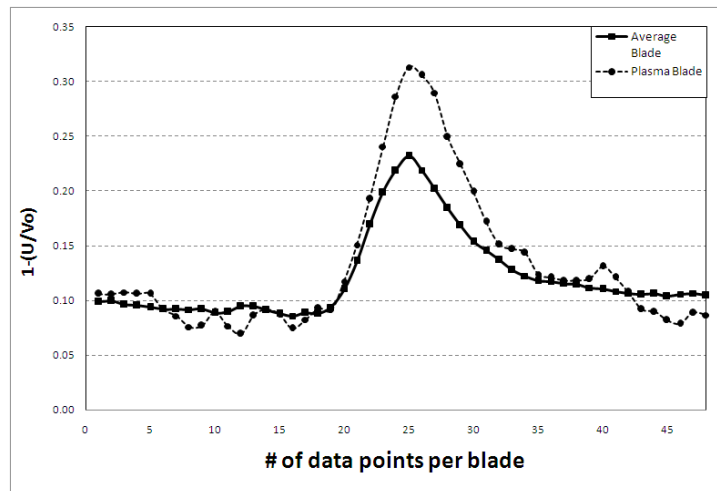


(b) Wake velocity for plasma blade

Figure 3.30: Wake velocity for 600 RPM per revolution (a), and per blade (b): Leading edge Counter Flow Plasma at $F = 10\text{Hz}$

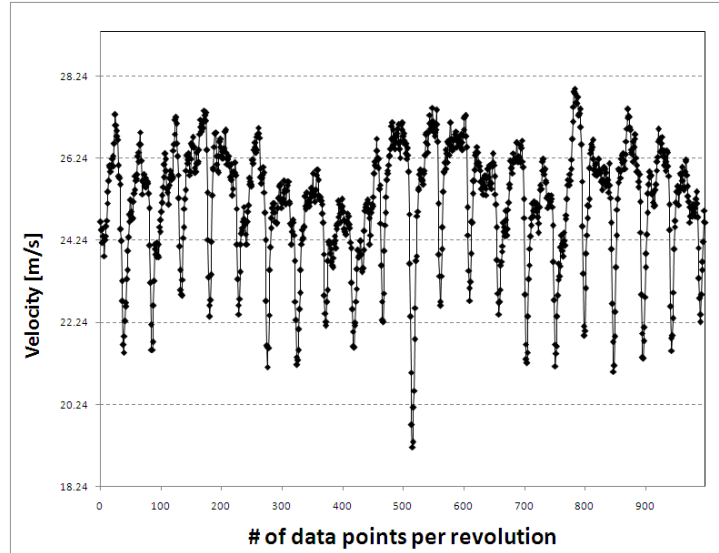


(a) Wake velocity per revolution

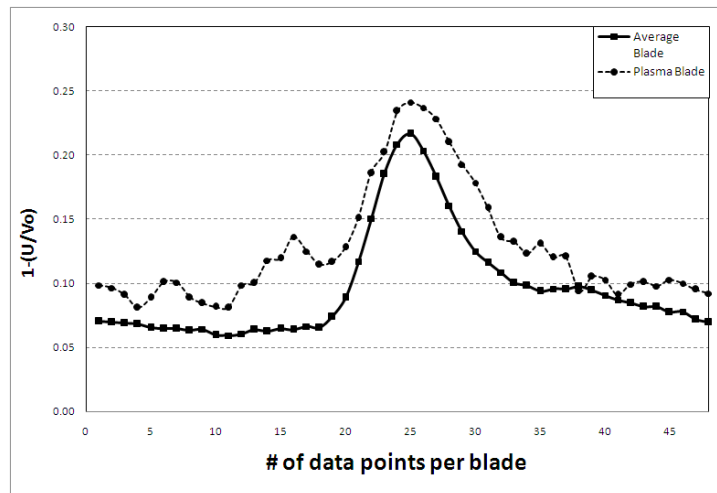


(b) Wake velocity for plasma blade

Figure 3.31: Wake velocity for 600 RPM per revolution (a), and per blade (b): Leading edge Counter Flow Plasma at $F = 30\text{Hz}$



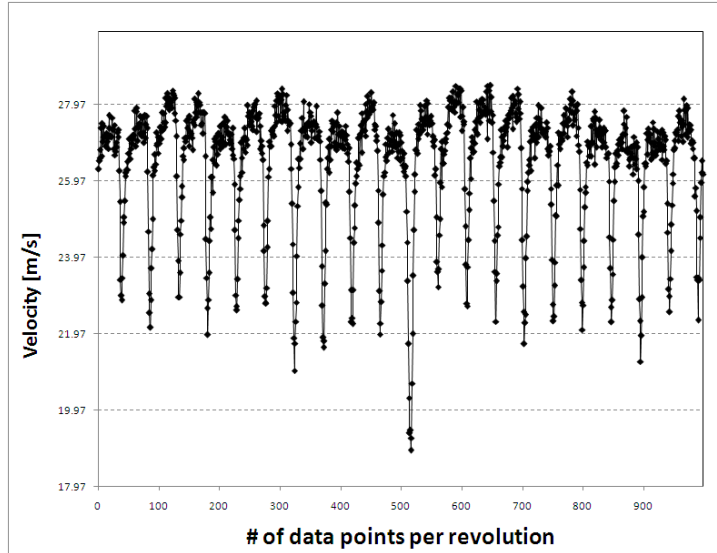
(a) Wake velocity per revolution



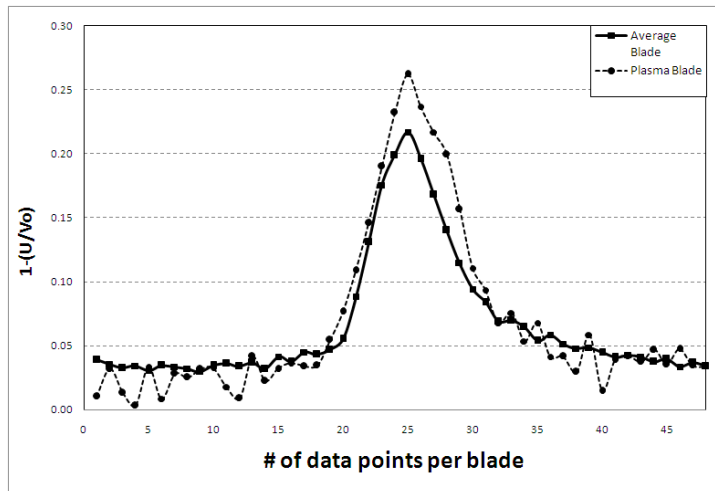
(b) Wake velocity for plasma blade

Figure 3.32: Wake velocity for 600 RPM per revolution (a), and per blade (b): Leading edge Counter Flow Plasma at $F = 50\text{Hz}$

The individual graphical results for the co-flow orientation can be seen in figure 3.33(a) through 3.37(b) for both the entire rotor revolution and for the plasma blade itself for the leading edge cases run at 600 RPM. In this group of figures the plasma blade wake is located in the seventh blade position and the mechanical trip remained installed on the eleventh blade position. It can be seen in these figures that mechanical trip is visually evident. It can also be seen in the plasma blade wake measurements for most forcing frequencies that actuation increased the peak of the wake over that of an average blade.

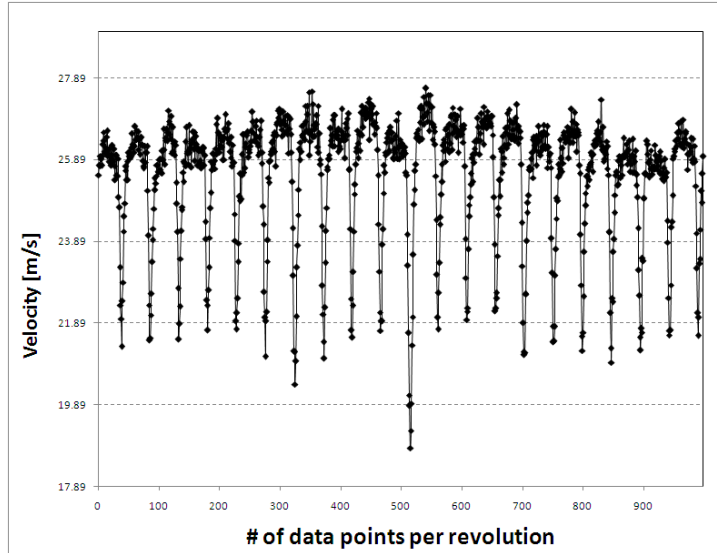


(a) Wake velocity per revolution

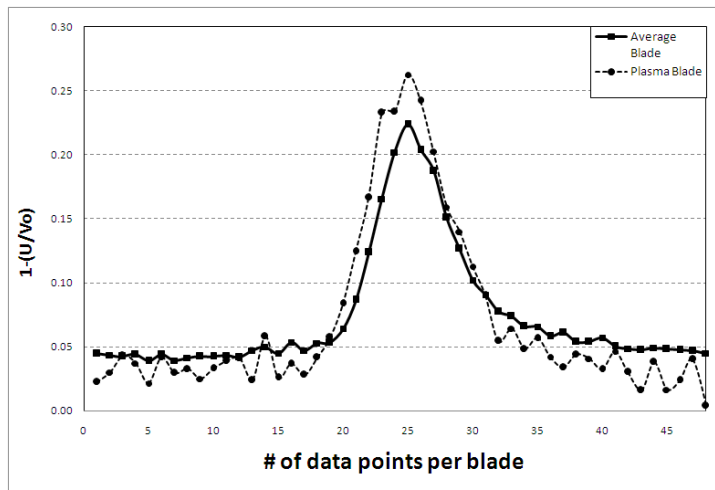


(b) Wake velocity for plasma blade

Figure 3.33: Wake velocity for 600 RPM per revolution (a), and per blade (b): Leading edge Co-Flow Plasma Off

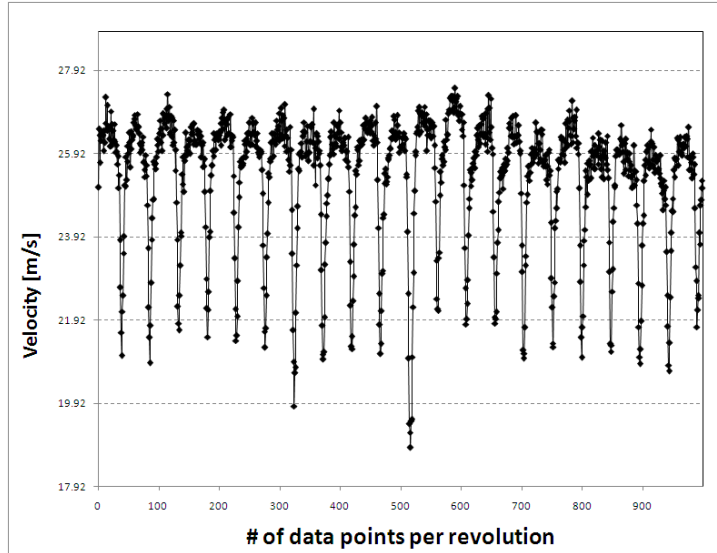


(a) Wake velocity per revolution

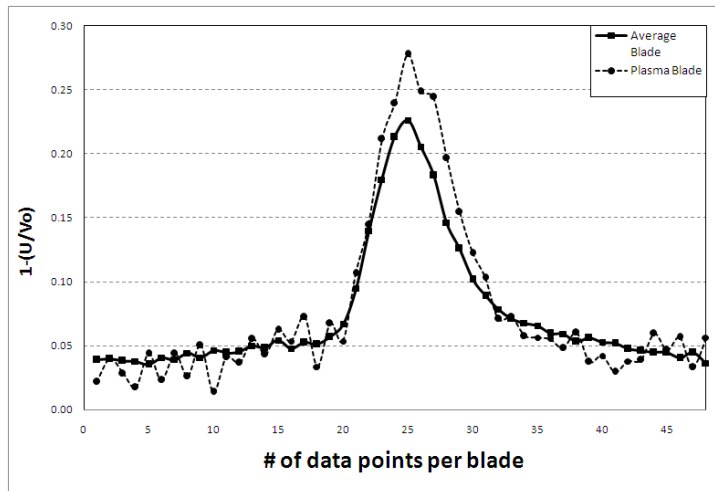


(b) Wake velocity for plasma blade

Figure 3.34: Wake velocity for 600 RPM per revolution (a), and per blade (b): Leading edge Co-Flow Plasma Steady

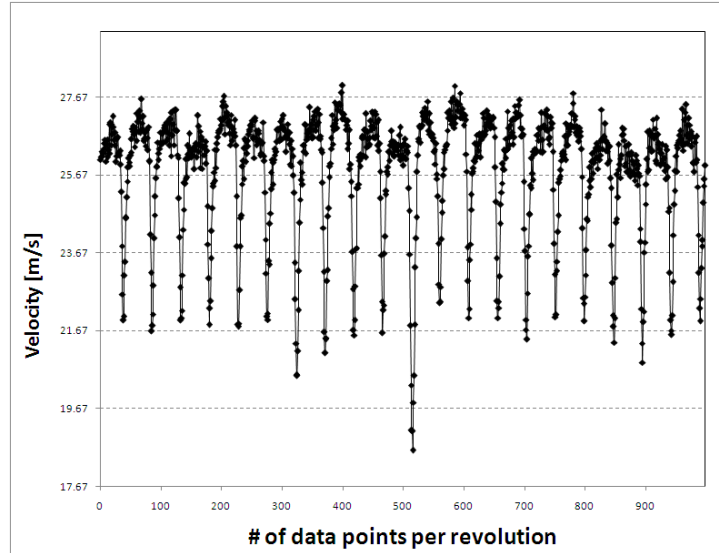


(a) Wake velocity per revolution

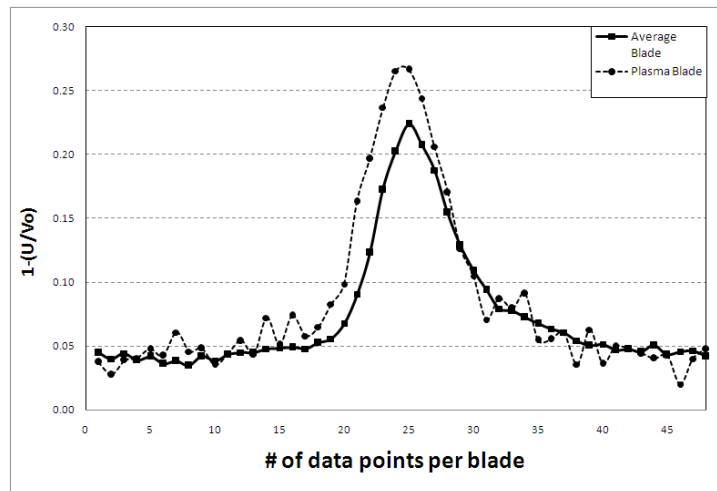


(b) Wake velocity for plasma blade

Figure 3.35: Wake velocity for 600 RPM per revolution (a), and per blade (b): Leading edge Co-Flow Plasma at $F = 10\text{Hz}$

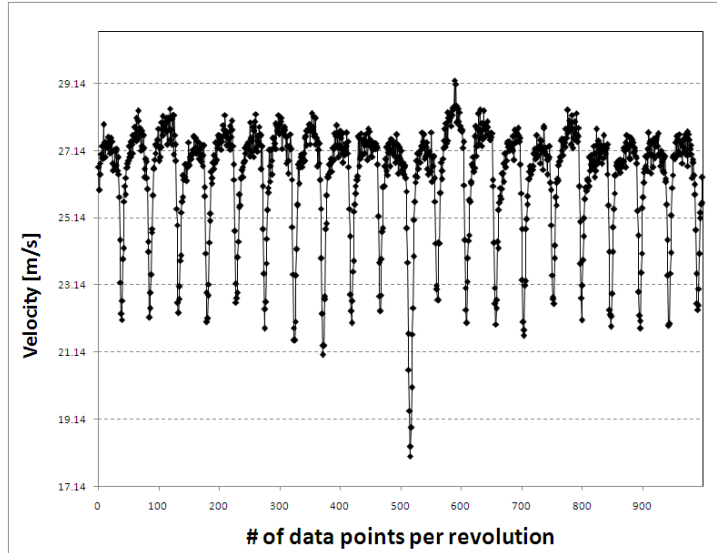


(a) Wake velocity per revolution

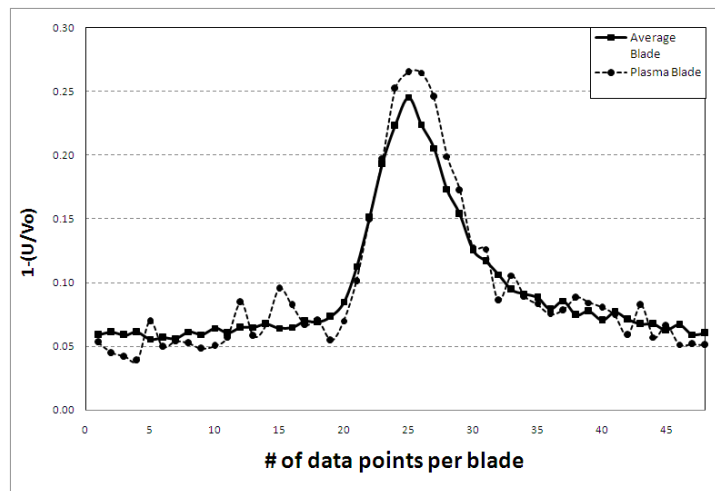


(b) Wake velocity for plasma blade

Figure 3.36: Wake velocity for 600 RPM per revolution (a), and per blade (b): Leading edge Co-Flow Plasma at $F = 30\text{Hz}$



(a) Wake velocity per revolution



(b) Wake velocity for plasma blade

Figure 3.37: Wake velocity for 600 RPM per revolution (a), and per blade (b): Leading edge Co-Flow Plasma at $F = 50\text{Hz}$

3.2.2 Counter and Co-Flow Results for 350 RPM at Various Forcing Frequencies

The second set of results were achieved with the rotor RPM set to 350, which equated to a Reynolds number of about 1.7×10^4 . The data was sampled at 10 kHz and analyzed using the window averaging computer program. The forcing frequency was varied using forcing frequencies of 10 Hz, 30 Hz, and 50 Hz. Data was also sampled with the actuator off and in steady actuation. The hotwire was located at the midspan location, one chord length downstream. Results were taken with the actuator at 1/4 chord and at the leading edge locations.

350 RPM 1/4 chord results

A summary of the drag data for both flow orientations can be seen in figure 3.38 for the 1/4 chord actuator configuration at 350 RPM. The graph shows the change in percent delta D for various forcing frequencies. The data reveals that the counter flow orientation may tend to decrease the drag in the wake of the plasma blade with increasing forcing frequency. It also shows that for the co-flow orientation that as the forcing frequency increases so does the increase in drag. It is of note that at a forcing frequency of zero, which signifies steady plasma operation, the percent change in drag for the co-flow case is at its peak. This signifies that there is a drag decrease on the plasma blade during steady plasma actuation of approximately 12%, although as the forcing frequency increases so does the drag.

The individual graphical results for the counter flow orientation can be seen in figures 3.39(a) through 3.43(b) for both the entire rotor revolution and for the plasma blade itself for the 1/4 chord cases run at 350 RPM. In this group of figures the plasma blade wake is located in the eighth blade position and the mechanical trip

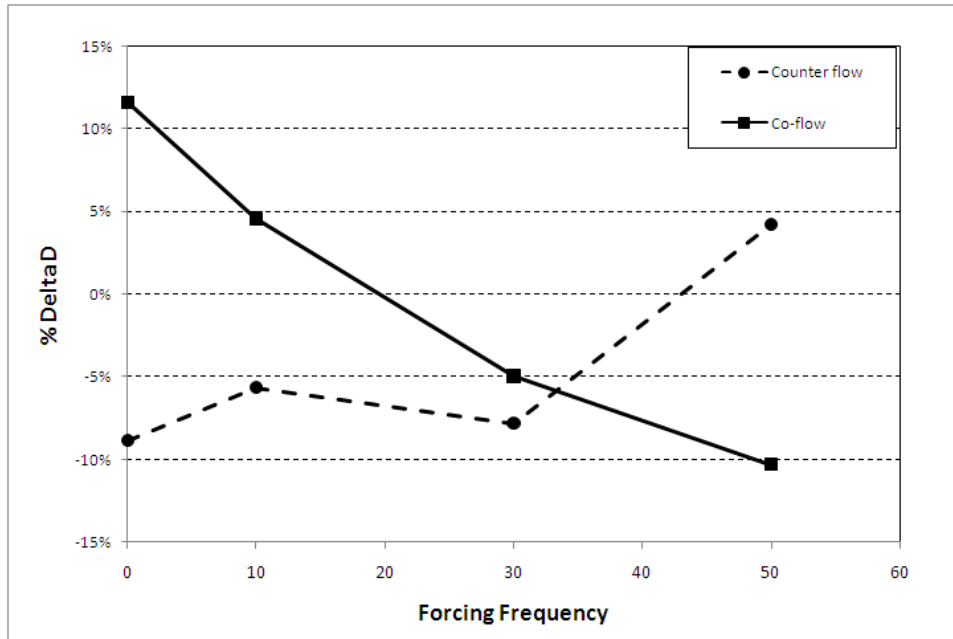
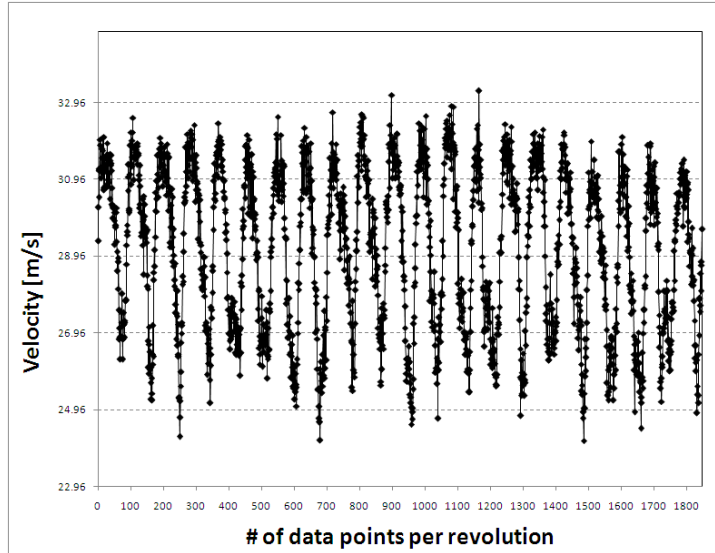
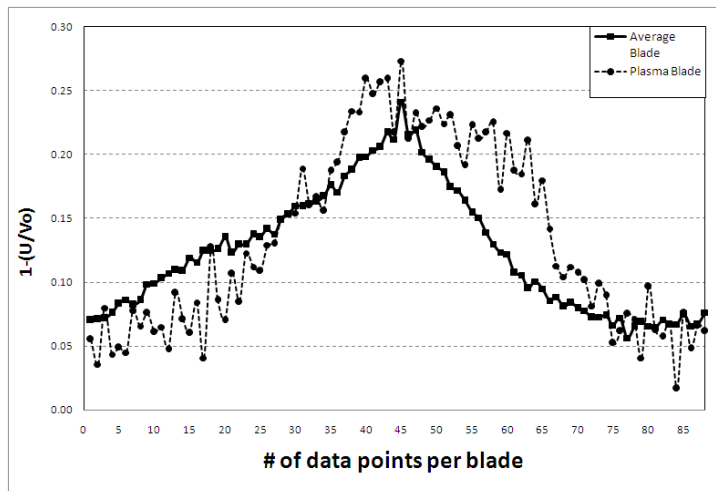


Figure 3.38: Drag variations at various forcing frequencies for 350 RPM with Plasma at 1/4 Chord

remained installed on the eleventh blade position. It can be seen in these figures that mechanical trip is not always visually evident. It can also be seen in the plasma blade wake measurements for the zero forcing frequency that there is a velocity decrease evident on the suction side of the blade wake. Then as the blade passes there is a steeper velocity gradient as compared to the average blade as the wake velocity returns to the free stream velocity magnitude. Thus making this forcing frequency the optimum for decreasing drag for this actuator and flow configuration. This could be the actuator's effect on the airflow by encouraging reattachment of the airflow, and thus increasing the velocity.

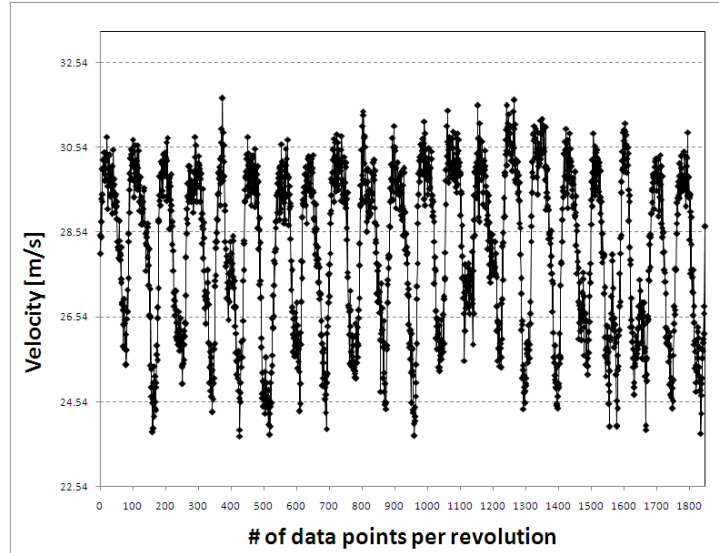


(a) Wake velocity per revolution

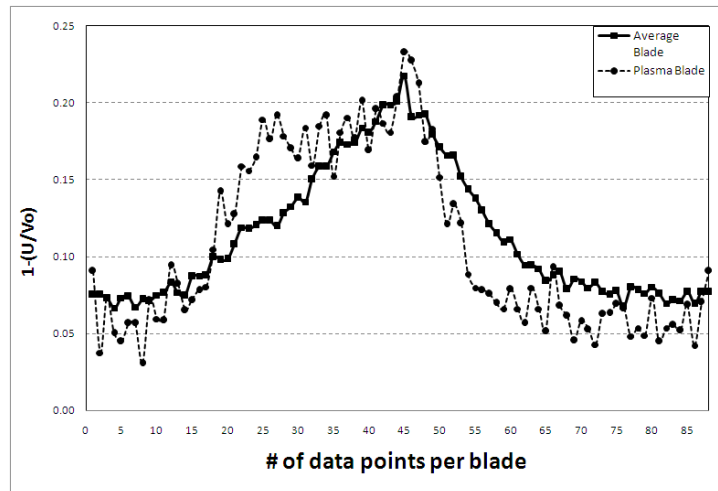


(b) Wake velocity for plasma blade

Figure 3.39: Wake velocity for 350 RPM per revolution (a), and per blade (b): 1/4 Chord Counter Flow Plasma Off

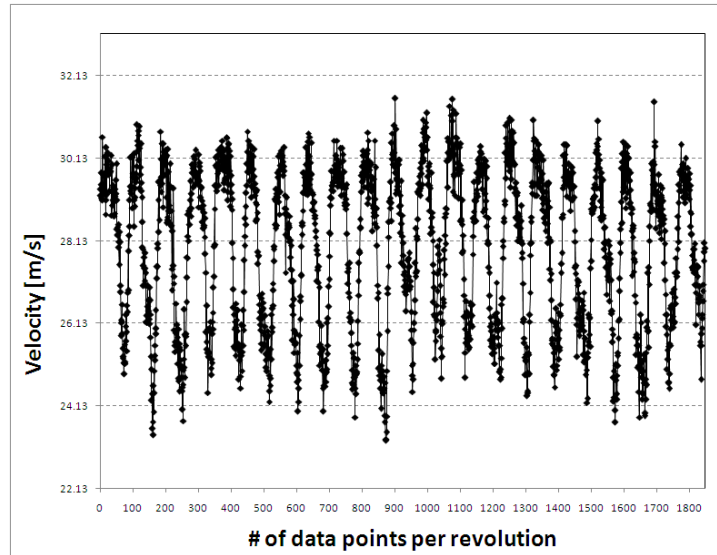


(a) Wake velocity per revolution

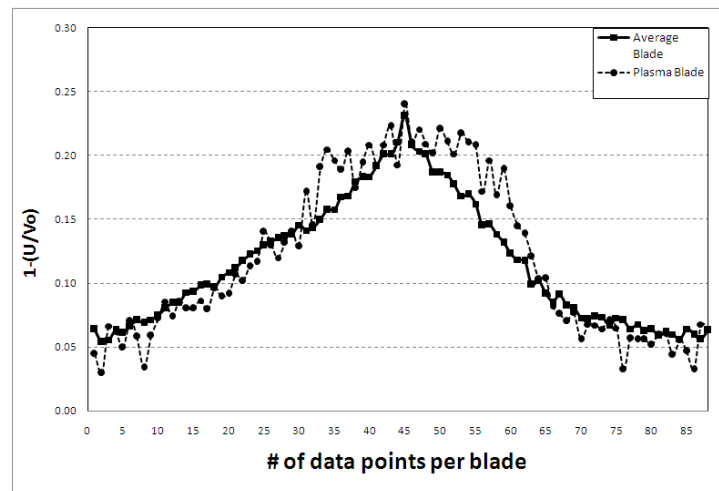


(b) Wake velocity for plasma blade

Figure 3.40: Wake velocity for 350 RPM per revolution (a), and per blade (b): 1/4 Chord Counter Flow Plasma Steady

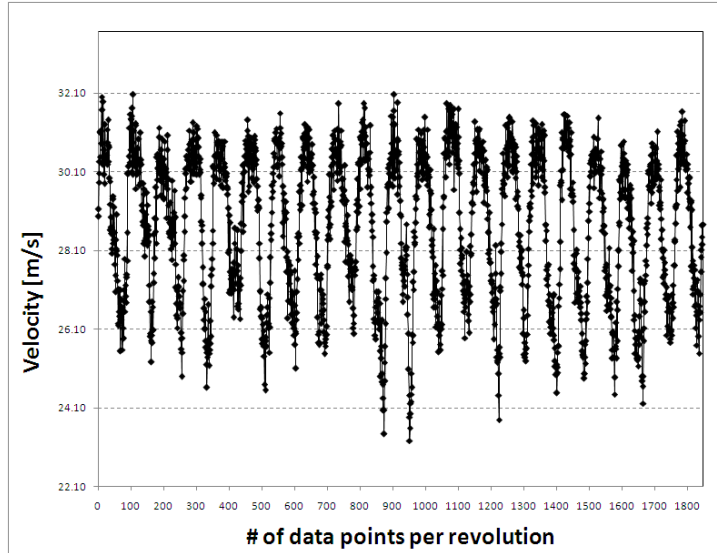


(a) Wake velocity per revolution

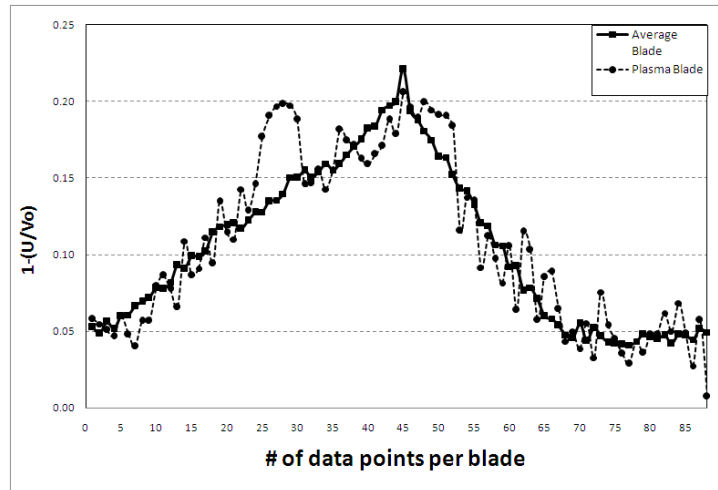


(b) Wake velocity for plasma blade

Figure 3.41: Wake velocity for 350 RPM per revolution (a), and per blade (b): 1/4 Chord Counter Flow Plasma at $F = 10\text{Hz}$

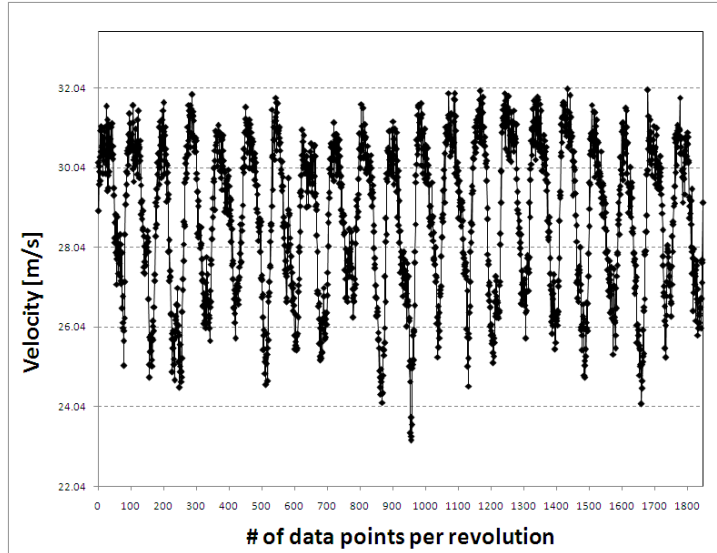


(a) Wake velocity per revolution

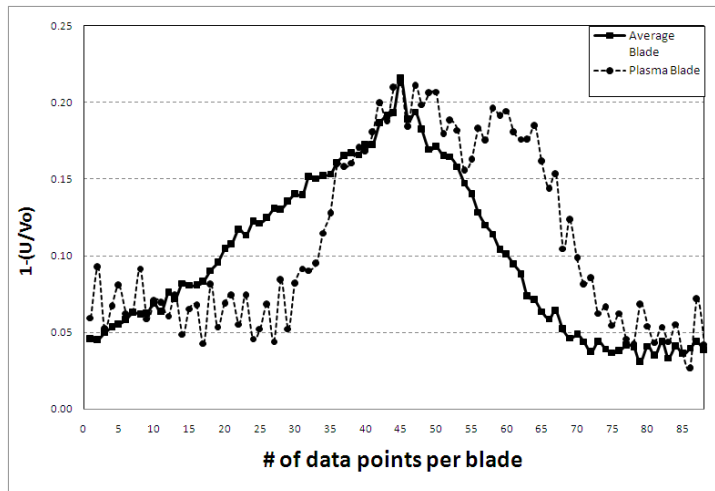


(b) Wake velocity for plasma blade

Figure 3.42: Wake velocity for 350 RPM per revolution (a), and per blade (b): 1/4 Chord Counter Flow Plasma at $F = 30\text{Hz}$



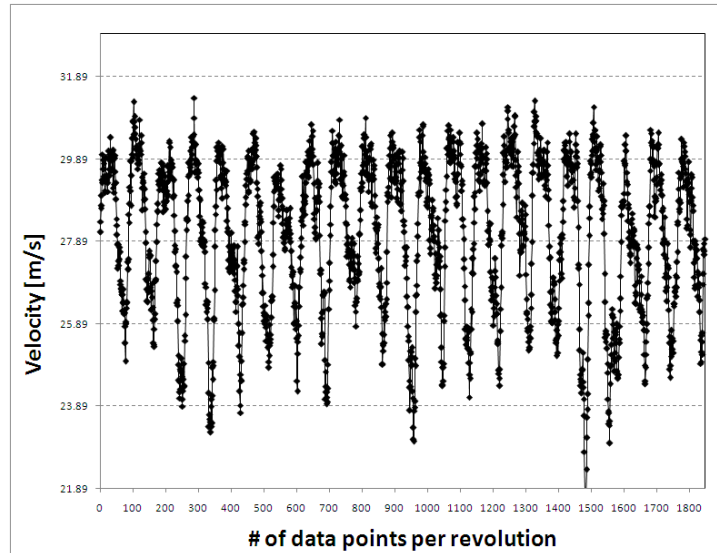
(a) Wake velocity per revolution



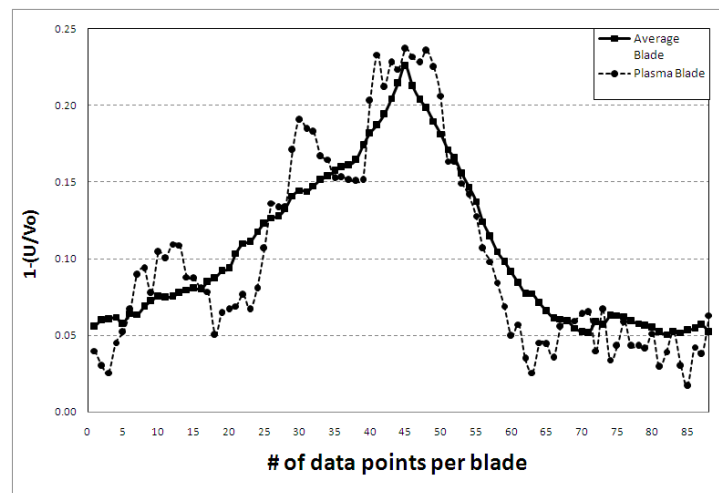
(b) Wake velocity for plasma blade

Figure 3.43: Wake velocity for 350 RPM per revolution (a), and per blade (b): 1/4 Chord Counter Flow Plasma at $F = 50\text{Hz}$

The individual graphical results for the co-flow orientation can be seen in figures 3.44(a) through 3.48(b) for both the entire rotor revolution and for the plasma blade itself for the 1/4 chord cases run at 350 RPM. In this group of figures the plasma blade wake is located in the seventh blade position and the mechanical trip remained installed on the eleventh blade position. It can be seen in these figures that mechanical trip is not always visually evident. It can also be seen in the plasma blade wake measurements that there is a velocity decrease evident on the suction side of the blade wake for 50 Hz case. Then as the blade passes there is a steeper velocity gradient as compared to the average blade as the wake velocity returns to the free stream velocity magnitude. Thus making this forcing frequency the optimum for decreasing drag for this actuator and flow configuration. This could be the actuator's effect on the airflow by encouraging reattachment of the airflow, and thus increasing the velocity.

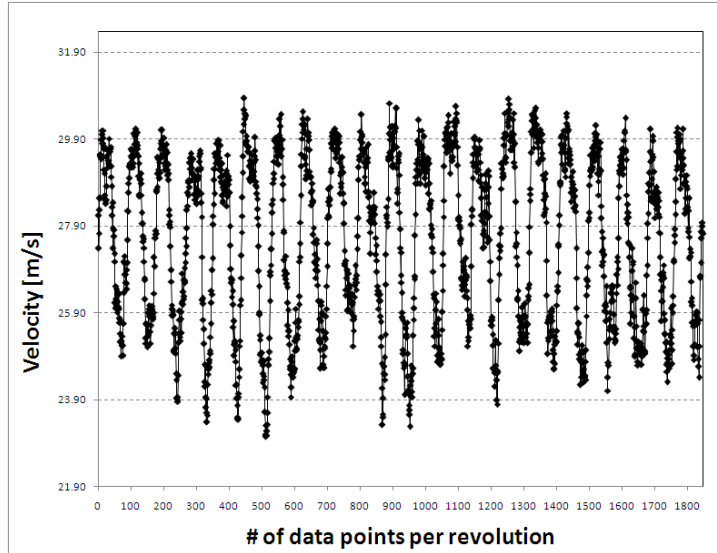


(a) Wake velocity per revolution

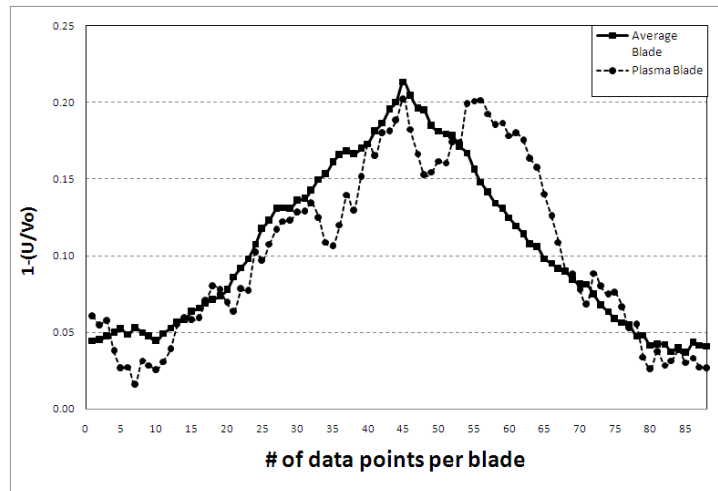


(b) Wake velocity for plasma blade

Figure 3.44: Wake velocity for 350 RPM per revolution (a), and per blade (b): 1/4 Chord Co-Flow Plasma Off

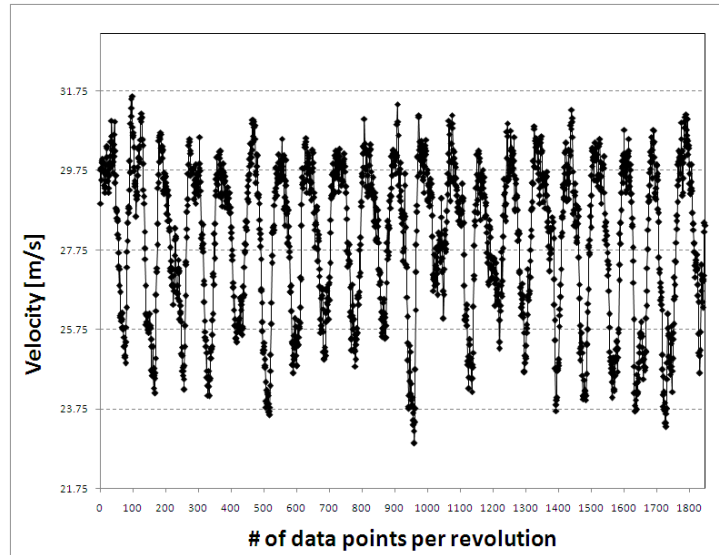


(a) Wake velocity per revolution

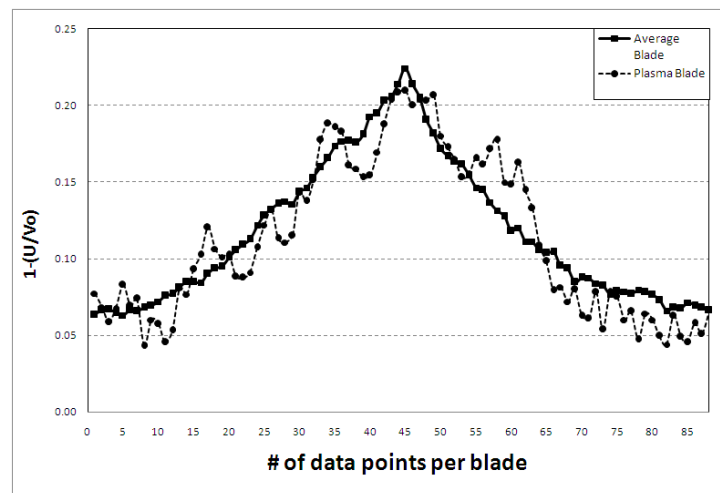


(b) Wake velocity for plasma blade

Figure 3.45: Wake velocity for 350 RPM per revolution (a), and per blade (b): 1/4 Chord Co-Flow Plasma Steady

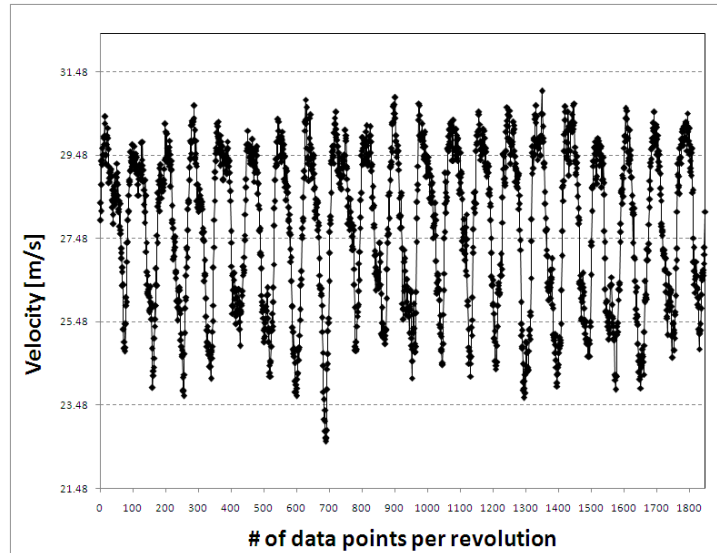


(a) Wake velocity per revolution

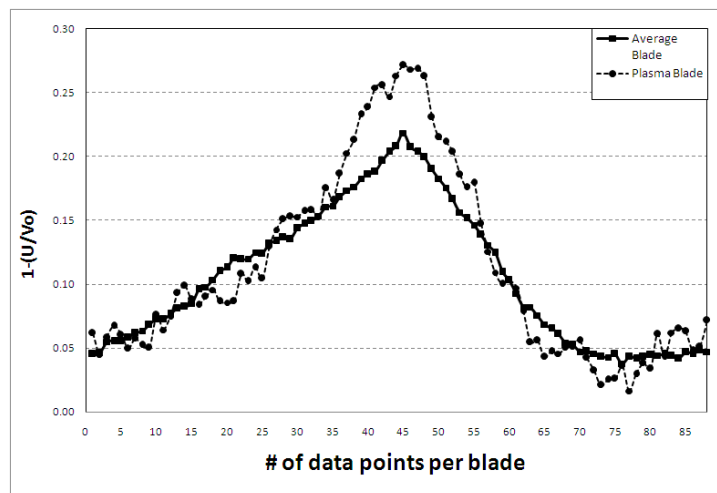


(b) Wake velocity for plasma blade

Figure 3.46: Wake velocity for 350 RPM per revolution (a), and per blade (b): 1/4 Chord Co-Flow Plasma at $F = 10\text{Hz}$

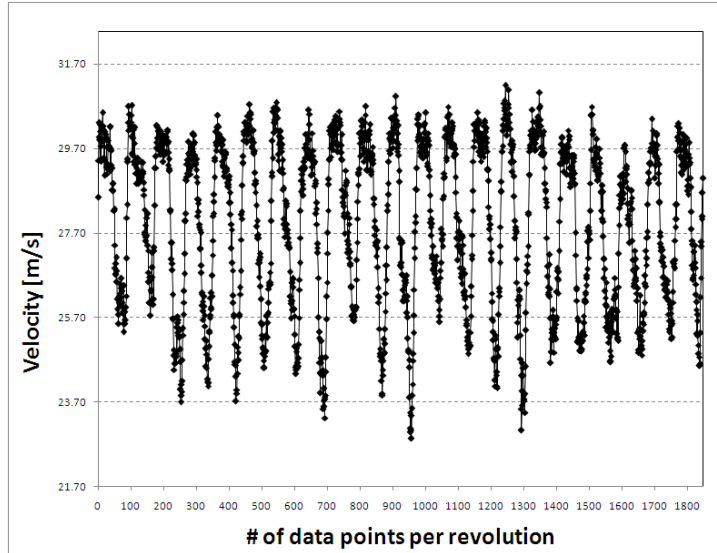


(a) Wake velocity per revolution

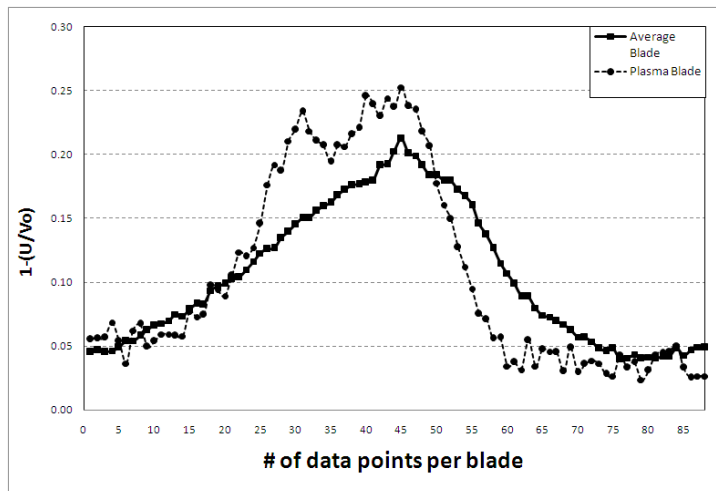


(b) Wake velocity for plasma blade

Figure 3.47: Wake velocity for 350 RPM per revolution (a), and per blade (b): 1/4 Chord Co-Flow Plasma at $F = 30\text{Hz}$



(a) Wake velocity per revolution



(b) Wake velocity for plasma blade

Figure 3.48: Wake velocity for 350 RPM per revolution (a), and per blade (b): 1/4 Chord Co-Flow Plasma at $F = 50\text{Hz}$

350 RPM Leading edge results

A summary of the drag data for both flow orientations can be seen in figure 3.49 for the leading edge actuator configuration at 350 RPM. The graph shows the change in percent delta D for various forcing frequencies. The data reveals that both the counter and co-flow actuators decreased drag in the wake of the plasma blade at a forcing frequency of zero. The co-flow orientation decreased drag by about 10% and the counterflow by about 6% during steady actuation. As the forcing frequency increased the change in drag became sporadic and unpredictable. It is of note that at a forcing frequency of zero Hz, which signifies steady plasma operation, the percent change in drag was at its optimum for both the counter and co-flow orientations. This could indicate that a pulsed leading edge actuator may be too disruptive to the flow at this Reynolds number, and may possibly encourage separation.

The individual graphical results for the counter flow orientation can be see in figure 3.50(a) through 3.54(b) for both the entire rotor revolution and for the plasma blade itself for the leading edge cases run at 350 RPM. In this group of figures the plasma blade wake is located in the eighth blade position and the mechanical trip remained installed on the eleventh blade position. It can be seen in these figures that mechanical trip not always visually evident. It can also be seen in the plasma blade wake measurements at a forcing frequency of zero, which is steady plasma actuation, that the blade wake is much improved over that of the plasma blade in the off condition.

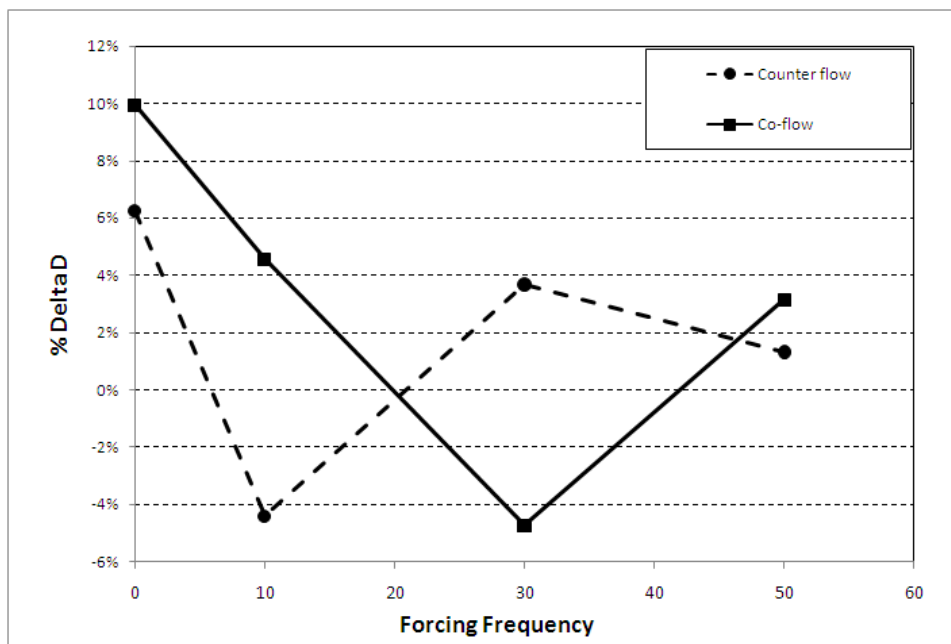
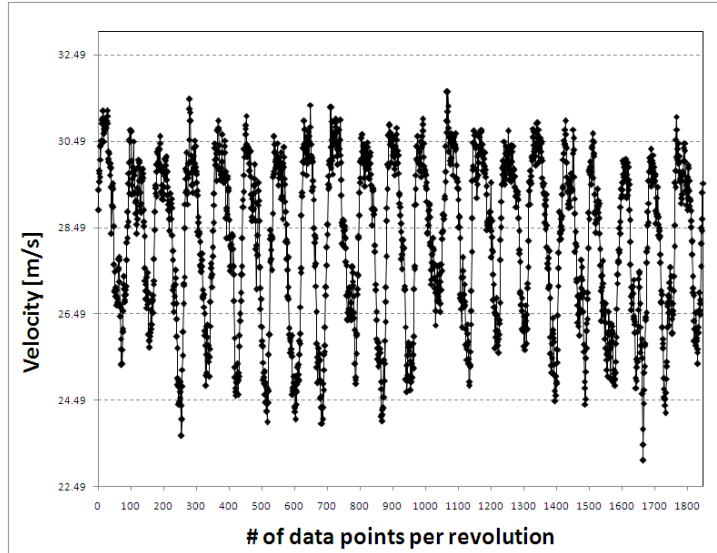
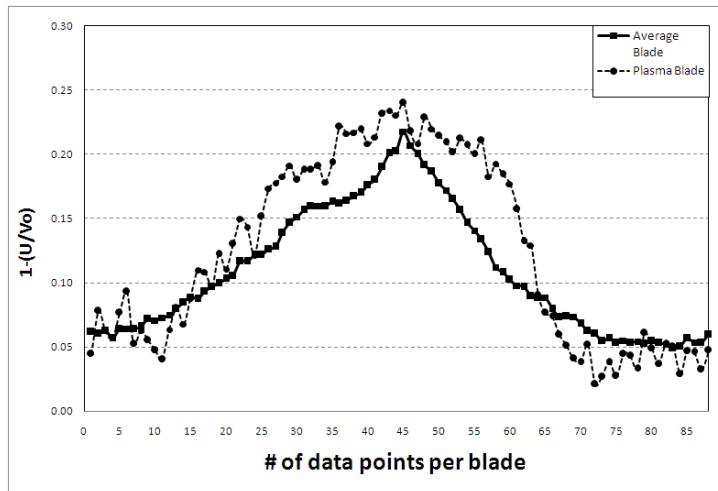


Figure 3.49: Drag variations at various forcing frequencies for 350 RPM with Plasma at leading edge

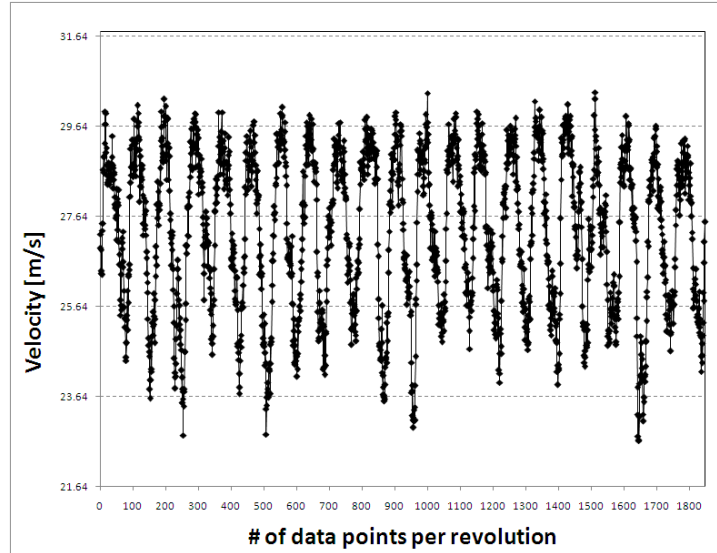


(a) Wake velocity per revolution

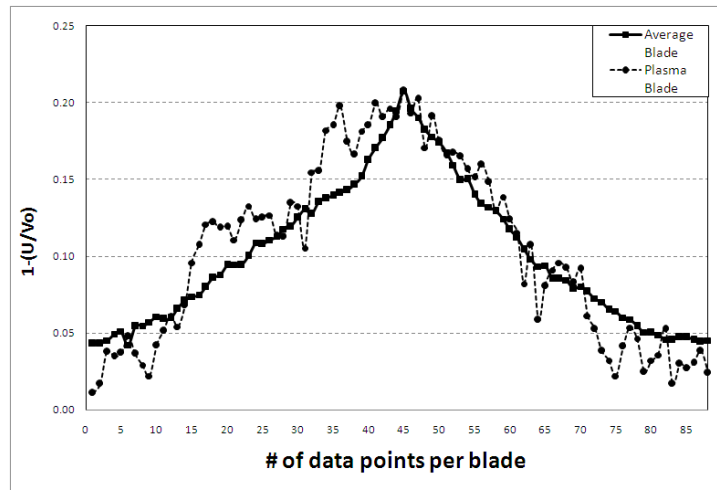


(b) Wake velocity for plasma blade

Figure 3.50: Wake velocity for 350 RPM per revolution (a), and per blade (b): Leading edge Counter Flow Plasma Off

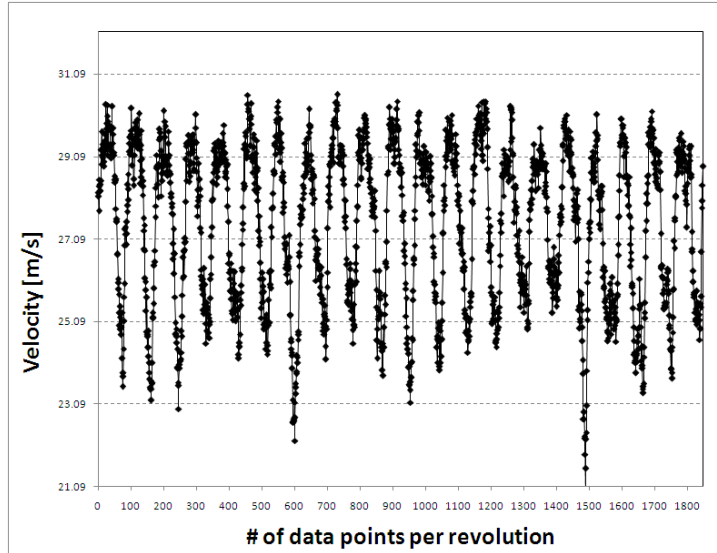


(a) Wake velocity per revolution

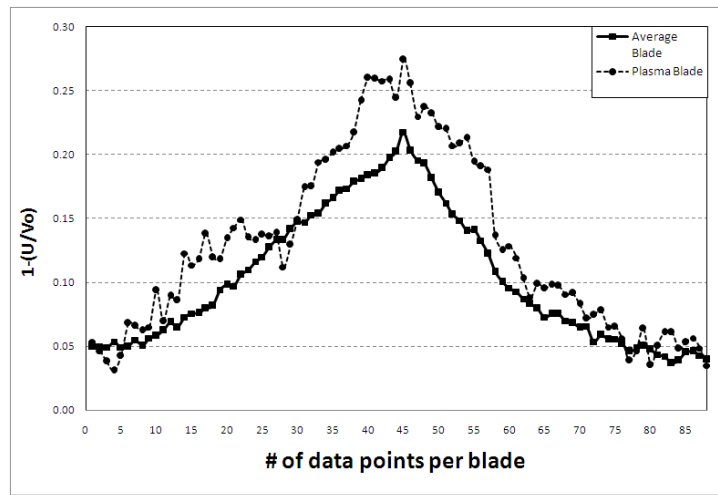


(b) Wake velocity for plasma blade

Figure 3.51: Wake velocity for 350 RPM per revolution (a), and per blade (b): Leading edge Counter Flow Plasma Steady

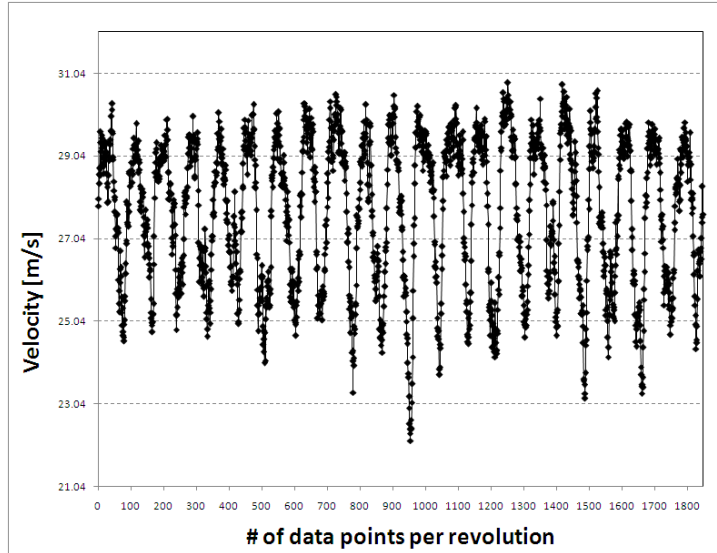


(a) Wake velocity per revolution

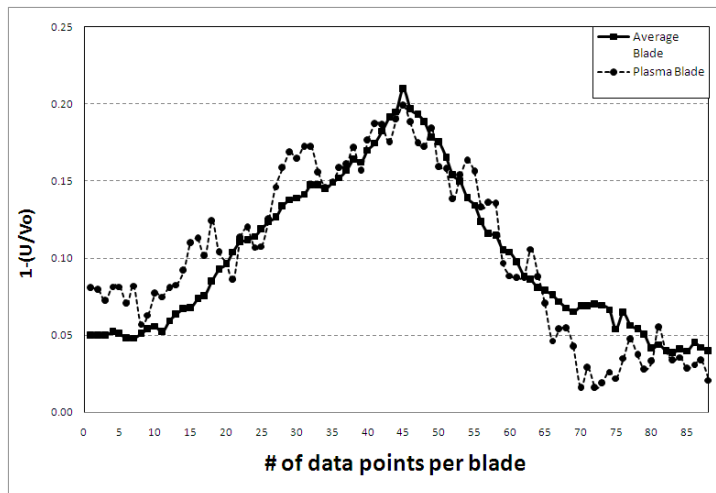


(b) Wake velocity for plasma blade

Figure 3.52: Wake velocity for 350 RPM per revolution (a), and per blade (b): Leading edge Counter Flow Plasma at $F = 10\text{Hz}$

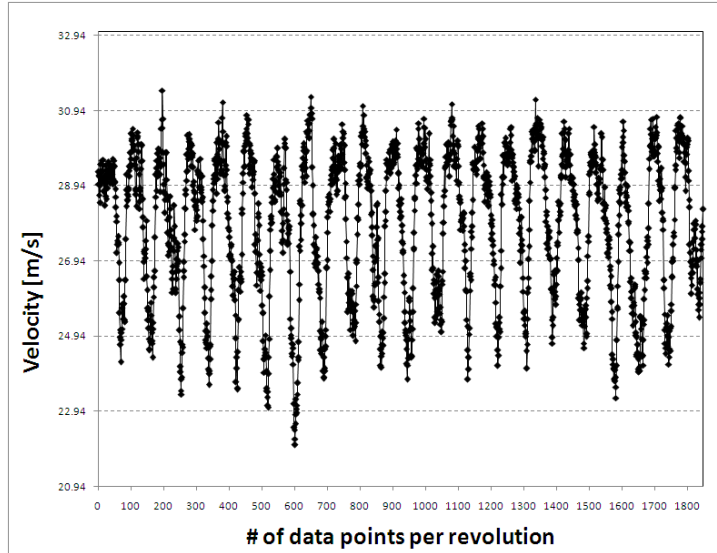


(a) Wake velocity per revolution

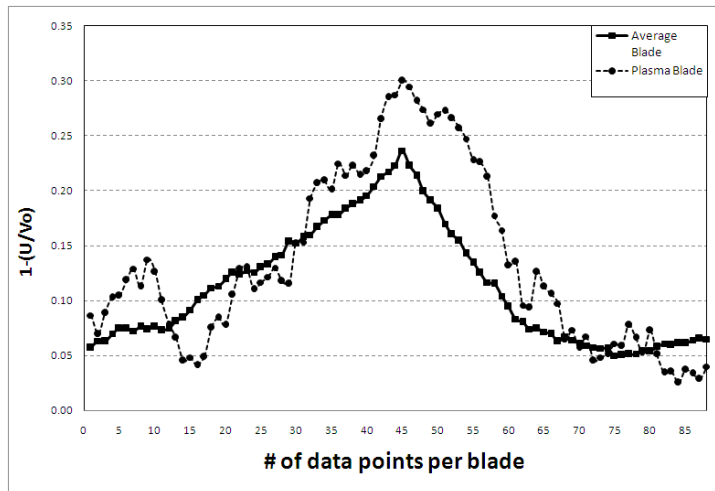


(b) Wake velocity for plasma blade

Figure 3.53: Wake velocity for 350 RPM per revolution (a), and per blade (b): Leading edge Counter Flow Plasma at $F = 30\text{Hz}$



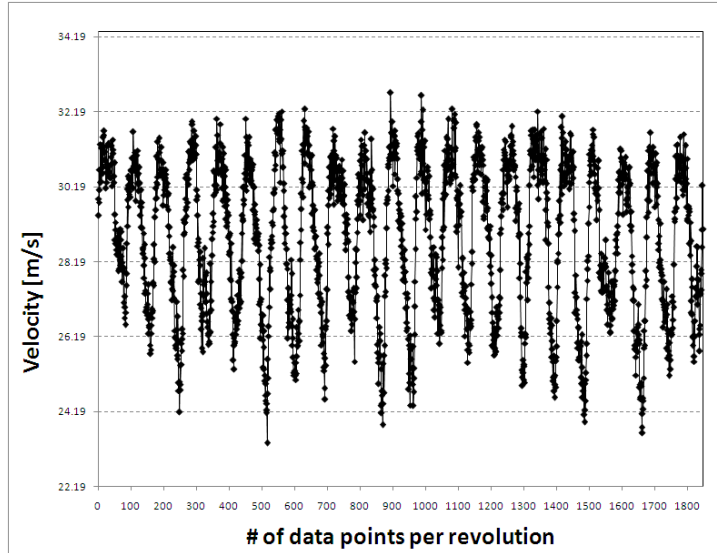
(a) Wake velocity per revolution



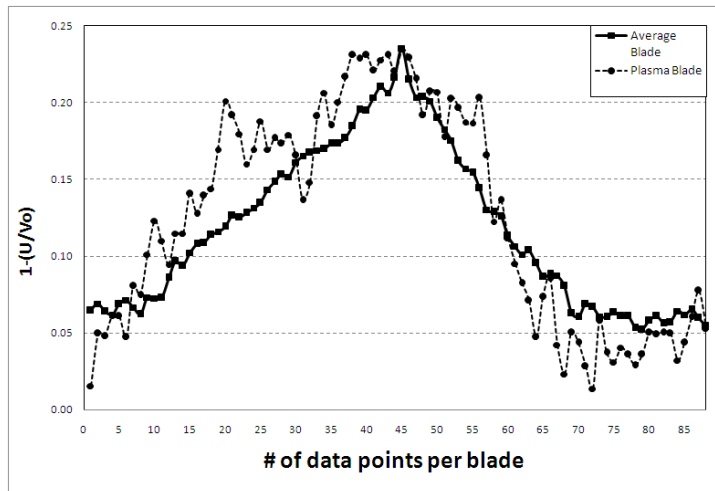
(b) Wake velocity for plasma blade

Figure 3.54: Wake velocity for 350 RPM per revolution (a), and per blade (b): Leading edge Counter Flow Plasma at $F = 50\text{Hz}$

The individual graphical results for the co-flow orientation can be seen in figure 3.55(a) through 3.59(b) for both the entire rotor revolution and for the plasma blade itself for the leading edge cases run at 350 RPM. In this group of figures the plasma blade wake is located in the seventh blade position and the mechanical trip remained installed on the eleventh blade position. It can be seen in these figures that mechanical trip is not always visually evident. It can also be seen in the plasma blade wake measurements at a forcing frequency of zero, which is steady plasma actuation, that the blade wake is much improved over that of the plasma blade in the off condition.

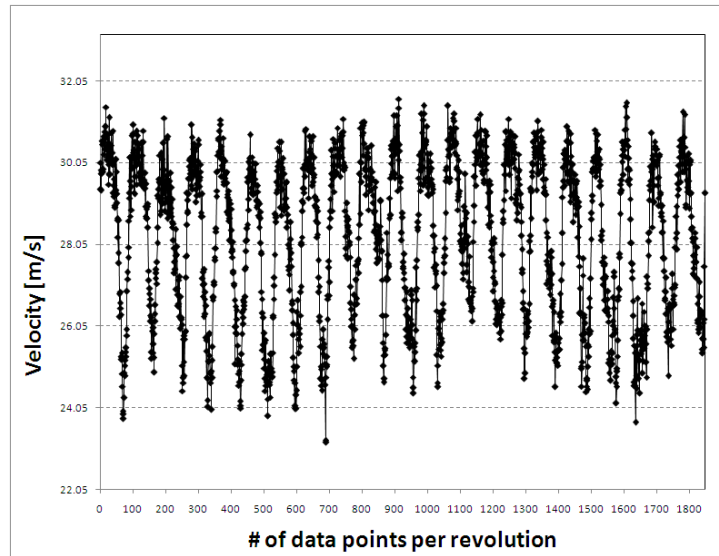


(a) Wake velocity per revolution

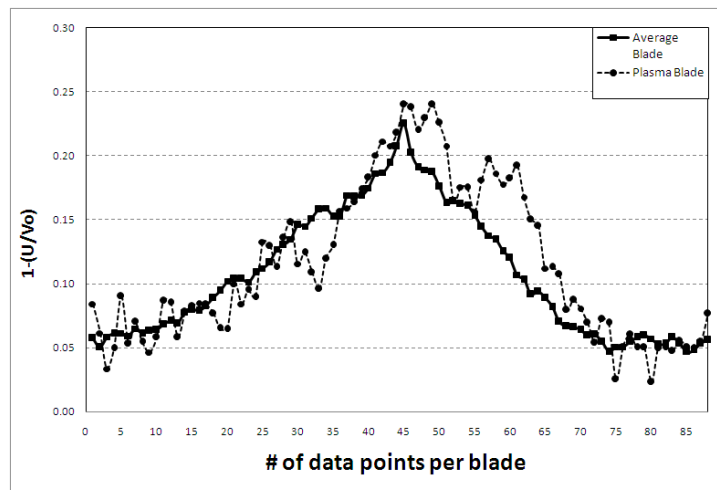


(b) Wake velocity for plasma blade

Figure 3.55: Wake velocity for 350 RPM per revolution (a), and per blade (b): Leading edge Co-Flow Plasma Off

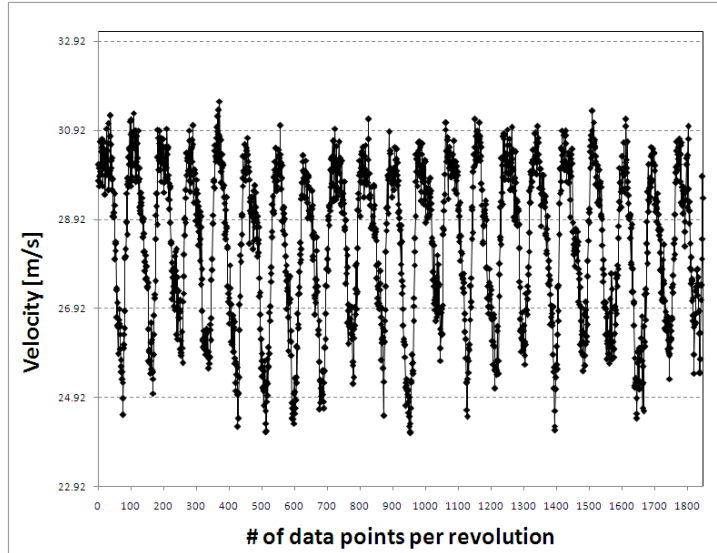


(a) Wake velocity per revolution

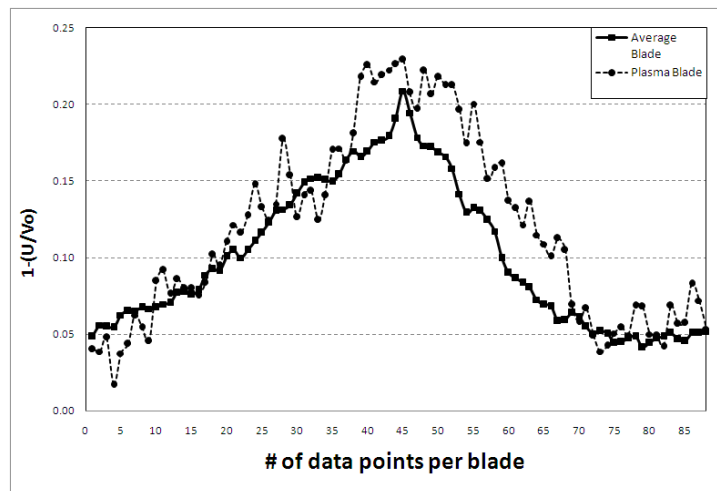


(b) Wake velocity for plasma blade

Figure 3.56: Wake velocity for 350 RPM per revolution (a), and per blade (b): Leading edge Co-Flow Plasma Steady

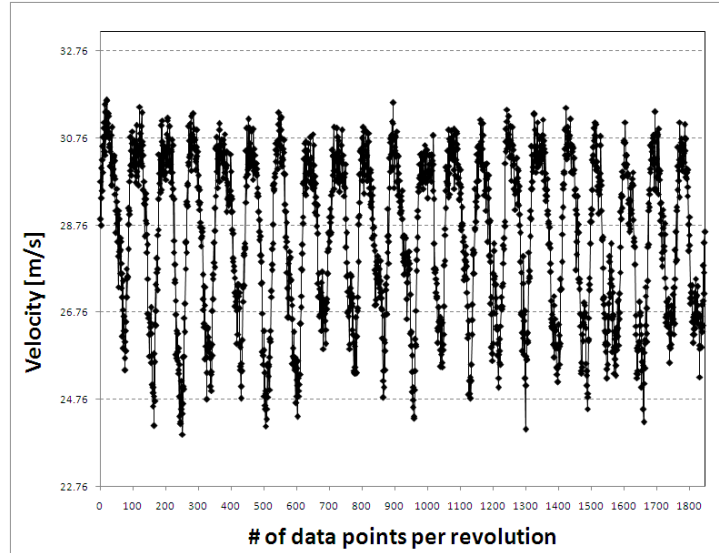


(a) Wake velocity per revolution

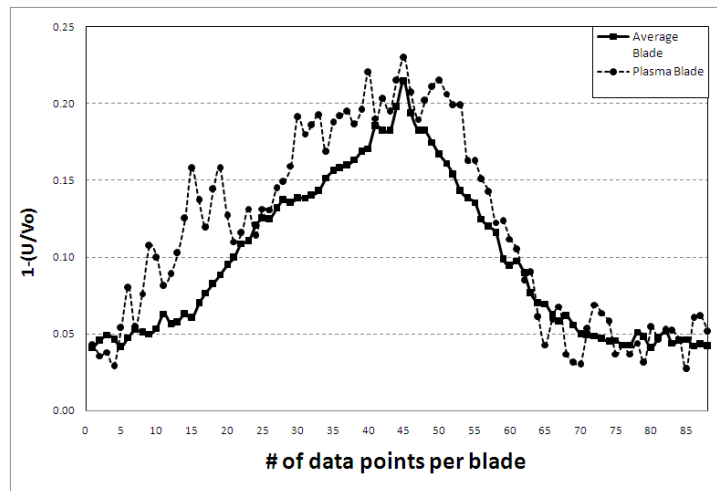


(b) Wake velocity for plasma blade

Figure 3.57: Wake velocity for 350 RPM per revolution (a), and per blade (b): Leading edge Co-Flow Plasma at $F = 10\text{Hz}$

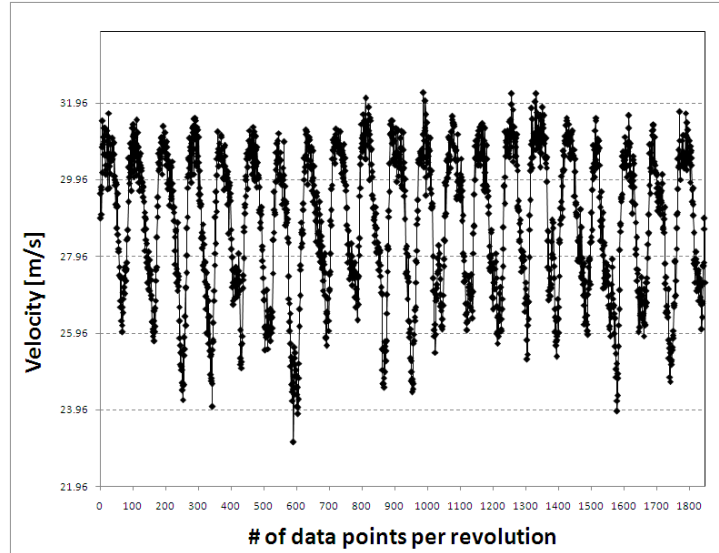


(a) Wake velocity per revolution

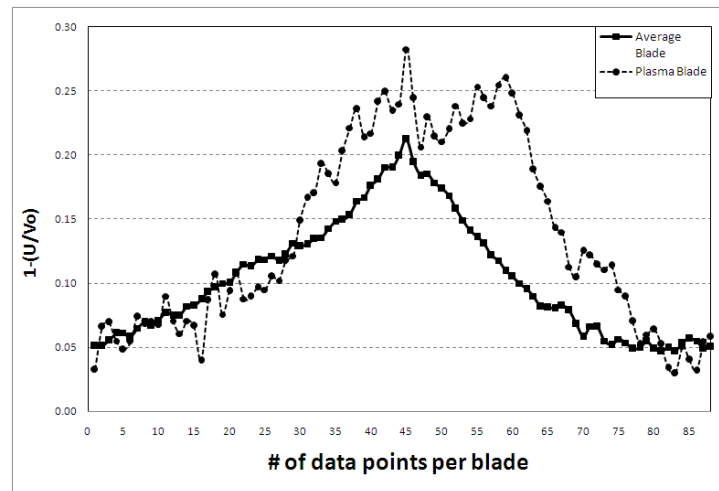


(b) Wake velocity for plasma blade

Figure 3.58: Wake velocity for 350 RPM per revolution (a), and per blade (b): Leading edge Co-Flow Plasma at $F = 30\text{Hz}$



(a) Wake velocity per revolution



(b) Wake velocity for plasma blade

Figure 3.59: Wake velocity for 350 RPM per revolution (a), and per blade (b): Leading edge Co-Flow Plasma at $F = 50\text{Hz}$

3.2.3 Comparison Between Reynolds Numbers

The counter and co-flow cases at 1/4 chord for both Reynolds numbers analyzed were compared further. This target area for further analysis was chosen due the trends which were visible in the data. The leading edge results appeared to possibly be random in nature so they were not explored further.

It can be seen in figure 3.60 that there are visible trends for both Reynolds numbers with the actuator in the co-flow orientation. The Re of 170,000 was for the 350 RPM and the Re of 260,000 was for the 600 RPM case. At a Re of 170,000 the forcing frequency of zero, thus steady actuation, had the most desirable effect of decreasing the drag by 12%. As the forcing frequency increased the deleterious effects to the flow increased as well, reaching a 10% increase in drag at a forcing frequency of 50 Hz. At a Re of 260,000 a forcing frequency of zero increased the drag by 13% as opposed to the 12% decrease over the lower Reynolds number. The drag continued to decrease in a steady trend until it reached its maximum of 18% drag reduction at a forcing frequency of 50 Hz.

As for the counter flow oriented actuator it can be seen in figure 3.61 that there are visible trends for both Reynolds numbers. It is of note that these results trend inversely of the co-flow results. Again the Re of 170,000 was for the 350 RPM and the Re of 260,000 was for the 600 RPM case. At a Re of 170,000 the forcing frequency of zero, thus steady actuation, had the most deleterious effect by increasing the drag by 9%. As the forcing frequency increased the effects became improved and actually reached a 4% decrease in drag at a forcing frequency of 50 Hz. At a Re of 260,000 a forcing frequency of zero had no effect on the flow as opposed to the 13% increase in drag that the co flow orientation showed. The drag continued to increase until it reached its minimum of 13% drag increase at a forcing frequency of 50 Hz.

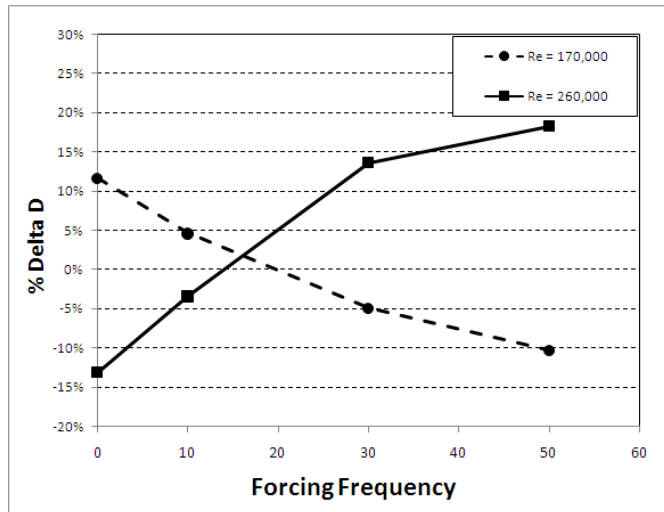


Figure 3.60: Change in drag on a co-flow actuator at 1/4 chord at various Reynolds numbers

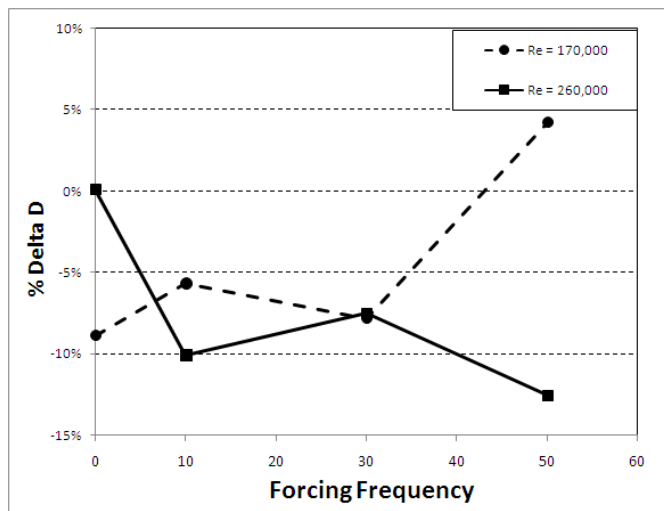


Figure 3.61: Change in drag for a counter flow actuator at 1/4 chord at various Reynolds numbers

CHAPTER 4

CONCLUSIONS

4.0.4 Discussion

Two configurations of a plasma actuator were experimented with in the quiescent state. PIV measurements were performed on actuators with Teflon and Kapton used as the dielectric material. The results of the quiescent PIV measurements showed that the actuators produced a wall jet in the boundary layer region. This resultant momentum was input in the region within one centimeter from the plasma surface. The velocity profiles for the Kapton and Teflon dielectrics with steady plasma actuation showed that the Kapton configuration only produce a maximum velocity of about 5 cm/s while the Teflon configuration produced a maximum velocity of about 40 cm/s. The velocity profiles for the same arrangement but for a forcing frequency of 50 Hz displayed maximum velocities of about 3 cm/s and 9 cm/s on the Kapton and Teflon configurations respectively. The Teflon dielectric configured actuator displayed the better performance at a lower power consumption level. This was attributed to the elevated magnitude of peak to peak voltage that was inherent to the Teflon configuration. Although the Teflon configuration required less average power the instantaneous power was greater due to the elevated driving voltage over the Kapton configuration. Momentum calculations were also performed on the two actuator configurations and an average compressor rotor blade wake. It was determined that the Teflon configured actuator input 1.16% of the momentum of the blade wake momentum deficit.

Blade wake momentum calculations were performed on the compressor rotor in response to various plasma actuator operating conditions. Both leading edge and 1/4

chord plasma actuator configurations were operated in both the counter and co-flow directions. The blade wake of the rotor was measured in this parametric analysis using a hotwire at relative Reynolds numbers of 170,000 and 260,000.

The compressor rotor momentum calculations showed that leading edge actuation can have an unpredictable effect and can cause an increase in drag, at these Reynolds numbers and power settings.

The optimum forcing frequency for a co-flow actuator at 1/4 chord was determined. The optimum condition was at steady actuation for a Reynolds number of 170,000 and at a forcing frequency of 50 Hz for a Reynolds number of 260,000. The counter flow actuator orientation at 1/4 chord showed decreased effects over the co-flow case. The maximum drag decrease was seen at a Reynolds number of 170,000 and a forcing frequency of 50 Hz.

Based upon the input power of the actuator of 12.75 W and the change in the blade power for the best case scenario of 0.523 W (where power is equal to drag times velocity), one can see that the power recovered by using the plasma actuator to decrease blade drag under these conditions is substantially lower than the actuator power, having an efficiency of approximately 4.1%. Hence, the final conclusion is that the potential for blade drag reduction is moderate at certain operating conditions.

4.0.5 Future work

These results are applicable to a single blade in a compressor rotor. It is reasoned that the effects would be comparable if applied to every blade in the rotor. Maximum drag reduction of a single blade was determined in this study to be approximately 18%. If this drag reduction could be experienced to the entire rotor flow field significant improvements are possible. The drag reduction may scale down by a certain factor with full rotor actuators, which could be a focus of further study, but even small drag reductions in off optimum compressor conditions could prove beneficial.

The drag reduction as a reactive device could prove beneficial for preventing off optimum conditions; such as a compressor entering a spike or modal stall condition. If the situation could be detected a control system could activate the plasma actuators decreasing the drag in a certain quadrant of rotor blades, for spike stall prevention, or the entire rotor of blades to reduce the effect of a modal stall. As compressor rotor blade drag is decreased the flow velocity is increased. This has the potential of increasing downstream pressure for the same amount of work input, or decreasing the amount of work input to achieve the same pressure ratio.

One area of improvement for this study would be the survivability of the actuator itself. Actuators are prone to burn through if the dielectric becomes too hot, or has some compromised area, or if an unexpected power burst occurs. Alternate dielectric materials should be explored with the possibility of embedding the actuator in a compressor blade. This would be optimized over adhering it to the surface of the blade. Also, as displayed in this study and others, a counter flow actuator actually has benefits over a co-flow actuator at certain operating conditions. Further study could be focused on this area to either design a single actuator that has counter and co-flow capabilities, or by equipping the compressor rotor blades with alternating actuator types.

A second area of improvement would be that of the transformer. To limit variables in this study a single transformer was used throughout. Also to simplify this study it was decided to pulse the power signal before it entered the transformer. This limited the magnitude of the forcing frequency due to the response time of the transformer. It was determined experimentally that the subject transformer would only show a pulsed signal at a maximum forcing frequency of 50 Hz. Any forcing frequencies greater than 50 Hz no longer appeared pulsed, it was steady in appearance. The subject transformer was also limited to a 15 V input, thus limiting the total power of the actuator. Thus by exploring with different transformers one could create a stronger

plasma field and have the ability to increase the forcing frequency. Experience has shown that a reduced forcing frequency of about one usually has the peak effectiveness on the flow. Thus for this set of experiments a forcing frequency on the order of 250 Hz would have had the optimum effects on the flow.

Further studies could also involve varying the mass flow through the compressor, and measuring the flow field at different spans. This would allow one to characterize the actuation phenomena throughout the compressor map. Variations in forcing frequency duty cycle could also be performed. Experience has proven this to be an effective method to decrease power requirements.

APPENDIX A

Labview Front Panel and Block Diagram

Labview was used exclusively to monitor, collect, and analyze data during the parametric analysis. The data received from the Laser and the hotwire was controlled through LabView using the front panel and block diagram found here. This code was created in order to receive the data from the instrumentation, control the sampling rate, and write measurement files which were later used to analyze the data. Formulas were also incorporated into the code to provide real time data for flow velocities and RPM. The DCC sampling rate was adjusted using Labview. Sampling rates of 5 kHz to 50 kHz were used during the course of this research.

The front panel displays real time laser and hotwire voltage signals. The Laser signal is fed through a timing and transition measurement block where the RPM is calculated. This value is shown on the front panel. A formula was instituted to calculate the number of revolutions per second in order to calculate the number of blade passes per second. These two values are also shown on the front panel. A spectral measurement block was added in order to perform a fast fourier transform (FFT) on the hotwire signal. This FFT showed a peak at the frequency of the blades passing. This was compared to the laser measurement calculations of blade frequency to insure accuracy. It is of note that the FFT showed no clear blade frequency signal unless the mass flow fan was on.

It can also be seen in the block diagram that the signals for four pressure transducers were available for further research. These pressure transducers which were installed in the OSCAR DAQ facility were not utilized for this present study.

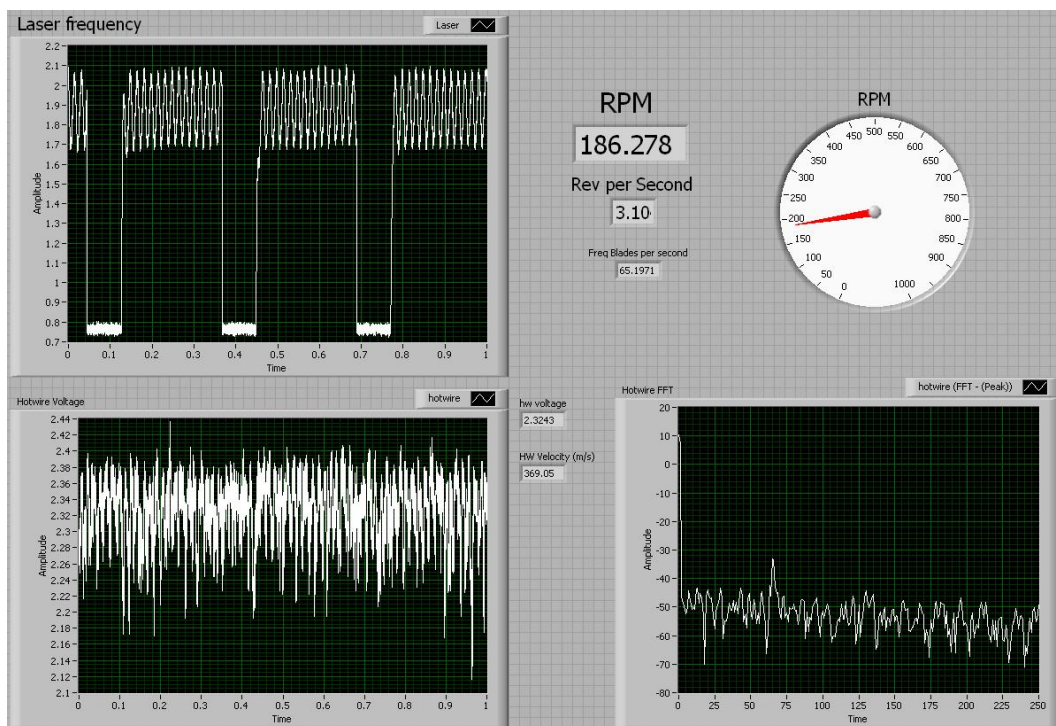


Figure A.1: Screen shot of Labview front panel

APPENDIX B

Visual Basic Code: Window Averaging Algorithm

```
Dim LAS(60000) As Single, Ind(1000) As Single, i As Single,  
Lstore As Single, Diff(60000) As Single, AVG(50000),  
Bmin As Double, Bmax As Double, Iavg As Integer
```

```
Sub average()
```

```
n = 1
```

```
s = 1
```

```
For i = 2 To 50000
```

```
    Lstore = LAS(i - 1)
```

```
    LAS(i) = Cells(i, 2)
```

```
    Diff(i) = LAS(i) - Lstore
```

```
    If Diff(i) < -0.9 Then
```

```
        Ind(n) = i
```

```
        n = n + 1
```

```
    End If
```

```
Next i
```

```

j = 1
Iavg = (Ind(2) - Ind(1))

'Deterime Iavg - the average number of data
'points per revolution
For i = 1 To 999

Cells(i + 1, 4) = Ind(i)
If Ind(i + 1) = 0 Then GoTo 20

If (Ind(i + 1) - Ind(i)) > Iavg + 10 Or (Ind(i + 1) - Ind(i)) <
  < Iavg - 10 Then GoTo 50

Isum = Isum + (Ind(i + 1) - Ind(i))
Iavg = Isum / j
j = j + 1
50
Next i
20
Cells(2, 6) = Iavg

'Print hotwire voltage values to Sheet 2- Each column
'is 1 revolution (Revloutions which have
'number of data points +/-20 of the Average are excluded
' from the Window Average algorithm)

```

```

For i = 2 To 1000

    If Finish < -500 Then GoTo 10

    Startold = Start
    Start = Ind(i) - 1
    Finold = Finish
    Finish = Ind(i + 1) - Ind(i)

    If Finish < Iavg - 20 Then GoTo 10
    If Finish > Iavg + 20 Then GoTo 10

    Calculate

    For j = 1 To Finish
        Sheet2.Cells(j + 1, s) = Cells(Start + j, 3)
    Next j

10

    s = s + 1

Next i

'Write window Averaged voltage values from sheet two to sheet one
For i = 1 To Iavg

Cells(i + 1, 7) = "=AVERAGE(Sheet2!RC[-6]:RC[39])"

Next i

```

```
Cells(2, 6) = Iavg
```

```
End Sub
```

```
Sub bladeaverage()
```

```
Dim myRange As Range, AVG(5000) As Single, Iavg As Integer, _  
Ind(5000), Interval As Integer
```

```
Iavg = Cells(2, 6)
```

```
For i = 2 To Iavg
```

```
AVG(i - 1) = Cells(i, 7)
```

```
Next i
```

```
Set myRange = Worksheets("Sheet1").Range("G2:G2500")
```

```
Bmax = Application.WorksheetFunction.Max(AVG)
```

```
Bmin = Application.WorksheetFunction.Min(myRange)
```

```
Cells(4, 6) = Bmax
```

```
Cells(5, 6) = Bmin
```

```
j = 1
```

```
'Find the lowest velocity in the wake of each blade
```

```
For i = 2 To Iavg
```

```
Middle = Bmax - ((Bmax - Bmin) / 2) * 1 'This value of 1 may
```

```
'need to be modified at different RPM
```

```

If AVG(i) > Middle Then GoTo 40
If AVG(i + 1) < AVG(i) Or AVG(i + 2) <
  < AVG(i) Or AVG(i + 3) <
< AVG(i) Or AVG(i + 4) < AVG(i) _
  Or AVG(i + 5) < AVG(i) _
Or AVG(i + 6) < AVG(i) Or AVG(i + 7) <
  < AVG(i) Or AVG(i + 8) < AVG(i) _
Or AVG(i + 9) < AVG(i) Or AVG(i + 10) <
  < AVG(i) Or AVG(i + 11) < AVG(i) _
Or AVG(i + 12) < AVG(i) Or AVG(i + 13) <
  < AVG(i) Or AVG(i + 14) < AVG(i) _
Or AVG(i + 15) < AVG(i) Or AVG(i + 16) <
  < AVG(i) Or AVG(i + 17) < AVG(i) _
Or AVG(i + 18) < AVG(i) Or AVG(i + 19) <
  < AVG(i) Or AVG(i + 20) < AVG(i) _

```

```

Then GoTo 40

```

```

  Ind(j) = i - 1

```

```

  Interval = (Iavg / 21) / 2

```

```

  i = i + Interval

```

```

  j = j + 1

```

```

Cells(6, 6) = j

```

```

40

```

```

Next i

```

```

For i = 1 To Iavg / 21
Cells(i + 1, 9) = Ind(i)
Next i

For i = 1 To 20

    For j = 1 To 2 * Interval
        If Ind(i) < Interval Then GoTo 77
        Sheet3.Cells(j, i) = AVG(Ind(i) - (Interval - j))
    Next j
77
Next i

tripbld = Application.InputBox( _
    prompt:="Select a trip blade location", Type:=1)

For j = 1 To 2 * Interval

Sheet1.Cells(j + 1, 12) = AVG(Ind(tripbld) - (Interval - j))
Next j

removetripbld = MsgBox("Remove Trip blade from average?", _
    vbYesNo, "trip blade")

If removetripbld <> 6 Then GoTo 70
For i = 1 To Interval * 2
Sheet3.Cells(i, tripbld) = ""

```

Next i

70

```
Set twoRange = Worksheets("Sheet1").Range("h2:h1000")
```

```
Pmax = Application.WorksheetFunction.Max(twoRange)
```

```
Pmin = Application.WorksheetFunction.Min(twoRange)
```

```
    ActiveSheet.ChartObjects("Chart 6").Activate
```

```
    ActiveChart.Axes(xlValue).Select
```

```
    ActiveSheet.ChartObjects("Chart 6").Activate
```

```
    ActiveChart.Axes(xlValue).MinimumScale = Pmin - Pmin * 0.05
```

```
    ActiveChart.Axes(xlValue).MaximumScale = Pmax + Pmax * 0.05
```

```
    ActiveSheet.ChartObjects("Chart 6").Activate
```

```
    ActiveChart.Axes(xlCategory).Select
```

```
    ActiveSheet.ChartObjects("Chart 6").Activate
```

```
    ActiveChart.Axes(xlCategory).MaximumScale = Iavg
```

```
    ActiveChart.Axes(xlCategory).MinimumScale = 0
```

```
    ActiveSheet.ChartObjects("Chart 3").Activate
```

```
    ActiveChart.Axes(xlCategory).Select
```

```
    ActiveSheet.ChartObjects("Chart 3").Activate
```

```
    ActiveChart.Axes(xlCategory).MaximumScale = Interval * 2
```

```
    Range("P31").Select
```

```
Sheet3.Range("k1:k5000") = ""
```

End Sub

```

Sub clear()
    Sheet1.Range("d2:d5000") = ""
    Sheet2.Range("a2:bd5000") = ""
    Sheet1.Range("g2:g5000") = ""
End Sub

Sub clear1()
    Sheet1.Range("l2:l1000") = ""
    Sheet1.Range("i2:i1000") = ""
    Sheet3.Range("a1:AA5000") = ""
End Sub

Sub clear2()
    cleardata = MsgBox("Are you sure you want to delete _
the data?", vbYesNo, "R U sure")

If cleardata <> 6 Then GoTo 70
    Sheet1.Range("a2:c60000") = ""
70

End Sub

```

APPENDIX C

XFOIL Supplementary Data

XFOIL Dump File for 350 RPM

#	s	x	y	Ue/Vinf	Dstar	Theta	Cf	H
0.00000	1.00000	0.00000	0.91907	0.025395	0.014905	0.001671	1.704	
0.00859	0.99142	0.00044	0.92408	0.024647	0.014600	0.001743	1.688	
0.02218	0.97785	0.00118	0.92829	0.024091	0.014344	0.001792	1.680	
0.03652	0.96354	0.00207	0.93245	0.023566	0.014095	0.001839	1.672	
0.05151	0.94859	0.00317	0.93747	0.022942	0.013804	0.001899	1.662	
0.06722	0.93294	0.00459	0.94417	0.022118	0.013432	0.001989	1.647	
0.08374	0.91651	0.00628	0.95240	0.021151	0.012997	0.002107	1.627	
0.10113	0.89922	0.00819	0.96171	0.020126	0.012527	0.002244	1.607	
0.11930	0.88117	0.01023	0.97138	0.019139	0.012062	0.002387	1.587	
0.13808	0.86251	0.01238	0.98144	0.018186	0.011602	0.002539	1.568	
0.15735	0.84338	0.01464	0.99206	0.017252	0.011141	0.002703	1.549	
0.17700	0.82387	0.01698	1.00335	0.016330	0.010676	0.002882	1.530	
0.19693	0.80408	0.01938	1.01505	0.015445	0.010221	0.003073	1.511	
0.21701	0.78414	0.02178	1.02697	0.014610	0.009781	0.003271	1.494	
0.23714	0.76416	0.02417	1.03895	0.013833	0.009363	0.003474	1.477	
0.25723	0.74421	0.02652	1.05103	0.013104	0.008962	0.003684	1.462	
0.27722	0.72435	0.02882	1.06313	0.012423	0.008581	0.003899	1.448	
0.29708	0.70461	0.03105	1.07531	0.011784	0.008217	0.004122	1.434	
0.31680	0.68501	0.03319	1.08726	0.011197	0.007877	0.004344	1.421	
0.33637	0.66555	0.03524	1.09916	0.010648	0.007554	0.004572	1.410	
0.35579	0.64623	0.03719	1.11075	0.010145	0.007252	0.004798	1.399	
0.37505	0.62706	0.03904	1.12241	0.009667	0.006962	0.005032	1.388	
0.39414	0.60804	0.04076	1.13370	0.009229	0.006693	0.005263	1.379	
0.41308	0.58918	0.04237	1.14498	0.008813	0.006434	0.005501	1.370	
0.43185	0.57046	0.04384	1.15575	0.008436	0.006195	0.005732	1.362	
0.45046	0.55190	0.04517	1.16644	0.008078	0.005967	0.005967	1.354	
0.46890	0.53350	0.04636	1.17694	0.007742	0.005750	0.006204	1.346	
0.48719	0.51524	0.04739	1.18669	0.007441	0.005553	0.006427	1.340	
0.50536	0.49708	0.04824	1.19567	0.007172	0.005374	0.006635	1.335	
0.52349	0.47897	0.04891	1.20298	0.006954	0.005224	0.006802	1.331	

0.54162	0.46084	0.04941	1.20944	0.006762	0.005089	0.006947	1.329
0.55979	0.44267	0.04975	1.21538	0.006588	0.004964	0.007077	1.327
0.57801	0.42446	0.04994	1.22086	0.006430	0.004847	0.007191	1.327
0.59628	0.40619	0.04998	1.22613	0.006281	0.004734	0.007296	1.327
0.61459	0.38788	0.04988	1.23105	0.006144	0.004627	0.007384	1.328
0.63294	0.36953	0.04964	1.23578	0.006016	0.004524	0.007459	1.330
0.65131	0.35116	0.04927	1.24039	0.005897	0.004423	0.007519	1.333
0.66967	0.33281	0.04878	1.24562	0.005771	0.004317	0.007584	1.337
0.68796	0.31453	0.04817	1.25108	0.005649	0.004210	0.007638	1.342
0.70613	0.29638	0.04745	1.25660	0.005534	0.004105	0.007674	1.348
0.72411	0.27841	0.04661	1.26254	0.005422	0.003997	0.007695	1.356
0.74185	0.26070	0.04566	1.26864	0.005318	0.003891	0.007690	1.367
0.75925	0.24333	0.04461	1.27502	0.005223	0.003784	0.007653	1.380
0.77623	0.22639	0.04347	1.28151	0.005143	0.003681	0.007571	1.397
0.79269	0.20998	0.04224	1.28835	0.005075	0.003577	0.007440	1.419
0.80851	0.19421	0.04094	1.29527	0.005029	0.003478	0.007240	1.446
0.82359	0.17919	0.03960	1.30275	0.004999	0.003378	0.006974	1.480
0.83784	0.16501	0.03823	1.31041	0.004999	0.003281	0.006616	1.524
0.85118	0.15174	0.03685	1.31875	0.005025	0.003183	0.006167	1.579
0.86358	0.13941	0.03548	1.32776	0.005086	0.003085	0.005615	1.648
0.87504	0.12803	0.03413	1.33791	0.005184	0.002983	0.004960	1.738
0.88559	0.11757	0.03281	1.34946	0.005331	0.002874	0.004199	1.855
0.89528	0.10796	0.03153	1.36349	0.005522	0.002750	0.003363	2.008
0.90418	0.09915	0.03028	1.38129	0.005751	0.002600	0.002496	2.212
0.91235	0.09107	0.02907	1.40389	0.006019	0.002419	0.001705	2.488
0.91987	0.08364	0.02790	1.43296	0.006288	0.002195	0.001054	2.864
0.92681	0.07679	0.02677	1.46930	0.006547	0.001930	0.000380	3.393
0.93322	0.07048	0.02569	1.51385	0.006760	0.001624	-0.000199	4.163
0.93915	0.06463	0.02464	1.56551	0.006914	0.001295	-0.000497	5.339
0.94467	0.05921	0.02362	1.61802	0.007000	0.000988	-0.000574	7.084
0.94982	0.05416	0.02263	1.67554	0.006994	0.000681	-0.000618	10.270
0.95463	0.04944	0.02165	1.75068	0.006841	0.000305	-0.000674	22.454
0.95915	0.04503	0.02069	1.76690	0.006708	0.000238	-0.0002453	28.144
0.96340	0.04089	0.01975	1.76974	0.006491	0.000229	-0.0002560	28.385
0.96741	0.03699	0.01883	1.77235	0.006186	0.000220	-0.0002661	28.073
0.97120	0.03331	0.01792	1.77480	0.005814	0.000213	-0.0002758	27.282
0.97479	0.02983	0.01703	1.77715	0.005387	0.000207	-0.0002850	26.055
0.97820	0.02653	0.01616	1.77940	0.004910	0.000201	-0.0002937	24.395
0.98144	0.02341	0.01530	1.78157	0.004381	0.000197	-0.0003019	22.279
0.98454	0.02043	0.01444	1.78376	0.003817	0.000193	-0.0003099	19.814
0.98749	0.01761	0.01356	1.78618	0.003243	0.000189	-0.0003187	17.175

0.99032	0.01494	0.01263	1.78915	0.002673	0.000185	-0.003297	14.473
0.99304	0.01240	0.01165	1.79329	0.002118	0.000180	-0.003453	11.781
0.99566	0.01000	0.01060	1.79991	0.001587	0.000173	-0.003715	9.166
0.99819	0.00775	0.00946	1.81227	0.001097	0.000163	-0.004277	6.721
1.00063	0.00566	0.00819	1.83905	0.000673	0.000147	-0.004346	4.563
1.00300	0.00379	0.00673	1.89211	0.000413	0.000124	0.009282	3.322
1.00532	0.00218	0.00506	1.96149	0.000273	0.000098	0.036172	2.801
1.00759	0.00090	0.00319	2.01363	0.000196	0.000073	0.060467	2.678
1.00982	0.00010	0.00111	1.97788	0.000122	0.000051	0.134650	2.366
1.01203	0.00010	-0.00111	1.58004	0.000099	0.000046	0.157903	2.173
1.01427	0.00090	-0.00319	1.04256	0.000121	0.000055	0.083563	2.198
1.01654	0.00218	-0.00506	0.66967	0.000139	0.000064	0.046766	2.191
1.01885	0.00379	-0.00673	0.39354	0.000162	0.000073	0.022967	2.224
1.02123	0.00566	-0.00819	0.18028	0.000176	0.000079	0.009710	2.219
1.02367	0.00775	-0.00946	0.01929	0.000230	0.000103	0.000791	2.230
1.02620	0.01000	-0.01060	-0.09963	0.000230	0.000103	0.004084	2.230
1.02882	0.01240	-0.01165	-0.19214	0.000280	0.000123	0.006150	2.283
1.03153	0.01494	-0.01263	-0.26120	0.000311	0.000138	0.007785	2.248
1.03437	0.01761	-0.01356	-0.32325	0.000334	0.000148	0.008858	2.261
1.03732	0.02043	-0.01444	-0.36996	0.000380	0.000165	0.008502	2.310
1.04042	0.02341	-0.01530	-0.40917	0.000410	0.000179	0.008913	2.288
1.04366	0.02653	-0.01616	-0.44490	0.000441	0.000192	0.008941	2.296
1.04707	0.02983	-0.01703	-0.47822	0.000465	0.000203	0.009153	2.290
1.05066	0.03331	-0.01792	-0.50840	0.000496	0.000215	0.009023	2.303
1.05445	0.03699	-0.01883	-0.53666	0.000521	0.000227	0.009068	2.301
1.05846	0.04089	-0.01975	-0.56452	0.000543	0.000237	0.009208	2.295
1.06271	0.04503	-0.02069	-0.58943	0.000577	0.000249	0.008875	2.316
1.06722	0.04945	-0.02165	-0.61330	0.000603	0.000261	0.008859	2.313
1.07204	0.05416	-0.02263	-0.63563	0.000635	0.000274	0.008642	2.322
1.07718	0.05921	-0.02362	-0.65621	0.000670	0.000288	0.008380	2.331
1.08270	0.06463	-0.02464	-0.67582	0.000704	0.000301	0.008193	2.335
1.08864	0.07048	-0.02569	-0.69444	0.000740	0.000316	0.007964	2.340
1.09505	0.07679	-0.02677	-0.71212	0.000778	0.000332	0.007722	2.346
1.10198	0.08364	-0.02790	-0.72999	0.000811	0.000346	0.007630	2.342
1.10951	0.09107	-0.02907	-0.74762	0.000848	0.000362	0.007465	2.343
1.11768	0.09915	-0.03028	-0.76399	0.000893	0.000379	0.007158	2.355
1.12658	0.10796	-0.03153	-0.78079	0.000929	0.000395	0.007065	2.350
1.13627	0.11757	-0.03281	-0.79682	0.000975	0.000414	0.006818	2.358
1.14682	0.12803	-0.03413	-0.81195	0.001026	0.000433	0.006553	2.366
1.15828	0.13941	-0.03548	-0.82675	0.001074	0.000454	0.006356	2.368
1.17068	0.15174	-0.03685	-0.84096	0.001126	0.000475	0.006139	2.373

1.18402	0.16501	-0.03823	-0.85482	0.001178	0.000496	0.005957	2.375
1.19827	0.17919	-0.03960	-0.86830	0.001230	0.000518	0.005789	2.376
1.21335	0.19421	-0.04094	-0.88133	0.001282	0.000540	0.005631	2.377
1.22917	0.20998	-0.04224	-0.89357	0.001338	0.000562	0.005450	2.381
1.24563	0.22639	-0.04347	-0.90509	0.001393	0.000584	0.005285	2.384
1.26261	0.24333	-0.04461	-0.91585	0.001449	0.000607	0.005126	2.387
1.28001	0.26070	-0.04566	-0.92594	0.001503	0.000629	0.004983	2.390
1.29775	0.27841	-0.04661	-0.93524	0.001558	0.000651	0.004835	2.393
1.31573	0.29638	-0.04745	-0.94380	0.001614	0.000673	0.004694	2.397
1.33390	0.31453	-0.04817	-0.95196	0.001665	0.000694	0.004587	2.398
1.35219	0.33281	-0.04878	-0.95976	0.001713	0.000714	0.004498	2.397
1.37054	0.35116	-0.04927	-0.96692	0.001763	0.000735	0.004388	2.400
1.38892	0.36953	-0.04964	-0.97383	0.001809	0.000754	0.004312	2.400
1.40727	0.38788	-0.04988	-0.98030	0.001855	0.000773	0.004229	2.401
1.42558	0.40619	-0.04998	-0.98636	0.001900	0.000791	0.004146	2.402
1.44385	0.42446	-0.04994	-0.99151	0.001955	0.000811	0.004016	2.411
1.46206	0.44267	-0.04975	-0.99589	0.002013	0.000831	0.003874	2.422
1.48024	0.46084	-0.04941	-0.99988	0.002068	0.000851	0.003757	2.429
1.49837	0.47897	-0.04891	-1.00277	0.002136	0.000873	0.003585	2.446
1.51649	0.49708	-0.04824	-1.00470	0.002213	0.000897	0.003392	2.467
1.53467	0.51524	-0.04739	-1.00504	0.002316	0.000925	0.003121	2.503
1.55296	0.53350	-0.04636	-1.00392	0.002439	0.000957	0.002813	2.550
1.57140	0.55190	-0.04517	-1.00214	0.002565	0.000989	0.002544	2.593
1.59001	0.57046	-0.04384	-0.99970	0.002697	0.001023	0.002294	2.637
1.60878	0.58918	-0.04237	-0.99678	0.002834	0.001057	0.002067	2.680
1.62771	0.60804	-0.04076	-0.99344	0.002978	0.001093	0.001856	2.725
1.64681	0.62706	-0.03904	-0.98964	0.003136	0.001130	0.001647	2.775
1.66607	0.64623	-0.03719	-0.98547	0.003308	0.001169	0.001445	2.830
1.68549	0.66555	-0.03524	-0.98100	0.003495	0.001209	0.001249	2.892
1.70506	0.68501	-0.03319	-0.97629	0.003701	0.001250	0.001058	2.962
1.72477	0.70461	-0.03105	-0.97134	0.003935	0.001292	0.000865	3.046
1.74464	0.72435	-0.02882	-0.96625	0.004204	0.001335	0.000673	3.148
1.76463	0.74421	-0.02652	-0.96119	0.004501	0.001379	0.000493	3.265
1.78472	0.76416	-0.02417	-0.95625	0.004837	0.001421	0.000325	3.403
1.80484	0.78414	-0.02178	-0.95160	0.005202	0.001463	0.000181	3.556
1.82492	0.80408	-0.01938	-0.94729	0.005613	0.001502	0.000053	3.737
1.84486	0.82387	-0.01698	-0.94338	0.006060	0.001539	-0.000050	3.939
1.86451	0.84338	-0.01464	-0.93989	0.006517	0.001573	-0.000122	4.144
1.88377	0.86251	-0.01238	-0.93673	0.006956	0.001604	-0.000167	4.336
1.90256	0.88117	-0.01023	-0.93388	0.007383	0.001634	-0.000193	4.518
1.92073	0.89922	-0.00819	-0.93135	0.007803	0.001662	-0.000209	4.696

1.93811	0.91651	-0.00628	-0.92913	0.008229	0.001687	-0.000217	4.879
1.95464	0.93294	-0.00459	-0.92714	0.008555	0.001710	-0.000219	5.004
1.97035	0.94859	-0.00317	-0.92530	0.008712	0.001732	-0.000216	5.030
1.98534	0.96354	-0.00207	-0.92349	0.008649	0.001754	-0.000210	4.932
1.99967	0.97785	-0.00118	-0.92174	0.008457	0.001775	-0.000199	4.765
2.01326	0.99142	-0.00044	-0.92006	0.008266	0.001795	-0.000183	4.605
2.02186	1.00000	0.00000	-0.91907	0.008463	0.001807	-0.000146	4.684
2.02186	1.00010	0.00000	0.91907	0.033859	0.016712	0.000000	2.026
2.03045	1.00869	0.00003	0.92284	0.032315	0.016441	0.000000	1.965
2.04032	1.01856	0.00012	0.92482	0.031335	0.016302	0.000000	1.922
2.05165	1.02989	0.00027	0.92675	0.030386	0.016170	0.000000	1.879
2.06466	1.04290	0.00049	0.92867	0.029452	0.016042	0.000000	1.836
2.07961	1.05784	0.00079	0.93063	0.028520	0.015914	0.000000	1.792
2.09677	1.07500	0.00118	0.93261	0.027592	0.015787	0.000000	1.748
2.11647	1.09470	0.00169	0.93459	0.026673	0.015662	0.000000	1.703
2.13910	1.11732	0.00234	0.93652	0.025773	0.015544	0.000000	1.658
2.16509	1.14329	0.00317	0.93833	0.024901	0.015435	0.000000	1.613
2.19493	1.17312	0.00421	0.93992	0.024069	0.015341	0.000000	1.569
2.22921	1.20737	0.00550	0.94119	0.023288	0.015268	0.000000	1.525
2.26856	1.24669	0.00712	0.94197	0.022575	0.015224	0.000000	1.483
2.31375	1.29184	0.00911	0.94205	0.021945	0.015219	0.000000	1.442
2.36565	1.34368	0.01157	0.94112	0.021427	0.015271	0.000000	1.403
2.42525	1.40320	0.01458	0.93867	0.021061	0.015406	0.000000	1.367
2.49369	1.47154	0.01825	0.93372	0.020930	0.015682	0.000000	1.335
2.57228	1.55000	0.02272	0.92426	0.021217	0.016221	0.000000	1.308
2.66253	1.64009	0.02814	0.90530	0.022436	0.017370	0.000000	1.292
2.76618	1.74353	0.03469	0.86171	0.026643	0.020439	0.000000	1.304
2.88519	1.86229	0.04257	0.76705	0.042648	0.030210	0.000000	1.412
3.02187	1.99863	0.05203	0.71782	0.214907	0.042713	0.000000	5.031

XFOIL Dump File for 600 RPM

#	s	x	y	Ue/Vinf	Dstar	Theta	Cf	H
0.00000	1.00000	0.00000	1.25086	0.417136	0.030750	-0.000009	13.565	
0.00859	0.99142	0.00044	1.25153	0.413754	0.030494	-0.000009	13.568	
0.02218	0.97785	0.00118	1.25266	0.410043	0.030070	-0.000009	13.636	
0.03652	0.96354	0.00207	1.25386	0.406168	0.029621	-0.000009	13.712	
0.05151	0.94859	0.00317	1.25512	0.401945	0.029154	-0.000010	13.787	
0.06722	0.93294	0.00459	1.25646	0.397227	0.028669	-0.000010	13.856	
0.08374	0.91651	0.00628	1.25787	0.391977	0.028162	-0.000010	13.919	
0.10113	0.89922	0.00819	1.25937	0.386226	0.027631	-0.000010	13.978	
0.11930	0.88117	0.01023	1.26096	0.380073	0.027078	-0.000010	14.036	
0.13808	0.86251	0.01238	1.26263	0.373567	0.026508	-0.000011	14.093	
0.15735	0.84338	0.01464	1.26438	0.366729	0.025926	-0.000011	14.145	
0.17700	0.82387	0.01698	1.26618	0.359575	0.025334	-0.000011	14.194	
0.19693	0.80408	0.01938	1.26805	0.352161	0.024735	-0.000011	14.238	
0.21701	0.78414	0.02178	1.26998	0.344560	0.024133	-0.000012	14.278	
0.23714	0.76416	0.02417	1.27194	0.336822	0.023531	-0.000012	14.314	
0.25723	0.74421	0.02652	1.27396	0.328987	0.022931	-0.000012	14.347	
0.27722	0.72435	0.02882	1.27601	0.321078	0.022336	-0.000013	14.375	
0.29708	0.70461	0.03105	1.27810	0.313132	0.021745	-0.000013	14.400	
0.31680	0.68501	0.03319	1.28023	0.305165	0.021158	-0.000013	14.423	
0.33637	0.66555	0.03524	1.28240	0.297195	0.020577	-0.000014	14.443	
0.35579	0.64623	0.03719	1.28462	0.289231	0.020000	-0.000014	14.461	
0.37505	0.62706	0.03904	1.28688	0.281276	0.019429	-0.000015	14.477	
0.39414	0.60804	0.04076	1.28920	0.273352	0.018862	-0.000015	14.492	
0.41308	0.58918	0.04237	1.29157	0.265465	0.018300	-0.000016	14.506	
0.43185	0.57046	0.04384	1.29399	0.257626	0.017742	-0.000016	14.521	
0.45046	0.55190	0.04517	1.29647	0.249841	0.017189	-0.000017	14.535	
0.46890	0.53350	0.04636	1.29902	0.242118	0.016640	-0.000017	14.550	
0.48719	0.51524	0.04739	1.30163	0.234471	0.016095	-0.000018	14.568	
0.50536	0.49708	0.04824	1.30433	0.226913	0.015552	-0.000019	14.590	
0.52349	0.47897	0.04891	1.30712	0.219439	0.015009	-0.000019	14.620	
0.54162	0.46084	0.04941	1.31003	0.212018	0.014465	-0.000020	14.657	
0.55979	0.44267	0.04975	1.31306	0.204624	0.013918	-0.000021	14.702	
0.57801	0.42446	0.04994	1.31623	0.197248	0.013368	-0.000022	14.755	
0.59628	0.40619	0.04998	1.31954	0.189880	0.012816	-0.000023	14.816	
0.61459	0.38788	0.04988	1.32301	0.182510	0.012262	-0.000024	14.885	
0.63294	0.36953	0.04964	1.32665	0.175140	0.011704	-0.000025	14.963	
0.65131	0.35116	0.04927	1.33047	0.167755	0.011146	-0.000026	15.051	
0.66967	0.33281	0.04878	1.33448	0.160358	0.010587	-0.000028	15.147	
0.68796	0.31453	0.04817	1.33869	0.152962	0.010029	-0.000030	15.251	

0.70613	0.29638	0.04745	1.34310	0.145576	0.009475	-0.000031	15.365
0.72411	0.27841	0.04661	1.34771	0.138217	0.008925	-0.000033	15.487
0.74185	0.26070	0.04566	1.35254	0.130913	0.008382	-0.000036	15.619
0.75925	0.24333	0.04461	1.35758	0.123687	0.007848	-0.000038	15.760
0.77623	0.22639	0.04347	1.36283	0.116583	0.007327	-0.000041	15.912
0.79269	0.20998	0.04224	1.36827	0.109621	0.006821	-0.000044	16.072
0.80851	0.19421	0.04094	1.37387	0.102856	0.006333	-0.000048	16.241
0.82359	0.17919	0.03960	1.37960	0.096334	0.005868	-0.000052	16.418
0.83784	0.16501	0.03823	1.38544	0.090088	0.005427	-0.000056	16.600
0.85118	0.15174	0.03685	1.39133	0.084160	0.005014	-0.000061	16.787
0.86358	0.13941	0.03548	1.39723	0.078561	0.004628	-0.000067	16.974
0.87504	0.12803	0.03413	1.40313	0.073305	0.004272	-0.000072	17.161
0.88559	0.11757	0.03281	1.40900	0.068399	0.003942	-0.000079	17.352
0.89528	0.10796	0.03153	1.41482	0.063823	0.003638	-0.000086	17.543
0.90418	0.09915	0.03028	1.42061	0.059561	0.003358	-0.000093	17.738
0.91235	0.09107	0.02907	1.42637	0.055588	0.003099	-0.000101	17.936
0.91987	0.08364	0.02790	1.43210	0.051878	0.002860	-0.000110	18.140
0.92681	0.07679	0.02677	1.43783	0.048399	0.002638	-0.000120	18.347
0.93322	0.07048	0.02569	1.44358	0.045124	0.002432	-0.000130	18.557
0.93915	0.06463	0.02464	1.44936	0.042034	0.002239	-0.000142	18.774
0.94467	0.05921	0.02362	1.45522	0.039123	0.002058	-0.000155	19.009
0.94982	0.05416	0.02263	1.46120	0.036361	0.001888	-0.000170	19.263
0.95463	0.04944	0.02165	1.46732	0.033735	0.001726	-0.000186	19.544
0.95915	0.04503	0.02069	1.47366	0.031247	0.001572	-0.000205	19.876
0.96340	0.04089	0.01975	1.48027	0.028863	0.001425	-0.000227	20.261
0.96741	0.03699	0.01883	1.48722	0.026573	0.001282	-0.000253	20.723
0.97120	0.03331	0.01792	1.49462	0.024367	0.001144	-0.000285	21.298
0.97479	0.02983	0.01703	1.50262	0.022221	0.001009	-0.000325	22.033
0.97820	0.02653	0.01616	1.51158	0.020141	0.000872	-0.000377	23.106
0.98144	0.02341	0.01530	1.52168	0.018079	0.000734	-0.000450	24.631
0.98454	0.02043	0.01444	1.53356	0.016050	0.000591	-0.000517	27.146
0.98749	0.01761	0.01356	1.54849	0.014054	0.000435	-0.000528	32.304
0.99032	0.01494	0.01263	1.57165	0.012067	0.000222	-0.000543	54.282
0.99304	0.01240	0.01165	1.59033	0.010182	0.000086	-0.003952	119.041
0.99566	0.01000	0.01060	1.59110	0.008441	0.000083	-0.004076	101.657
0.99819	0.00775	0.00946	1.59159	0.006720	0.000083	-0.004101	81.277
1.00063	0.00566	0.00819	1.59158	0.005046	0.000085	-0.004015	59.582
1.00300	0.00379	0.00673	1.59116	0.003527	0.000088	-0.003896	40.211
1.00532	0.00218	0.00506	1.59063	0.002198	0.000090	-0.003818	24.287
1.00759	0.00090	0.00319	1.59219	0.001090	0.000090	-0.003975	12.048
1.00982	0.00010	0.00111	1.61470	0.000292	0.000080	0.002221	3.652

1.01203	0.00010	-0.00111	1.68189	0.000114	0.000051	0.091632	2.222
1.01427	0.00090	-0.00319	1.38761	0.000116	0.000053	0.076844	2.181
1.01654	0.00218	-0.00506	1.10350	0.000128	0.000059	0.054940	2.188
1.01885	0.00379	-0.00673	0.87042	0.000140	0.000064	0.039075	2.203
1.02123	0.00566	-0.00819	0.66940	0.000151	0.000069	0.028347	2.186
1.02367	0.00775	-0.00946	0.49127	0.000173	0.000080	0.018580	2.162
1.02620	0.01000	-0.01060	0.35756	0.000204	0.000092	0.010833	2.223
1.02882	0.01240	-0.01165	0.25422	0.000216	0.000099	0.007541	2.183
1.03153	0.01494	-0.01263	0.16494	0.000245	0.000109	0.004087	2.244
1.03437	0.01761	-0.01356	0.08860	0.000250	0.000113	0.002230	2.205
1.03732	0.02043	-0.01444	0.02316	0.000315	0.000141	0.000452	2.230
1.04042	0.02341	-0.01530	-0.02742	0.000315	0.000141	0.000536	2.230
1.04366	0.02653	-0.01616	-0.07800	0.000326	0.000146	0.001463	2.235
1.04707	0.02983	-0.01703	-0.12277	0.000358	0.000159	0.002060	2.256
1.05066	0.03331	-0.01792	-0.16222	0.000383	0.000170	0.002563	2.249
1.05445	0.03699	-0.01883	-0.20047	0.000397	0.000177	0.003063	2.245
1.05846	0.04089	-0.01975	-0.23742	0.000414	0.000184	0.003451	2.253
1.06271	0.04503	-0.02069	-0.26987	0.000447	0.000196	0.003547	2.280
1.06722	0.04945	-0.02165	-0.30259	0.000456	0.000203	0.004014	2.248
1.07204	0.05416	-0.02263	-0.33481	0.000478	0.000211	0.004165	2.267
1.07718	0.05921	-0.02362	-0.36393	0.000507	0.000222	0.004203	2.284
1.08270	0.06463	-0.02464	-0.39184	0.000531	0.000233	0.004337	2.280
1.08864	0.07048	-0.02569	-0.41884	0.000557	0.000244	0.004394	2.286
1.09505	0.07679	-0.02677	-0.44665	0.000574	0.000252	0.004600	2.274
1.10198	0.08364	-0.02790	-0.47299	0.000605	0.000264	0.004536	2.293
1.10951	0.09107	-0.02907	-0.49862	0.000632	0.000276	0.004582	2.293
1.11768	0.09915	-0.03028	-0.52484	0.000655	0.000286	0.004679	2.287
1.12658	0.10796	-0.03153	-0.55078	0.000683	0.000298	0.004679	2.294
1.13627	0.11757	-0.03281	-0.57616	0.000713	0.000310	0.004664	2.299
1.14682	0.12803	-0.03413	-0.60090	0.000746	0.000324	0.004626	2.304
1.15828	0.13941	-0.03548	-0.62567	0.000776	0.000337	0.004636	2.303
1.17068	0.15174	-0.03685	-0.64941	0.000813	0.000352	0.004551	2.312
1.18402	0.16501	-0.03823	-0.67342	0.000843	0.000365	0.004580	2.307
1.19827	0.17919	-0.03960	-0.69711	0.000875	0.000379	0.004557	2.308
1.21335	0.19421	-0.04094	-0.72003	0.000909	0.000393	0.004516	2.312
1.22917	0.20998	-0.04224	-0.74213	0.000943	0.000408	0.004477	2.314
1.24563	0.22639	-0.04347	-0.76401	0.000972	0.000421	0.004489	2.310
1.26261	0.24333	-0.04461	-0.78414	0.001011	0.000436	0.004391	2.320
1.28001	0.26070	-0.04566	-0.80399	0.001039	0.000449	0.004401	2.315
1.29775	0.27841	-0.04661	-0.82275	0.001071	0.000462	0.004357	2.318
1.31573	0.29638	-0.04745	-0.84067	0.001101	0.000475	0.004326	2.319

1.33390	0.31453	-0.04817	-0.85819	0.001127	0.000487	0.004330	2.315
1.35219	0.33281	-0.04878	-0.87487	0.001154	0.000498	0.004305	2.316
1.37054	0.35116	-0.04927	-0.89076	0.001181	0.000510	0.004279	2.317
1.38892	0.36953	-0.04964	-0.90668	0.001200	0.000519	0.004313	2.311
1.40727	0.38788	-0.04988	-0.92218	0.001219	0.000528	0.004328	2.308
1.42558	0.40619	-0.04998	-0.93656	0.001245	0.000538	0.004286	2.313
1.44385	0.42446	-0.04994	-0.95057	0.001266	0.000548	0.004281	2.312
1.46206	0.44267	-0.04975	-0.96357	0.001292	0.000558	0.004233	2.317
1.48024	0.46084	-0.04941	-0.97606	0.001315	0.000567	0.004205	2.319
1.49837	0.47897	-0.04891	-0.98767	0.001341	0.000577	0.004151	2.324
1.51649	0.49708	-0.04824	-0.99824	0.001372	0.000588	0.004070	2.332
1.53467	0.51524	-0.04739	-1.00697	0.001415	0.000602	0.003908	2.351
1.55296	0.53350	-0.04636	-1.01425	0.001463	0.000617	0.003732	2.372
1.57140	0.55190	-0.04517	-1.02070	0.001508	0.000632	0.003589	2.387
1.59001	0.57046	-0.04384	-1.02682	0.001548	0.000647	0.003490	2.395
1.60878	0.58918	-0.04237	-1.03238	0.001589	0.000662	0.003393	2.402
1.62771	0.60804	-0.04076	-1.03792	0.001624	0.000676	0.003333	2.404
1.64681	0.62706	-0.03904	-1.04294	0.001662	0.000690	0.003256	2.409
1.66607	0.64623	-0.03719	-1.04778	0.001698	0.000704	0.003193	2.411
1.68549	0.66555	-0.03524	-1.05253	0.001732	0.000718	0.003144	2.412
1.70506	0.68501	-0.03319	-1.05714	0.001764	0.000731	0.003098	2.412
1.72477	0.70461	-0.03105	-1.06165	0.001796	0.000745	0.003057	2.412
1.74464	0.72435	-0.02882	-1.06598	0.001828	0.000758	0.003013	2.413
1.76463	0.74421	-0.02652	-1.07034	0.001857	0.000770	0.002984	2.411
1.78472	0.76416	-0.02417	-1.07488	0.001881	0.000782	0.002972	2.406
1.80484	0.78414	-0.02178	-1.07987	0.001897	0.000792	0.002992	2.396
1.82492	0.80408	-0.01938	-1.08484	0.001914	0.000801	0.003000	2.389
1.84486	0.82387	-0.01698	-1.08996	0.001928	0.000810	0.003016	2.381
1.86451	0.84338	-0.01464	-1.09576	0.001930	0.000816	0.003074	2.365
1.88377	0.86251	-0.01238	-1.10283	0.001914	0.000818	0.003201	2.339
1.90256	0.88117	-0.01023	-1.11105	0.001887	0.000817	0.003368	2.309
1.92073	0.89922	-0.00819	-1.11985	0.001859	0.000815	0.003533	2.282
1.93811	0.91651	-0.00628	-1.12775	0.001850	0.000815	0.003611	2.271
1.95464	0.93294	-0.00459	-1.13774	0.001811	0.000808	0.003828	2.240
1.97035	0.94859	-0.00317	-1.15329	0.001710	0.000787	0.004368	2.172
1.98534	0.96354	-0.00207	-1.18057	0.001521	0.000741	0.005546	2.053
1.99967	0.97785	-0.00118	-1.22249	0.001299	0.000675	0.007417	1.926
2.01326	0.99142	-0.00044	-1.29386	0.001029	0.000577	0.010956	1.784
2.02186	1.00000	0.00000	-1.25086	0.001439	0.000683	0.005944	2.107
2.02186	1.00010	0.00000	1.25086	0.418576	0.031433	0.000000	13.316
2.03045	1.00869	0.00010	1.24928	0.416120	0.032039	0.000000	12.988

2.04032	1.01856	0.00043	1.24754	0.415620	0.032709	0.000000	12.707
2.05165	1.02988	0.00095	1.24554	0.415242	0.033482	0.000000	12.402
2.06466	1.04287	0.00170	1.24324	0.414878	0.034376	0.000000	12.069
2.07961	1.05778	0.00272	1.24058	0.414419	0.035413	0.000000	11.702
2.09677	1.07488	0.00407	1.23751	0.413776	0.036617	0.000000	11.300
2.11647	1.09451	0.00582	1.23396	0.412854	0.038019	0.000000	10.859
2.13910	1.11703	0.00806	1.22986	0.411537	0.039652	0.000000	10.379
2.16509	1.14286	0.01090	1.22510	0.409684	0.041560	0.000000	9.858
2.19493	1.17249	0.01445	1.21957	0.407112	0.043793	0.000000	9.296
2.22921	1.20647	0.01889	1.21314	0.403591	0.046414	0.000000	8.695
2.26856	1.24544	0.02440	1.20564	0.398825	0.049501	0.000000	8.057
2.31375	1.29012	0.03119	1.19684	0.392428	0.053151	0.000000	7.383
2.36565	1.34135	0.03953	1.18648	0.383901	0.057492	0.000000	6.677
2.42525	1.40007	0.04972	1.17417	0.372587	0.062700	0.000000	5.942
2.49369	1.46737	0.06215	1.15930	0.357616	0.069040	0.000000	5.180
2.57228	1.54450	0.07723	1.14079	0.337836	0.077004	0.000000	4.387
2.66253	1.63289	0.09546	1.11532	0.311914	0.088106	0.000000	3.540
2.76618	1.73418	0.11744	1.08379	0.276528	0.102056	0.000000	2.710
2.88519	1.85023	0.14384	1.07544	0.224272	0.105603	0.000000	2.124
3.02187	1.98320	0.17546	1.22525	0.088663	0.064788	0.000000	1.369

BIBLIOGRAPHY

- [1] J. Mattingly, *Elements of Propulsion, Gas Turbines and Rockets*. Virginia: American Institute of Aeronautics and Astronautics, 1 ed., 2006.
- [2] Y. Nakayama and R. F. Boucher, *Introduction to Fluid Mechanics*. London: Elsevier, 2 ed., 2000.
- [3] R. Nelson, T. Corke, and H. Othman, “A smart wind turbine blade using distributed plasma actuators for improved performance,” AIAA Paper 2008–1312, 46th AIAA Aerospace Sciences Meeting and Exhibit, Reno, NV, Jan. 2008.
- [4] M. Drela, “Xfoil.” website. <http://web.mit.edu/drela/Public/web/xfoil/>.
- [5] “Corporate report: Parent of united airlines projects fuel bill \$3.5 billion higher than last year,” *www.heraldtribune.com*, June 2008.
- [6] C. L. Enloe, T. E. McLaughlin, R. D. VanDyken, K. D. Kachner, E. J. Jumper, and T. C. Corke, “Mechanisms and responses of a single dielectric barrier discharge plasma actuator: Plasma morphology,” *AIAA Journal*, vol. 42, no. 3, pp. 589–594, 2004.
- [7] C. L. Enloe, T. E. McLaughlin, R. D. VanDyken, K. D. Kachner, E. J. Jumper, T. C. Corke, M. Post, and O. Haddad, “Mechanisms and responses of a single dielectric barrier discharge plasma actuator: Geometric effects,” *AIAA Journal*, vol. 42, no. 3, pp. 595–604, 2004.

- [8] M. L. Post and T. C. Corke, “Separation control using plasma actuators – dynamic stall control on an oscillating airfoil,” AIAA Paper 2004–2517, 2nd AIAA Flow Control Conference, Portland, OR, June 2004.
- [9] J. Huang, T. C. Corke, and F. O. Thomas, “Plasma actuators for separation control of low-pressure turbine blades,” *AIAA Journal*, vol. 44, no. 1, pp. 51–57, 2006.
- [10] J. H. Mabe, F. T. Calkins, B. Wesley, R. Woszidlo, L. Taubert, and I. Wygnanski, “On the use of single dielectric barrier discharge plasma actuators for improving the performance of airfoils,” AIAA Paper 2007–3972, 45th Aerospace Sciences Meeting and Exhibit, Reno, NV, Jan. 2007.
- [11] J. D. Wall, I. C. Boxx, and R. Rivir, “Effects of pulsed-d.c. discharge plasma actuators in a separated low pressure turbine boundary layer,” AIAA Paper 2004–0842, 45th AIAA Aerospace Sciences Meeting and Exhibit, Reno, NV, Jan. 2007.
- [12] D. M. Orlov, T. Apker, C. He, H. Othman, and T. C. Corke, “Modeling and experiment of leading edge separation control using sdbd plasma actuators,” AIAA Paper 2007–0877, 45th AIAA Aerospace Sciences Meeting and Exhibit, Reno, NV, Jan. 2007.
- [13] J. Prato and B. Lakshminarayana, “Investigation of compressor rotor wake structure at peak pressure rise coefficient and effects of loading,” *J. Turbomachinery*, vol. 115, pp. 487–500, 1993.
- [14] E. Braunscheidel, D. Culley, and K. Zaman, “Application of synthetic jets to reduce stator flow separation in a low speed axial compressor,” AIAA Paper 2008–0602, 46th AIAA Aerospace Sciences Meeting and Exhibit, Reno, NV, Jan. 2008.

- [15] M. Kefalakis and K. Papailiou, “Active flow control for increasing the surge margin of an axial flow compressor,” tech. rep., Laboratory of Thermal Turbomachines, National Technical University of Athens, Iroon Polytechniou 9, Athens 15773, Greece.
- [16] S. Gbadebo, N. Cumpsty, and T. Hynes, “Control of three-dimensional separations in axial compressors by tailored boundary layer suction,” *J. Turbomachinery*, Jan. 2008.
- [17] N. Nguyen, M. Bright, and D. Culley, “Adaptive feedback optimal control of flow separation on stators by air injection,” *AIAA Journal*, vol. 45, pp. 1393–1405, 2007.
- [18] J. Gregory, J. Ruotolo, A. Byerley, and T. McLaughlin, “Switching behavior of a plasma-fluidic actuator,” tech. rep., United States Air Force Academy, USAF Academy, CO, 80840.
- [19] C. Enloe, M. McHarg, and T. McLaughlin, “Time-correlated force production measurements of the dielectric barrier discharge plasma aerodynamic actuator,” *J. Appl. Phys.*, vol. 103, pp. 1–7, 2008.
- [20] M. P. Patel, T. T. Ng, and S. Vasudevan, “Plasma actuators for hingeless aerodynamic control of an unmanned air vehicle,” *Journal of Aircraft*, vol. 44, no. 4, pp. 1264–1274, 2007.
- [21] W. Shyy, B. Jayaraman, and A. Andersson, “Modeling of dielectric barrier discharge plasma actuator,” *J. Appl. Phys.*, vol. 92, pp. 6434–6443, Dec. 2002.
- [22] B. Jayaraman, Y. Cho, and W. Shyy, “Flow control and thermal management using dielectric glow discharge concepts,” AIAA Paper 2007–4531, 38th AIAA Plasmadynamics and Lasers Conference, Miami, FL, June 2007.

- [23] J. W. Gregory, C. L. Enloe, G. I. Font, and T. E. McLaughlin, “Force production mechanisms of a dielectric-barrier discharge plasma actuator,” AIAA Paper 2007–0185, 45th Aerospace Sciences Meeting and Exhibit, Reno, NV, Jan. 2007.
- [24] D. Greenblatt, C. Schle, D. Romann, and C. Paschereit, “Dielectric barrier discharge flow control at very low flight reynolds numbers,” *AIAA Journal*, vol. 46, no. 6, pp. 1528–1541, 2008.
- [25] D. VanNess, T. Corke, and S. Morris, “Turbine tip clearance flow control using plasma actuators,” AIAA Paper 2006–0021, 44th Aerospace Sciences Meeting and Exhibit, Reno, NV, Jan. 2006.
- [26] H. D. Vo, “Control of rotating stall in axial compressors using plasma actuators,” AIAA Paper 2006–0021, 37th Aerospace Sciences Meeting and Exhibit, Miami, FL, 2007.
- [27] Y. WU, Y. LI, J. ZHU, C. SU, H. LIANG, and G. LI, “Experimental investigation of a subsonic compressor with plasma actuation treated casing,” AIAA Paper 2007–3849, 37th Aerospace Sciences Meeting and Exhibit, Miami, FL, 2007.
- [28] D. K. VanNess, T. C. Corke, and S. C. Morris, “Stereo piv of a turbine tip clearance flow with plasma actuation,” AIAA Paper 2007–0647, 45th Aerospace Sciences Meeting and Exhibit, Reno, NV, Jan. 2007.
- [29] J. Hansen, “Design, installation and initial validation of the oklahoma state compressor aerodynamics research facility,” Master’s thesis, Oklahoma State University, Stillwater, OK, July 2004.
- [30] R. J. Goldstein, *Fluid Mechanics Measurements*. Philadelphia, PA: Taylor and Francis, 2 ed., 1996.

- [31] F. E. Jorgenson, “How to measure turbulence with hot-wire anemometers - a practical guide.” Dantec Dynamics, Skovlunde, Denmark, February 2002.
- [32] M. Sholl and Ö. Savaş, “A fast lagrangian PIV method for study of general high-gradient flows,” AIAA Paper 1997-0493, 35th AIAA Aerospace Sciences Meeting, Reno, NV, Jan. 1997.
- [33] L. Tsuei and Ö. Savaş, “Treatment of interfaces in particle image velocimetry,” *Experiments in Fluids*, vol. 29, pp. 203–214, 2000.
- [34] K. Ramakumar, “Active flow control of low pressure turbine blade separation using plasma actuators,” Master’s thesis, University of Kentucky, Lexington, Kentucky, 2006.
- [35] M. Selig, “Naca coordinate source code.” website. <http://www.ae.uiuc.edu/m-selig/ads.html>.
- [36] M. Visbal, D. Gaitonde, and S. Roy, “Exploration of plasma-based flow control strategies using high-fidelity 3d simulations,” afosr/usafa plasma simulation workshop presentation, Air Force Academy , CO, Nov. 2006.

VITA

Craig Williamson

Candidate for the Degree of

Masters of Science

Thesis: COMPRESSOR BLADE FLOW CONTROL IN AN AXIAL COMPRESSOR WITH PLASMA ACTUATORS

Major Field: Mechanical Engineering

Biographical:

Personal Data: Born in Redlands, California, U.S.A. in August, 1977.

Education:

Received the B.S. degree from Oklahoma Christian University, Oklahoma City, Oklahoma, U.S.A., 2000, in Mechanical Engineering

Completed the requirements for the degree of Master of Science with a major in Mechanical Engineering at Oklahoma State University in December, 2008.

Experience:

Craig Williamson began his career with the United States Air force at Tinker Air force base, Oklahoma. His career in gas turbine propulsion includes positions held on the F100, TF34 and J85 Jet engines. He instructed multiple training courses on Comprehensive Engine Trending and Diagnosis both in Oklahoma and Germany. He received his M.S. in Mechanical Engineering at Oklahoma State University in 2008, sponsored by the USAF as a student in the Long Term Full Time Training program. He intends to continue his career with the USAF as an Aerospace Engineer.

Name: CRAIG WILLIAMSON

Date of Degree: December, 2008

Institution: Oklahoma State University

Location: Stillwater, Oklahoma

Title of Study: COMPRESSOR BLADE FLOW CONTROL IN AN AXIAL COMPRESSOR WITH PLASMA ACTUATORS

Pages in Study: 140

Candidate for the Degree of Master of Science

Major Field: Mechanical Engineering

Flow control in an axial compressor using plasma actuators was investigated. A plasma actuator was mounted on blades in a rotating compressor cascade and its effects on the flow were observed via wake measurements. Prior to the blade study, two configurations of a plasma actuator were examined in the quiescent state using particle image velocimetry (PIV) with either Teflon or Kapton as the dielectric material. The velocity profiles for the Kapton and Teflon dielectrics with steady plasma actuation showed that the Kapton configuration only produced a maximum velocity of about 5 cm/s while the Teflon configuration produced a maximum velocity of about 40 cm/s. Pulsing the actuators for the same arrangement with a forcing frequency of 50 Hz displayed maximum velocities of about 3 cm/s and 9 cm/s on the Kapton and Teflon configurations, respectively. Momentum calculations performed on the two actuator configurations and an average compressor rotor blade wake show that the Teflon actuator momentum input was approximately 1% of the blade wake momentum deficit. The Teflon configured actuator was installed on one blade in a single stage axial compressor and blade wakes were measured in the laboratory reference frame using a hot-wire anemometer. Blade wake momentum calculations were made on the compressor rotor in response to various plasma actuator and compressor operating conditions. Both leading edge and 1/4 chord plasma actuator configurations were examined in the counter and co-flow directions. The blade wake of the rotor was measured using a hot-wire at blade Reynolds numbers of 170,000 and 260,000. The compressor rotor momentum calculations showed that leading edge actuation can have an unpredictable effect and may cause an increase in drag. The best case observed was at steady actuation for a Reynolds number of 170,000 and at a forcing frequency of 50 Hz for a Reynolds number of 260,000. The counter flow actuator orientation at 1/4 chord showed less control than over the co-flow case. The maximum drag decrease was seen at a Reynolds number of 170,000 and a forcing frequency of 50 Hz.

ADVISOR'S APPROVAL:

Dr. Jamey Jacob